MAGNETIC SKYRMION PHASE IN MNSI THIN FILMS

by

Murray Neff Wilson

Submitted in partial fulfillment of the
requirements for the degree of
Master of Science

at

Dalhousie University
Halifax, Nova Scotia
April 2013

DALHOUSIE UNIVERSITY

DEPARTMENT OF PHYSICS AND ATMOSPHERIC SCIENCE

The undersigned hereby certify that they have read and recommend to the Faculty of Graduate Studies for acceptance a thesis entitled "MAGNETIC SKYRMION PHASE IN MNSI THIN FILMS" by Murray Neff Wilson in partial fulfillment of the requirements for the degree of Master of Science.

Dated: April 1, 2013

Supervisor:

Professor Theodore Monchesky

Readers:

Professor Richard Dunlap

Professor Kevin Hewitt

DALHOUSIE UNIVERSITY

DATE: April 1, 2013

AUTHOR: Murray Neff Wilson

TITLE: MAGNETIC SKYRMION PHASE IN MNSI THIN FILMS

DEPARTMENT OR SCHOOL: Department of Physics and Atmospheric Science

DEGREE: M.Sc. CONVOCATION: May YEAR: 2013

Signature of Author

Table of Contents

List of Tables

List of Figures

Abstract

Detailed magnetometry and polarized neutron reflectometry studies were conducted on MnSi thin films grown epitaxially on Si(111) substrates. It is demonstrated that with an in-plane applied field $\vec{H} \parallel [1\bar{1}0]$, a broadly stable skyrmion phase exists at elevated temperatures and fields.

Magnetometry and transport measurements with an out-of-plane applied field $\vec{H} \parallel [111]$ prove that no skyrmion phase exists in this geometry. However, Hall effect measurements in this geometry show unexpected evidence of a topological Hall effect. This can be explained with a multi-dimensionally modulated cone phase, which proves that contrary to recent literature, a topological Hall effect is not sufficient proof of skyrmions.

The results of this thesis represent a significant step towards a technologically relevant material in which skyrmions are broadly stable. A material of this type could be used in novel magnetic storage devices and significantly impact our future computing capabilities.

List of Abbreviations and Symbols Used

$\boldsymbol{\alpha_c}$: Neutron critical angle

$\boldsymbol{\alpha}$: Neutron incidence angle

$\boldsymbol{\beta}$: Geometric factor for fitting SQUID voltage

$\boldsymbol{\chi_{Si}}$: Substrate susceptibility background correction factor

$\boldsymbol{\eta}$: Sensitivity factor for fitting SQUID voltage

$\boldsymbol{\gamma}$: Geometric factor for fitting SQUID voltage

$\boldsymbol{\lambda}$: Helical/conical wavelength

$\boldsymbol{\mu_0}$: Permeability of free space

$\boldsymbol{\mu_B}$: Bohr magneton

$\boldsymbol{\mu_n}$: Nuclear magneton

$\boldsymbol{\mu}$: Total magnetic moment measured by SQUID

$\boldsymbol{\phi_0}$: Helicoid translation parameter

$\boldsymbol{\Phi}$: Skyrmion density

$\boldsymbol{\phi}$: Azimuthal angle of effective magnetization relative to neutron spin

$\boldsymbol{\psi}$: Neutron wave function

$\boldsymbol{\rho_{xx0}}$: Zero field linear resistivity

$\boldsymbol{\rho_{xx}}$: Linear resistivity

$\boldsymbol{\rho_{yx}^{top}}$: Topological Hall resistivity

$\boldsymbol{\rho_{yx}}$: Hall resistivity

$\boldsymbol{\rho}$: Atomic density

$\boldsymbol{\sigma_{yx}^{top}}$: Topological Hall conductivity

$\boldsymbol{\sigma}$: Layer roughness

$\boldsymbol{\tau}$: Transport lifespan

$\boldsymbol{\theta}$: Polar angle of effective magnetization relative to neutron spin

$\boldsymbol{\varphi}$: Cone angle

$\boldsymbol{\hat{M}}$: Magnetization unit vector

$\boldsymbol{\hat{n}}$: Unit vector describing direction of uniaxial anisotropy

$\boldsymbol{\mathfrak{C}}$: Cone

$\boldsymbol{\mathcal{F}}$: Ferromagnetic

$\boldsymbol{\mathcal{H}}$: Helicoid

$\boldsymbol{\mathcal{SK}}$: Skyrmion

$|+>, |->$: Basis spin states

$\boldsymbol{\vec{\sigma}_P}$: Pauli spin matrices

$\boldsymbol{\vec{B}_{eff}}$: Effective field from sample magnetization

$\boldsymbol{\vec{H}}$: Magnetic field vector

$\boldsymbol{\vec{L}}$: Cubic invariant describing anisotropic exchange

$\vec{M}$: Magnetization vector

$\vec{Q}$: Propogation vector

$\vec{S}$: Spin vector

$A, B_{+,-}$: Neutron wavefunction coefficients

$ASYM$: PNR reflected spin asymmetry

A : Spin wave stiffness

a : Cubic lattice constant

b_D : Dzyaloshinskii-Moriya free energy prefactor

b_m : Magnetic neutron scattering length

b : Neutron scattering length

C : Topological Hall resistivity fitting parameter

c : Exchange free energy prefactor

D : Dzyaloshinskii-Moriya constant

d : Film thickness

E : Neutron energy

F : Anisotropic exchange constant

f : Sample footprint

g_n : Lande factor

G : Helicoid offset

$\boldsymbol{H_D}$: Effective bulk zero-anisotropy saturation field

$\boldsymbol{H_d}$: Demagnetizing stray field

$\boldsymbol{H_h}$: Helicoid upper stability field

$\boldsymbol{H_\alpha}$, $\boldsymbol{H_{\alpha 1}}$, $\boldsymbol{H_{\alpha 2}}$, $\boldsymbol{H_\beta}$: First-order transition fields in MnSi thin films with an applied field in plane

$\boldsymbol{H_{C2}^{\parallel}}$: Transition field between conical and ferromagnetic phases with an applied field in-plane

$\boldsymbol{H_{C2}^{\perp}}$: Transition field between conical and ferromagnetic phases with an applied field out-of-plane

$\boldsymbol{H_{C2}}$: Transition field between conical and ferromagnetic phases

$\boldsymbol{H_{S1}}$: Skyrmion lower equilibrium stability field

$\boldsymbol{H_{S2}}$: Skyrmion upper equilibrium stability field

$\boldsymbol{H_{S3}}$: Skyrmion upper stability field

$\boldsymbol{H_{sat}^{\parallel}}$: In-plane saturation field

$\boldsymbol{H_{sat}^{\perp}}$: Out-of-plane saturation field

$\boldsymbol{H}$: Magnetic field

$\boldsymbol{I}$: Current

$\boldsymbol{K_0}$: Effective stiffness of the conical phase

$\boldsymbol{K_m}$: Demagnetizing field contribution to saturation field

$\boldsymbol{K_u}$: Uniaxial anisotropy constant

$\boldsymbol{k}$: Wavevector

$\boldsymbol{l_o}$: Linear offset for fitting SQUID voltage

$\boldsymbol{L}$: Sample length

$\boldsymbol{l}$: Beam length

$\boldsymbol{M_1}$: First harmonic magnetization

$\boldsymbol{M_2}$: Second harmonic magnetization

$\boldsymbol{M_S}$: Saturation magnetization

$\boldsymbol{m_n}$: Neutron mass

$\boldsymbol{n_C}$: Charge carrier density

$\boldsymbol{P}$: Sample position for SQUID voltage measurements

$\boldsymbol{q_c}$: Neutron critical scattering vector

$\boldsymbol{Q}$: Helical propogation vector

$\boldsymbol{q}$: Neutron scattering vector

$\boldsymbol{R_0}$: Ordinary Hall coefficient

$\boldsymbol{R_S}$: Anomolous Hall coefficient

$\boldsymbol{R_{++}}$: Spin-up neutron reflectivity

$\boldsymbol{r_{++}}$: Spin-up to spin-up neutron reflectivity coefficient

$\boldsymbol{r_{+-}}$: Spin-up to spin-down neutron reflectivity coefficient

$\boldsymbol{r_{-+}}$: Spin-down to spin-up neutron reflectivity coefficient

$\boldsymbol{R_{--}}$: Spin-down neutron reflectivity

$\boldsymbol{r_{--}}$: Spin-down to spin-down neutron reflectivity coefficient

$\boldsymbol{r}$: Geometric factor for fitting SQUID voltage

$\boldsymbol{S(d)}$: Skyrmion depth profile

$\boldsymbol{S_f}$: Skyrmion fraction

$\boldsymbol{S_H}$: Anomolous Hall resistivity fitting parameter

$\boldsymbol{S_w}$: Slit width

$\boldsymbol{SC}$: Spin chirality

$\boldsymbol{SLD}$: Scattering length density

$\boldsymbol{SPFR}$: Spin flip ratio

$\boldsymbol{S}$: Spin per unit cell

$\boldsymbol{T_C}$: Curie temperature

$\boldsymbol{t_{++}}$: Spin-up to spin-up neutron transmission coefficient

$\boldsymbol{t_{+-}}$: Spin-up to spin-down neutron transmission coefficient

$\boldsymbol{u_{Mn,Si}}$: Basis vectors for Mn and Si atoms

$\boldsymbol{V_H}$: Hall effect voltage

$\boldsymbol{V_L}$: Longitudinal voltage

$\boldsymbol{V_{mag}}$: Magnetic neutron interaction potential

$\boldsymbol{V}$: Total neutron interaction potential

$\boldsymbol{v}$: Film volume

$\boldsymbol{w}$: Free energy density

$\boldsymbol{y}$: Depth in film

$\boldsymbol{z}$: Center position for SQUID voltage measurements

$\boldsymbol{n}$: Index of refraction

GMR : Giant magnetoresistance

PG : Pyrolytic graphite

PNR : Polarized neutron reflectometry

SANS : Small angle neutron scattering

SQUID : Superconducting Quantum Interference Device

Acknowledgements

I would like to thank my supervisor, Professor Theodore Monchesky, for his invaluable assistance during this project. I would also like to thank Dr. Eric Karhu for his assistance, and for growing the films studied in this project. I would like to thank my colleague Samer Kahwaji for his assistance with SQUID measurements. In addition, I would like to thank Dr. Helmut Fritzsche at the NRC Canadian Neutron Beam Centre for his assistance conducting PNR measurements, and I would like to thank Prof. A.N. Bogdanov, Dr. U.K. Rößler, Dr. F.N. Rybakov, and A.B. Butenko for their theoretical calculations. I would also like to thank Michel Johnson for his assistance with the electrical transport measurements. Finally, I would like to acknowledge the Dalhousie Institute for Research in Materials and the Natural Sciences and Engineering Research Council for financial support during this work.

Chapter 1

Introduction

Spintronics, the study of the control of electron spin in materials as well as charge, is a nascent field that has already had significant impacts on society. This field first emerged in the 1970s and 1980s with the discovery of spin-dependent tunneling by Julliere [1] and giant magnetoresistance (GMR) by Binasch et al. [2] and Baibich et al. [3]. Giant magnetoresistance is an effect that occurs in materials consisting of stacked ferromagnetic and nonmagnetic conducting thin film layers. In these materials, the resistance changes dramatically when adjacent ferromagnetic layers are aligned either parallel or antiparallel to one another. This change in resistance comes about through spin-dependent scattering of the electrons as they pass through the material. Both groups performed their initial studies on stacked Fe/Cr/Fe layers and found a maximum resistance change of approximately 80% when the layers were placed in a saturating field at $T = 4$ K [2, 3]. This large change in resistance enabled devices made of these layers to find widespread application in the read/write heads of magnetic hard drives, facilitating the enormous increases in data storage density seen in recent years.

The second founding discovery of spintronics, spin-dependent tunneling, occurs in ferromagnetic/insulating/ferromagnetic trilayer structures. If the insulating layer is sufficiently thin, quantum mechanics tells us that there will be a small tunneling current through the insulator when a voltage is applied to the structure. Julliere showed that this tunneling current depends on the relative orientation of the ferromagnetic layers when he studiedin Fe/Ge/Co junctions [1]. While the change in current discovered by Julliere was only 14%, later work has found changes of 180%

in Fe/MgO/Fe junctions [4], and 604% in CoFeB/MgO/CoFeB junctions [5]. These large current changes have allowed devices using spin-dependent tunneling to replace giant magnetoresistance sensors in hard drives today.

Another important spin transport process is known as spin transfer torque, where a spin polarized current transfers angular momentum from one magnetic layer to another [6]. This effect was first proposed by Berger [7] in 1978, and first observed by Freitas et al. [8] in 1985. This first observation demonstrated that a spin polarized current passing through a ferromagnetic material can drag domain walls along with it at an appreciable speed, and later work found that this speed can be up to 110 m/s [9]. In 1996, Slonczewski [10] and Berger [11] independently predicted that a spin polarized current that passes through a multilayer structure could reorient the magnetization in one of the layers. This prediction was important for the development GMR applications, and spurred a large amount of research into spin transfer torque.

Recently, a new type of magnetic memory called "racetrack memory" has been proposed by Parkin et al. [12] that would make use of spin transfer torque induced domain wall motion. Bits of data would be stored in domains along a magnetic wire, and then moved past a conventional magnetic read/write head by passing a spin polarized current through the wire. This would allow high density data storage without the moving parts that exist in modern hard drives, hopefully improving reliability and reducing power requirements. However, moving magnetic domains in ferromagnets requires very large current densities, typically on the order of $10^{11}\mathrm{A/m}^2$; this uses a large amount of power. This poses a significant technological challenge for racetrack memory devices. Hence, it is an important concern to find novel types of materials where spin transfer torque can occur at much lower current densities.

A few years ago Jonietz et al. demonstrated a spin transfer torque induced rotation in bulk crystals of MnSi [13], and more recently Yu et al. demonstrated spin transfer torque induced linear motion in FeGe [14]. These spin transfer torque effects occurred in a novel magnetic phase known as the skyrmion phase, and were shown to

require current densities as small as 10^6 A/m^2. Current densities on this scale would enable a much more practical racetrack memory device and could lead to commercial development in the near future. For development to proceed, detailed understanding of the materials, cubic helimagnets, that host this skyrmion phase is necessary.

1.1 Bulk MnSi and Other Cubic Helimagnets

MnSi is a member of a class of materials known as cubic helimagnets. These materials form a B20 cubic crystal structure (space group $P2_13$), which is a distorted rock salt structure with basis vectors $(u, u, u), (\frac{1}{2}+u, \frac{1}{2}-u, -u), (-u, \frac{1}{2}+u, \frac{1}{2}-u)$ and $(\frac{1}{2}-u, -u, \frac{1}{2}+u)$. The positions for MnSi are given by $u_{Mn} = 0.137$ and $u_{Si} = 0.845$ [15]. This crystal structure lacks inversion symmetry and hence can take on either a left or right handed crystal chirality. The structure is shown below in Fig. 1.1 for a left-handed MnSi crystal.

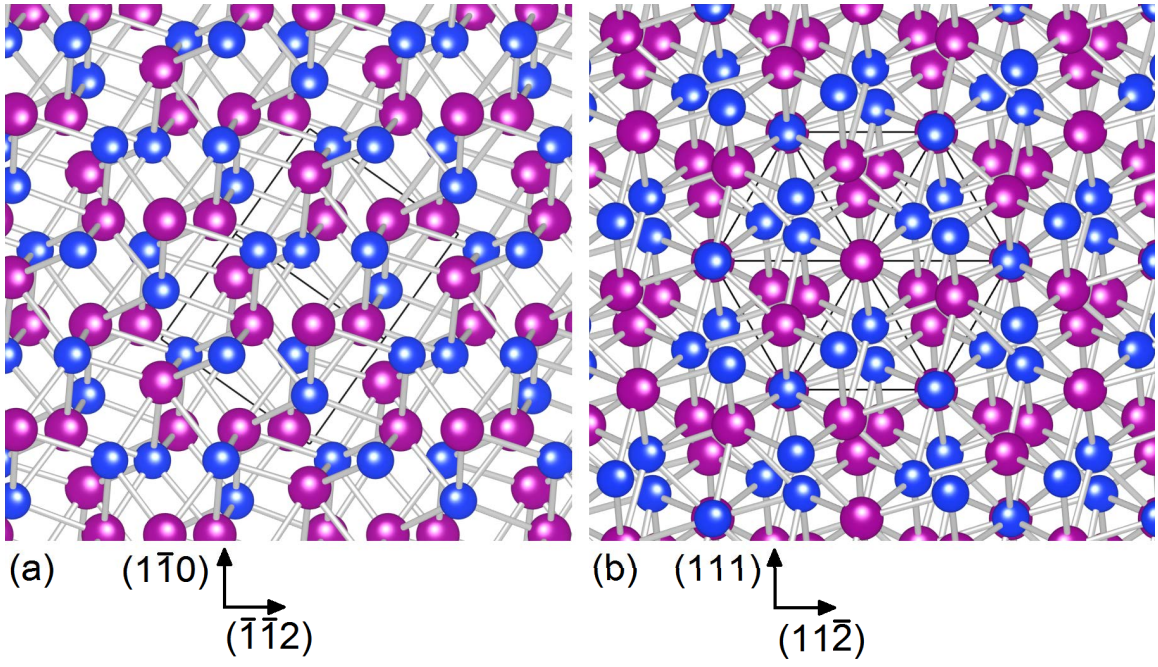

Figure 1.1: MnSi B20 cubic crystal structure. Purple atoms are Mn while blue atoms are Si. (a) Crystal axis (111) pointing out of the page. (b) Crystal axis (1$\bar{1}$0) axis out of plane. This structure is shown for a left handed crystal.

Crystals that lack inversion symmetry have four main interactions that contribute to the free energy density. These are the two standard magnetic interactions: Zeeman, and exchange, as well as a weak anisotropic exchange interaction, and an additional interaction which comes about from the lack of inversion symmetry. This additional interaction is the Dzyaloshinskii-Moriya interaction, which is caused by spin-orbit coupling and takes the form $\vec{S_i} \times \vec{S_j}$, where $\vec{S_{i,j}}$ are neighboring spins in the material [16, 17]. The free energy density, w, resulting from these interactions is shown in Eq. 1.1 [18, 19, 20].

$$w(M) = \frac{c}{2} M_s^2 (\nabla \hat{M})^2 + b_D M_s^2 \hat{M} \cdot (\nabla \times \hat{M}) + \frac{S^2 F Q^2 (\vec{L} \cdot \hat{M})^2}{4a^3} - \mu_0 \vec{H} \cdot \vec{M} \qquad (1.1)$$

In this equation M_S is the saturation magnetization, $\vec{M}$ is the magnetization vector, $\hat{M} = \frac{\vec{M}}{M_S}$ is a unit vector in the direction of the magnetization, $\vec{H}$ is the applied magnetic field, $S = 0.8\hbar$ is the spin per unit cell, $a = 0.4558$ nm is the lattice constant, F is the anisotropic exchange constant, and $\vec{L}$ is the cubic invariant which describes the anisotropy. The constants c and b_D are related to the spin wave stiffness A and the Dzyaloshinskii-Moriya constant D by $c = AS/(M_S^2 a^3)$ and $b_D = DS/(M_S^2 a^3)$.

As shown by Eq. 1.1, the Dzyaloshinskii-Moriya term, which is the second term in this equation, is an interaction that favors perpendicular alignment of adjacent spins, while the exchange interaction, the first term in Eq. 1.1, favors parallel alignment. The competition between these two interactions forms complicated magnetic textures in MnSi that are modulated in one or more dimensions. The common one dimensionally modulated structures are the helical and the conical phases, while the two dimensionally modulated structure is the aforementioned skyrmion phase. The

helical phase shown in Fig. 1.2 (a), consists of layers of ferromagnetically aligned spins that are perpendicular to the propagation vector, $\vec{Q}$, while adjacent layers have spins oriented at slightly different angles to form a twist with a particular chirality. The angle increases linearly in the $\hat{Q}$ direction, and spans a full cycle of 2π in a distance equal to the helical wavelength, $\lambda = \frac{2\pi}{|Q|}$. The cone phase is similar to the helix, except that the spins are canted towards the Q vector at an angle φ, called the cone angle, rather then being perpendicular to it, as shown in Fig. 1.2 (b). An expression for the magnetization of this phase with $\vec{Q}$ vector parallel to $\hat{z}$ the is shown in Eq. 1.2; the magnetization for the helical phase can be obtained by setting $\varphi = 0$ in this equation.

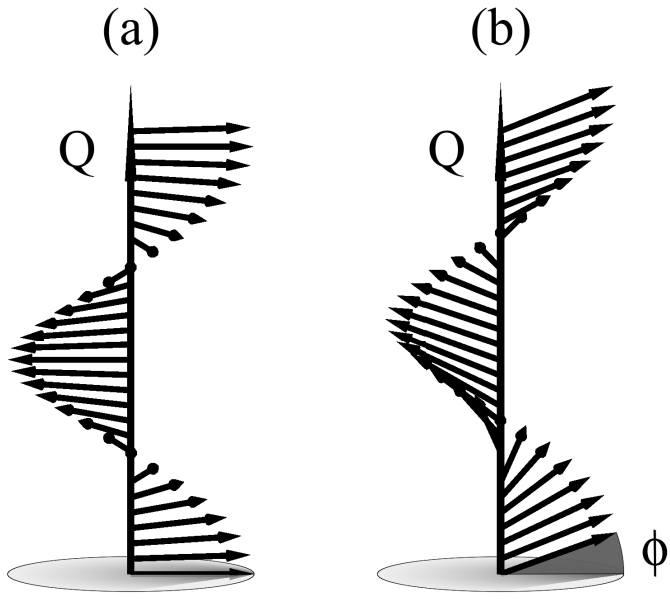

Figure 1.2: Magnetization structure where the arrows represent the direction of the magnetization at each point. (a) Helix, (b) Cone with cone angle $\varphi = \frac{\pi}{9}$

$$\vec{M} = M_S(sin(Qz)cos(\varphi), cos(Qz)cos(\varphi), sin(\varphi)) \tag{1.2}$$

Early investigations by Ishikawa et al. and Motoya et al. showed that MnSi orders magnetically in a helical state below a Curie temperature $T_C = 30$ K at zero field [21, 22, 23]. This helical phase has a multi-domain structure with the Q vectors

oriented along the ⟨111⟩ crystallographic directions. This indicates a weak cubic anisotropy derived from the anisotropic exchange interaction [21]. The Q vector of the helical phase aligns with the magnetic field for an applied field above 0.15 T, above which field the magnetic state evolves continuously through a cone state and into the ferromagnetic state at $H_{C2} = 0.62$ T [21].

Kusaka et al. used ultrasonic attenuation to map out the phase diagram of MnSi, shown in Fig. 1.3 [24]. This study identified an additional phase near the Curie temperature that was previously unknown, which was called the A-phase. The mag-

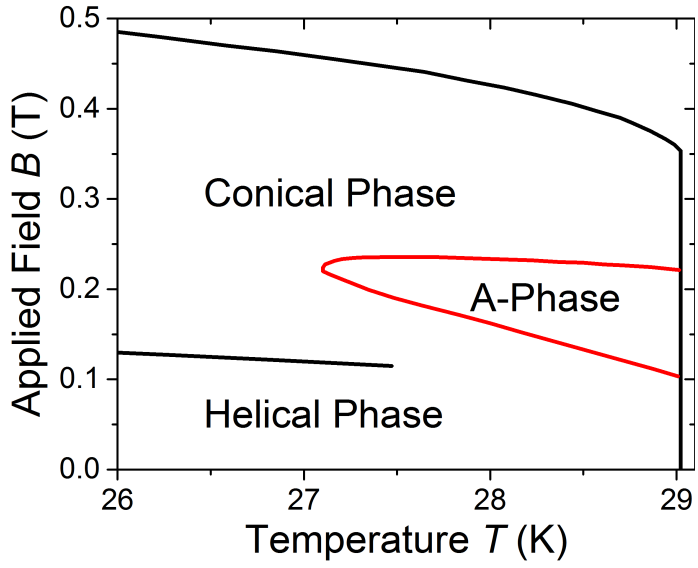

Figure 1.3: Phase diagram of bulk MnSi near the Curie temperature. Adapted from [24].

netic nature of the A-phase is currently a controversial topic, and considerable work has been performed over the years in an attempt to understand it. Kadowaki et al. performed early measurements that revealed anomalies in the magnetization and magnetoresistance at the boundaries of this phase, and suggested that it is further subdivided into two distinct magnetic phases [25]. Initial small angle neutron scattering (SANS) experiments performed soon after by Ishikawa et al. suggested that the entire A-phase was a paramagnetic phase [26]. However, later SANS studies by Lebech et al. and Harris et al. instead indicated that the A-phase is populated by

helical states with Q-vectors perpendicular to the applied field [27, 28]. A decade later, Lamago et al. performed refined SANS measurements, and found the results to be inconsistent with a simple reorientation of the helical Q vector, and instead suggested that the A-phase was a multi-dimensionally modulated structure [29]. More recent work has interpreted this phase as a skyrmion phase [30, 31].

1.2 Skyrmions

Skyrmions are topologically stable multi-dimensional solitons that arise as solutions to certain non-linear field equations. A schematic of a skyrmion is shown in Fig. 1.4.

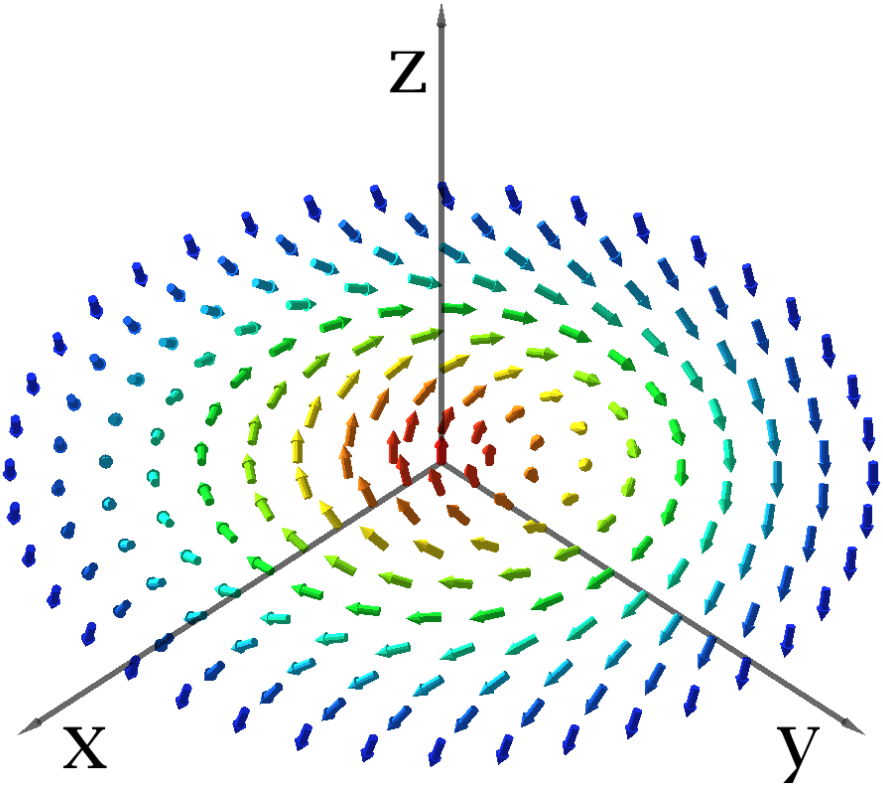

Figure 1.4: Constant M skyrmion for $\vec{B} \parallel \hat{z}$. Arrows show the direction of the magnetization at each point in space.

The idea of skyrmions was first proposed by Skyrme in the early 1960s [32]. He proposed the idea in the context of particle physics, to develop a theory that shows pions can be represented as topologically stable twists of meson fields, hence showing

how particles can arise in continuous fields. These topological objects were shown to have an integer 'twistedness' associated with them, which can be viewed as the Baryon number of the particles.

Skyrmion-like objects have since been discovered and proposed in a number of regimes outside particle physics. They have been theoretically predicted to exist in Bose-Einstein condensates by Khawaja et al. [33], and at a similar time observed by Anderson et al. [34]. In this system, skyrmions are unstable spin textures that persist for several hundred milliseconds before decaying into vortex rings [34]. Skyrmions have further been theoretically demonstrated in two dimensional Heisenberg ferromagnets by Balavin et al., [35], 2D electron gases under an applied field by Sondhi et al. [36], and in nematic liquid crystals by Bogdanov et al. [37]. Skyrmion-like objects have also been observed in chemical reaction Turing patterns by Ouyang et al. [38], and in the blue phases of crystallite liquids by Wright et al. [39].

Skyrmions were first proposed in magnetic crystals by Bogdanov et al. in 1989 [40, 41]. Later, Rößler et al. predicted the existence of skyrmions in cubic helimagnets [42, 43]. In these systems, skyrmions come about through the Dzyaloshinskii-Moriya interaction, and hence cannot form in crystals which possess inversion symmetry. However, it is possible to generate skyrmions in a material whose bulk form possesses inversion symmetry if that symmetry is broken by an interface, as was recently demonstrated by Heinze et al. in monolayers of Fe grown on Ir substrates [44]. Skyrmions in magnetic systems are of considerable interest because of their potential technological applications in magnetic data storage and computing [45, 46].

In 2009 Mühlbauer et al. and Pappas et al. independently made early demonstrations of the existence of skyrmions in a magnetic crystal, both studying the A-phase of MnSi [30, 31]. Mühlbauer et al. identified the skyrmion phase with SANS, expanding on similar measurements done by others [29, 27, 28], and re-interpreting the results based on a controversial triple-Q skyrmion model. Pappas et al. performed neutron spin echo spectroscopy measurements, and identified a disordered skyrmion phase in

this region. However, there is significant dispute in the community over the interpretation of these results. In particular, the triple-Q model used by Mühlbauer ignores the nonlinear nature of skyrmions, and theoretical work by Rößler et al. indicates that the A-phase is more complicated than their simple model suggests [47]. This is supported by the measurements of Kadowaki et al. [25] in MnSi and Wilhelm et al. in FeGe that indicate the A-phase is subdivided into a number of smaller regions [48]. Further, Grigoriev et al. have disputed the interpretation of a skyrmion phase over the entire A-phase region, and instead suggest a superposition of randomly oriented helices in some portions of this region [49].

Soon after these works on A-phase skyrmions, Yu et al. made the definitive identification of the magnetic skyrmion phase in thinned samples of $Fe_{0.5}Co_{0.5}Si$ [50]. This was a real space identification done with Lorentz microscopy, a technique which uses a defocussed transmission electron microscope to detect magnetic structure in thin samples [51]. Lorentz microscopy was further used by Yu et al. to image skyrmions in FeGe [52], and by Tonomura et al. to image skyrmions in MnSi [53]. In addition, Pfleiderer et al. have found evidence for skyrmion lattices in the small A-phase pockets of $Mn_{0.92}Fe_{0.08}Si$, $Mn_{0.98}Co_{0.02}Si$, and $Fe_{1-x}Co_xSi$ using SANS [54].

The study by Yu et al. on FeGe demonstrated that the skyrmion stability region dramatically increases as the thickness of the sample decreases , which is in line with theoretical predictions by Rößler et al. that surface anisotropies will stabilize the skyrmion phase [42, 55]. Tonomura et al. also showed that the skyrmion stability region in their thinned samples is significantly larger than the A-phase skyrmion region in bulk MnSi, although they do not present a study of multiple sample thicknesses as was done by Yu et al. These two studies form an important step towards realizing practical methods to stabilize skyrmions over broad regions of the phase diagram. However, freestanding thinned films are fragile and too small to study with many standard techniques and therefore are not an ideal material choice for further investigation or future application. Self-supported films grown epitaxially on a suitable

substrate avoid both of these problems, and thus represent a more attractive system for further study.

A number of groups have also investigated the Hall effect as it relates to the skyrmion phase in helimagnets [56] - [60]. Lee et al. studied MnSi bulk crystals and found that the anomalous Hall coefficient, R_S, can be expressed as $R_S = S_H \rho_{xx}^2 M$, where S_H is a constant that does not vary with temperature [56]. Using this fitting scheme, Neubauer et al. performed detailed measurements of the Hall effect in MnSi bulk crystals just below the Curie temperature, in the vicinity of the A-phase [57]. They found an additional component to the Hall effect in this region, which they identified as the topological Hall effect. They then use the previously calculated skyrmion density of -1 for a regular skyrmion lattice[30] to calculate the expected topological hall effect from this configuration, and find it in good agreement with their measured values. Hence, they have demonstrated that the presence of a skyrmion phase will produce a significant signature in the Hall effect. Following this work, Kanazawa et al. investigated the Hall effect in MnGe crystals and inferred the presence of a broad skyrmion region from a large topological Hall effect [59]. Similarly, Huang et al. used the topological Hall effect to infer the presence of a skyrmion phase in FeGe thin films grown epitaxially on Si(111) that is much larger than in bulk crystals [60]. Both of these works implicitly assume that the only magnetic phase that would give rise to a topological Hall effect is the skyrmion phase. This assumption is shown to be incorrect in a later section of this thesis.

1.3 MnSi Thin Films

Recently, theoretical work has been done by Butenko et al. to predict the stability of skyrmion lattices in strained epitaxial thin film helimagnets, where the strain induces a magnetocrystalline anisotropy in the film [61]. They predicted that the uniaxial anisotropy will suppress the helical and conical phases when a magnetic field

is applied in plane, leading to a much broader skyrmion stability region than seen in bulk crystals. A potentially larger skyrmion region, combined with the ease of integration with modern silicon-based electronics, makes the growth of thin films of helimagnets on silicon substrates an attractive research area.

In thin films there are additional interactions to consider in the free energy. The small thickness of the films means that the energy contribution from the demagnetizing stray field is significant. This must be taken into account by an additional term,

$$w_{demag} = \frac{1}{2}\mu_0 \vec{H}_d \cdot \vec{M}, \tag{1.3}$$

where H_d is the demagnetizing stray field. Further, strain in the films induces an easy-plane type anisotropy with the hard axis out of the plane, described by the free energy $w_a = K_u(\hat{M} \cdot \hat{n})^2$, where $\hat{n} \parallel [111]$. This anisotropy will be much larger than that induced by the weak anisotropic exchange interaction, and therefore the anisotropic exchange interaction is neglected in the following analysis. The total free energy density is therefore given by,

$$w = \frac{c}{2}M_s^2(\nabla\hat{M})^2 + b_D M_s^2 \hat{M} \cdot (\nabla \times \hat{M}) + K_u(\hat{M} \cdot \hat{n})^2 - \mu_0 \vec{H} \cdot \vec{M} + \frac{1}{2}\mu_0 \vec{H}_d \cdot \vec{M}. \tag{1.4}$$

An expression for the saturation field can be determined by substituting in the magnetization of the cone phase, equation 1.2, and then minimizing this with respect to the cone angle, φ. This must be done separately for the case of an in-plane or out-of-plane applied field, as the effect of the magnetocrystalline anisotropy and the demagnetizing field is different in the two cases. For a field applied out of plane, $\vec{H} \parallel [111]$, the demagnetizing energy density for the cone phase is given by [62] $w_{demag} = \frac{1}{2}\mu_0 M_S^2 sin^2\varphi$, and the magnetocrystalline anisotropy energy density is given by $w_a = K_u sin^2\varphi$. Substituting these two, along with equation 1.2, into equation 1.4

gives the following expression for the free energy density,

$$w = M_S^2 cos^2\varphi \left(\frac{c}{2}Q^2 - b_D Q\right) + sin^2\varphi \left(K_u + \frac{\mu_0}{2}M_S^2\right) - \mu_0 H M_S sin\varphi. \tag{1.5}$$

First, minimizing this with respect to the helical propagation vector, Q, gives a value of $Q = \frac{b_D}{c}$ which is useful to simplify the expressions determined for saturation fields. Next, the saturation field can be determined by minimizing with respect to the cone angle because, for a uniform cone phase, $sin\varphi = H/H_{C2}^{\perp}$. This minimization gives $H_{C2}^{\perp}$ as shown in Eq. 1.6.

$$\begin{aligned} \frac{\mu_0 H}{sin\varphi} &= \mu_0 H_{C2}^{\perp} = M_S(2bQ - cQ^2) + \frac{2K_u}{M_S} + \mu_0 M_S \\ \mu_0 H_{C2}^{\perp} &= M_S\left(\frac{b^2}{c}\right) + \frac{2K_u}{M_S} + \mu_0 M_S \end{aligned} \tag{1.6}$$

By defining a new parameter, $K_0 = \frac{b_D^2 M_S^2}{2C}$, which is the effective stiffness of the conical phase, the final expression for $H_{C2}^{\perp}$ becomes,

$$\mu_0 H_{C2}^{\perp} = \frac{2}{M_S}(K_0 + K_u) + \mu_0 M_S. \tag{1.7}$$

For the case of an in-plane field, $H \parallel [1\bar{1}0]$, the demagnetizing energy is given by $w_{demag} = \frac{\mu_0 M_S^2 cos^2\varphi}{4Qd}(1 - e^{-Qd}) = \frac{K_m}{2}$[62], where K_m is the total demagnetizing field contribution, and the magnetocrystalline anisotropy energy density is given by $w_a = K_u sin^2\varphi$. Proceeding similarly to the out-of-plane case, the in-plane saturation field can be expressed as follows,

$$\mu_0 H_{C2}^{\parallel} = \frac{1}{M_S}(2K_0 - K_u - K_m). \tag{1.8}$$

Experiments typically measure the values of parameters M_S, $H_{C2}^{\parallel}$, $H_{C2}^{\perp}$, and Q directly, and it is therefore useful to have expressions for K_0 and K_u in terms of these

parameters. These expressions follow directly from equations 1.7 and 1.8 and are given below.

$$K_u = \frac{M_S}{3}\left[\mu_0(H_{C2}^{\perp} - H_{C2}^{\parallel} - M_S) - \frac{K_m}{M_S}\right] \tag{1.9}$$

$$K_0 = \frac{M_S}{6}\left[\frac{2K_m}{M_S} + \mu_0(2H_{C2}^{\parallel} + H_{C2}^{\perp} - M_S)\right] \tag{1.10}$$

Finally, comparison with theoretical work presented later in this thesis requires normalization by the effective bulk zero-anisotropy saturation field, termed H_D. This field is calculated by setting $K_u = 0$, and $H_d = 0$ in equation 1.4, and minimizing as before, yielding the following expression,

$$\mu_0 H_D = \frac{2K_0}{M_S}. \tag{1.11}$$

It has been well established that MnSi films can be grown epitaxially on Si(111) substrates [62]-[70]. MnSi grows with the epitaxial relationship MnSi$[1\bar{1}0]$ $\|$Si$[11\bar{2}]$ [67]. With the lattice constants of $a_{MnSi} = 0.4561$ nm and $a_{Si} = 0.5431$ nm [71], there is a lattice misfit in this arrangement of $[a_{MnSi} - a_{Si}cos(30)]/a_{MnSi} = -3.1\%$. This lattice misfit induces a tensile strain in the films, which gives rise to an easy plane anisotropy that has significant impacts on their magnetic properties [70], and is predicted to stabilize the skyrmion phase [61].

MnSi thin films grown epitaxially have only been magnetically characterized previously by a small number of groups. The first magnetic measurements were done by Schwinge et al., and consisted of magneto-optic Kerr effect measurements at temperatures down to 10 K[72]. This data indicated ferromagnetic behavior at 10 K, but was not sufficient to determine the Curie temperature of the films. More recently, Magnano et al. grew MnSi thin films capped with Ag and performed Superconducting Quantum Interference Device (SQUID) magnetometry measurements on the films[69]. They found behavior very similar to bulk, with a Curie temperature of

30 K, a transition at 0.1 T attributed to the helical to conical transition, and a saturation field of 0.6 T. Further, a small ferromagnetic moment was found to persists above 300 K, which they attributed to Mn atoms at the Si-MnSi interface. However, more recent work by Karhu et al. disputes this explanation and instead attributes the high temperature ferromagnetism to the Ag-MnSi interface [70].

In the past couple of years, Karhu et al. have done a large amount of work characterizing the magnetic structure of Si capped MnSi thin films by a variety of methods. Early SQUID magnetometry work by this group indicated that the strain in epitaxial MnSi films causes the Curie temperature to increase significantly, up to 40 K for thicker films [70]. Further, transmission electron microscopy in this work demonstrated that both left and right handed chiral domains with sizes of the order 500 nm exist in these films, which explains the observed glassy magnetic behavior [70]. Later work presented polarized neutron reflectometry (PNR) and SQUID magnetometry measurements which gave direct evidence for the helical phase with $2\pi/Q = 13.9 \pm 0.1$ nm at 5 K [73]. The latest work by this group presents SQUID magnetometry measurements at 5 K with the applied field $H \parallel [1\bar{1}0]$ that identify one large first order transition in the majority of the films, labeled H_α, and a second, less pronounced, first-order transition, H_β, in films of thickness near $d = 4\pi/Q$ [20]. A theoretically calculated field - anisotropy phase diagram is presented which predicts a broad skyrmion stability region. However, agreement is not found between the measured and predicted transition fields. Finally, PNR measurements at 5 K on a 26.7 nm sample show that $\vec{Q}$ still points out of plane above H_β, but the profiles are explainable by neither a distorted helical phase nor a skyrmion phase.

These studies by Karhu et al. have contributed considerable understanding of the magnetic structure of these films at low temperature. However, very little work was done to determine the properties at elevated temperatures between $T = 5$ K and T_C. This thesis fills this gap by presenting a study of the magnetic properties of these films over a broad temperature range.

1.4 Magnetic Phase Transitions

Phase transitions can be broadly sorted into two categories, first-order phase transitions and second-order phase transitions. Second-order transitions occur with a continuous variation of a given order parameter, while first-order transitions have a discontinuity in this order parameter [74]. In the rest of this thesis I use the term "first-order" to refer to phase transitions that occur with a discontinuity or quasi-discontinuity in the magnetization, and "second-order" to refer to those that do not. Ideal first-order transitions with a discontinuity in the magnetization would show a delta function in the susceptibility at the transition. However, magnetic inhomogeneities in real samples cause different portions of the sample to transition at slightly different fields. This broadens the transition out into a quasi-discontinuity in the magnetization, which is indicated by a finite peak in the susceptibility.

The transition between different magnetic structures will be first-order when one structure cannot be continuously deformed into another, which causes a distinct jump in the magnetization when the new phase is suddenly created. In particular, the transition from a helical phase to a ferromagnetic phase is second-order, as the cone angle of the helicoid can vary continuously from the helical state at $\varphi = 0$ to the ferromagnetic state at $\varphi = \pi/2$. However, the skyrmion phase is topologically distinct from the ferromagnetic and helical phases, and hence cannot be continuously deformed into into these phases. Therefore, the transitions into and out of the skyrmion phase are first-order.

Another transition that can occur in helimagnets is Q-vector reorientation. This is where the Q-vector, which is originally pinned to a certain crystallographic direction by anisotropy effects, will reorient in the direct of an applied field. This transition is also seen to be first-order in measurements on bulk MnSi for certain field directions [75]. In this case, the transition is first-order because of an energy barrier created by the anisotropic exchange interaction [62].

Figure 1.5 shows a schematic of the energy in a generic first-order phase transition. It is energetically favorable for the system to transition between states one and two above the critical field H_C. However, the system will not transition continuously between these states because of the energy barrier, and the transition will only occur, abruptly, once the energy of state 1 is increased above the energy barrier. This typically occurs through increasing applied magnetic field in magnetic materials.

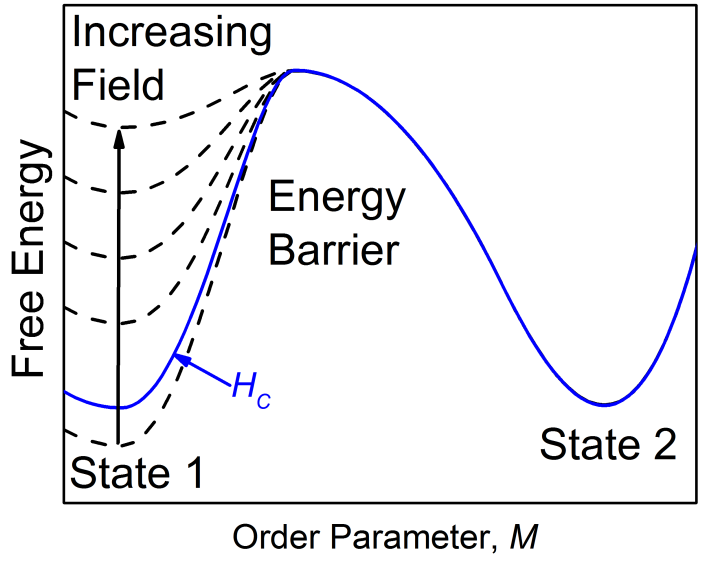

Figure 1.5: Schematic of a first-order phase transition in terms of the free energy as a function of the order parameter, M. Dotted lines indicate the free energy of state 1 in various magnetic fields. The solid blue line indicates the free energy at the critical field, H_C, where the free energy of the two states is equal.

Chapter 2

Experimental Methods

2.1 Sample Growth

Samples studied in this thesis were grown previously by Dr. E.A. Karhu. The MnSi films were grown on 300μm thick Si(111) wafers that were cleaned ultrasonically in acetone and methanol, and then in an H_2O_2/NaOH solution. The cleaned wafers were placed into a vacuum chamber with a base pressure less than 5×10^{-9} Pa, and then degassed by heating up to 600^{o}C overnight. Removal of the native Si oxide was then done by heating the wafers to 800^{o}C for 1 hour. After this, a 10-20 nm layer of Si was deposited onto the wafers at 600^{o}C. The wafers were then cooled to room temperature where a 0.5 nm layer of Mn was deposited. This Mn layer was annealed at 400^{o}C for 1 hour to produce a 1 nm template layer of MnSi. Mn and Si were then co-deposited on the surface in stoichiometric proportions at 400^{o}C until the desired film thickness was reached. Finally, the wafers were cooled to room temperature and a Si cap layer of approximately 20 nm was deposited. Further information about the film growth can be found in section 2.1 of Ref. [62].

2.2 Polarized Neutron Reflectometry

Polarized neutron reflectometry (PNR) is a technique used to characterize magnetic multilayers. Neutrons are reflected from surfaces at sufficiently low incidence angles, with the reflectivity dependent on the interaction potential of the material. As a result of the neutron's spin, neutrons interact with both the nuclei and with the magnetization of the material, allowing magnetic information to be extracted from the

reflectivity curves. In contrast to most magnetometry techniques, PNR determines the magnetization depth profile rather than the average magnetization, which makes it a powerful tool for studying non-trivial spin textures. Further, as it is layer-specific, PNR determines the magnetization of thin film layers without the influence of the substrate, allowing accurate measurements of small magnetic moments that would otherwise be lost in the magnetic response of the substrate.

2.2.1 Reflectometry Theory

The interaction of neutrons with matter is determined by the Schrödinger equation,

$$\left[\frac{-\hbar^2}{2m_n}\nabla^2 + V(\vec{r})\right]\Psi(\vec{r}) = E\Psi(\vec{r}), \tag{2.1}$$

where m_n is the neutron mass, V is the interaction potential, E is the neutron energy, and ψ is the neutron wavefunction. The potential, V, can be broken up into the nuclear potential, $V_{nuc} = \frac{2\pi\hbar^2 b\rho}{m_n}$, and the magnetic potential, $V_{mag} = g_n\mu_n\frac{\vec{\sigma}_P}{2}\cdot\vec{B}_{eff}$. Here ρ is the atomic density, b is the scattering length, $\vec{B}_{eff}$ is the effective field from the sample magnetization, $g_n = -1.913$ is the Lande factor, $\mu_n = \frac{e\hbar}{2m_n} = 5.05\times10^{-27}J/T$ is the nuclear magneton, and $\vec{\sigma}_P$ are the Pauli spin matrices:

$$\sigma_x = \begin{pmatrix} 0 & 1 \\ 1 & 0 \end{pmatrix} \qquad \sigma_y = \begin{pmatrix} 0 & -i \\ i & 0 \end{pmatrix} \qquad \sigma_x = \begin{pmatrix} 1 & 0 \\ 0 & -1 \end{pmatrix}. \tag{2.2}$$

The Schrödinger equation therefore will give solutions in the basis spin states $|+>$ and $|->$. Solutions can be expressed in the form $\Psi_+(r) =< r|+ >= a_+e^{ik_+r}$ and $\Psi_-(r) =< r|+ >= a_-e^{ik_-r}$. This gives two possible values for the wavevector,

$$k_\pm^2 = \frac{2mE}{\hbar^2} - 4\pi\rho\left(b \pm \frac{2m}{\hbar^2}\mu_n|B|\right) = \frac{2mE}{\hbar^2} - 4\pi\rho\left(b \pm b_m\right), \tag{2.3}$$

where $b_m = \frac{2m}{\hbar^2}\mu_n|B|$ is the magnetic scattering length. The general state using these wavevectors is,

$$\psi(r) = \begin{bmatrix} cos(\frac{\theta}{2}) \\ sin(\frac{\theta}{2})e^{i\phi} \end{bmatrix} (A_+e^{+i\vec{k}^+\cdot\vec{r}} + B_+e^{-i\vec{k}^+\cdot\vec{r}}) + \begin{bmatrix} -sin(\frac{\theta}{2})e^{-i\phi} \\ cos(\frac{\theta}{2}) \end{bmatrix} (A_-e^{+i\vec{k}^-\cdot\vec{r}} + B_-e^{-i\vec{k}^+\cdot\vec{r}}), \tag{2.4}$$

in terms of the polar angle θ, and azimuthal angle ϕ of $\vec{\sigma}_P$ with respect to the direction of the effective field in the medium. Using this expression, the reflectivity from a magnetic layer can be determined. First, assume a neutron beam in vacuum with $\vec{S} \parallel \vec{H} \parallel \hat{z}$. This gives the wave function in vacuum of,

$$\psi_0(r) = \begin{bmatrix} A_{0+}e^{ik^+r} + B_+e^{-ik^+r} \\ A_{0-}e^{ik^-r} + B_-e^{-ik^-r} \end{bmatrix} \tag{2.5}$$

In the case of spin-up neutrons incident on a sufficiently thick layer $B_{1+} = B_{1-} = A_{0-} = 0$, and the reflectivity and transmission coefficients can be expressed as,

$$r_{++} = \frac{B_{0+}}{A_{0+}} \qquad r_{+-} = \frac{B_{0-}}{A_{0+}} \qquad t_{++} = \frac{A_{1+}}{A_{0+}} \qquad t_{+-} = \frac{A_{1-}}{A_{0+}} \tag{2.6}$$

These reflectivity and transmission coefficients are determined by continuity of the wavefunction and its out of plane derivative ($\partial\psi/\partial z$) at the interface, which give the following four equations,

$$\begin{aligned} 1 + r_{++} &= t_{++}cos\frac{\theta}{2} - sin\frac{\theta}{2}t_{+-}e^{-i\phi} \\ r_{+-} &= t_{++}sin\frac{\theta}{2}e^{i\phi} + cos\frac{\theta}{2}t_{+-} \\ k^+_{0z}(1 - r_{++}) &= k^+_{1z}cos\frac{\theta}{2}t_{++} - k^-_{1z}sin\frac{\theta}{2}e^{-i\phi}t_{+-} \\ -k^-_{0z}r_{+-} &= k^+_{1z}sin\frac{\theta}{2}e^{i\phi}t_{++} + k^-_{1z}cos\frac{\theta}{2}t_{+-} \end{aligned} \tag{2.7}$$

Solving these equations gives the transmission and reflectivity coefficients,

$$
\begin{aligned}
t_{++} &= \frac{2k_0 z^+(k_{1z}^- + k_{0z}^-)cos\frac{\theta}{2}}{(k_{1z}^- + k_{0z}^+)(k_{1z}^+ + k_{0z}^-)sin^2\frac{\theta}{2} + (k_{1z}^- + k_{0z}^-)(k_{0z}^+ + k_{1z}^+)cos^2\frac{\theta}{2}} \\
t_{+-} &= \frac{-2k_0 z^+(k_{1z}^+ + k_{0z}^-)sin\frac{\theta}{2}e^{i\phi}}{(k_{1z}^- + k_{0z}^+)(k_{1z}^+ + k_{0z}^-)sin^2\frac{\theta}{2} + (k_{1z}^- + k_{0z}^-)(k_{0z}^+ + k_{1z}^+)cos^2\frac{\theta}{2}} \\
r_{++} &= \frac{(k_{1z}^- + k_{0z}^-)(k_{0z}^+ - k_{1z}^+)cos^2\frac{\theta}{2} + (k_{1z}^+ + k_{0z}^-)(k_{0z}^+ - k_{1z}^-)sin^2\frac{\theta}{2}}{(k_{1z}^- + k_{0z}^+)(k_{1z}^+ + k_{0z}^-)sin^2\frac{\theta}{2} + (k_{1z}^- + k_{0z}^-)(k_{0z}^+ + k_{1z}^+)cos^2\frac{\theta}{2}} \\
r_{+-} &= \frac{2k_{0z}^2(k_{1z}^- - k_{1z}^+)sin\frac{\theta}{2}cos\frac{\theta}{2}e^{i\phi}}{(k_{1z}^- + k_{0z}^+)(k_{1z}^+ + k_{0z}^-)sin^2\frac{\theta}{2} + (k_{1z}^- + k_{0z}^-)(k_{0z}^+ + k_{1z}^+)cos^2\frac{\theta}{2}}
\end{aligned}
\tag{2.8}
$$

The critical angle for total reflection can be determined from the continuity of $k_{\|}$ at the interface. This gives $cos\alpha_0 k_0 = k_1 cos\alpha_1$, where α_0 and α_1 are the incidence angle and refracted angle as shown in Fig. 2.1. Total reflection occurs when $\alpha_1 = 0$, and therefore, using the small angle approximation $cos\alpha = 1 - \frac{1}{2}\alpha^2$, the critical angle is given by $\alpha_c = \sqrt{2}\sqrt{1-n}$, where n is the refractive index, $n = \frac{k_1}{k_0}$.

As a specific example, consider B to be small in vacuum, and magnetization in the medium such that $\theta = 0$, $\phi = 0$. First, a small B in vacuum implies $k_0^{\pm 2} \approx \frac{2me}{\hbar^2}$ and therefore $n = \sqrt{1 - \frac{4\pi}{k_0^2}\rho(b \pm b_m)} \approx 1 - \frac{2\pi}{k_0^2}\rho(b \pm b_m)$. This gives $\alpha_c = \frac{\sqrt{4\pi\rho(b \pm b_m)}}{k_0}$. Next, the reflectivity coefficients are given by,

$$
\begin{aligned}
r_{++} &= \frac{k_{0z}^+ - k_{1z}^+}{k_{1z}^+ + k_{0z}^+} \\
r_{+-} &= 0 \\
r_{--} &= \frac{k_{0z}^+ - k_{1z}^-}{k_{1z}^- + k_{0z}^+} \\
r_{-+} &= 0
\end{aligned}
\tag{2.9}
$$

The magnetization causes the critical angle to be different for incident spin-up or

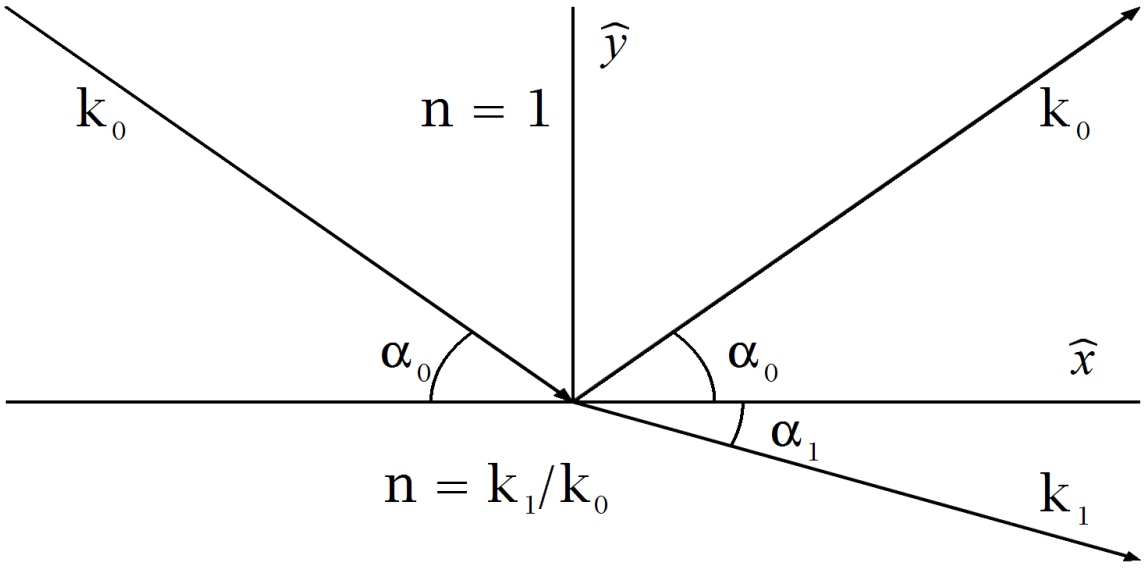

Figure 2.1: Reflected and refracted angles for a neutron impinging on an interface from vacuum.

spin-down neutrons, and gives a reflectivity curve as shown below in Fig. 2.2 for the case of the reflectivity from a thick magnetized iron sheet. In this figure, the reflectivity is plotted as a function of the scattering vector, defined as $q = 4\pi sin\alpha/\lambda_n$, where α is the neutron incidence angle, and λ_n is the neutron wavelength. Reflection from a sample consisting of multiple distinct layers is determined by considering iteratively the continuity of the wavefunction and its derivative at each interface. This can be calculated recursively from the back infinitely thick substrate through to the vacuum following Parrat's method developed for x-ray reflectometry [76]. Interference between reflection from the layers causes oscillating fringes to appear in the reflectivity, as shown in Fig. 2.3 (a) for a 50 nm Co layer on top of an infinitely thick Fe substrate. The width of these fringes varies strongly with the thickness of the layers.

Realistic materials do not contain infinitely sharp boundaries, and always have some roughness, or intermixing, at the interfaces between two materials. This can be taken into account by assuming the following form for the scattering length density,

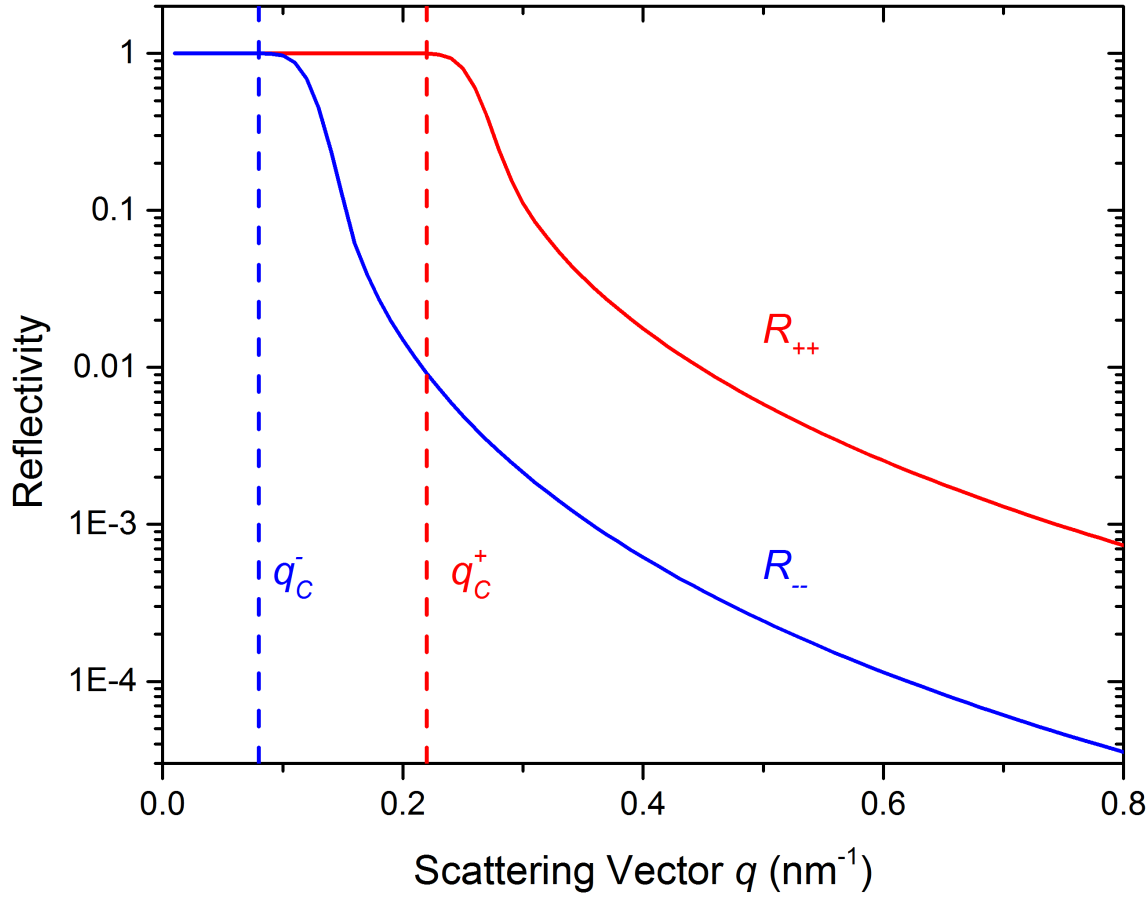

Figure 2.2: PNR from a magnetized Fe surface, with a uniform magnetization perpendicular to the scattering plane.

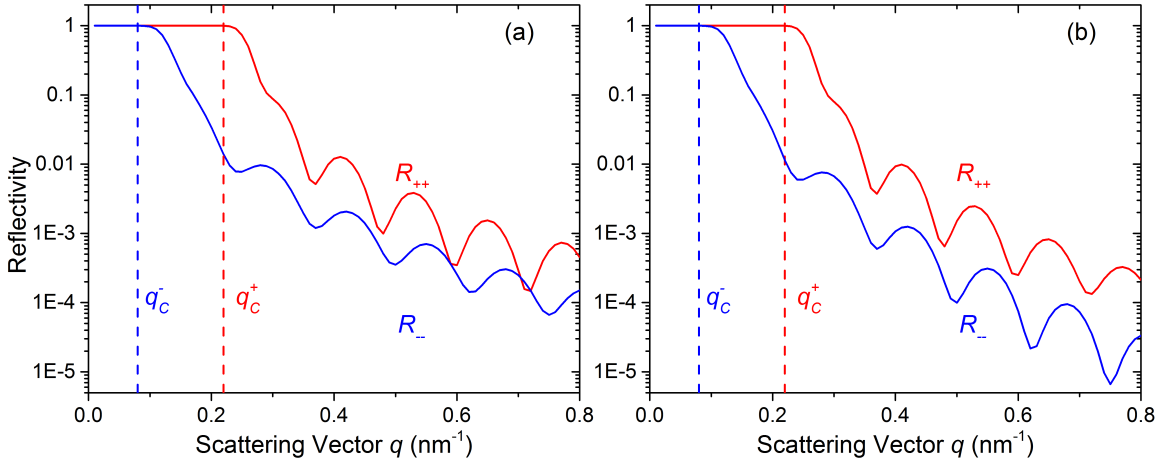

Figure 2.3: PNR from a 50 nm Co layer on a Fe substrate for (a) no interface roughness , (b) roughness with $\sigma = 2$ nm.

defined as $SLD = \rho b$,

$$SLD = SLD_1 + \frac{SLD_1 - SLD_2}{2}\left[1 + erf\left(\frac{y-d}{\sqrt{2}\sigma}\right)\right], \tag{2.10}$$

where y is the depth in the material, σ is the characteristic diffusion length, and d is the layer thickness. This gives an SLD profile as shown by the black line in Fig. 2.4. Reflectivity for this arrangement can be calculated by discretizing the SLD profile into a number of layers, as shown with the blue line in Fig. 2.4, and then applying Parratt's recursive formalism to the structure with these layers. As an example, the reflectivity from the aforementioned 50 nm Co layer on top of an Fe substrate with $\sigma = 2$ nm roughness at the interfaces gives the reflectivity curve shown in Fig. 2.3 (b), which drops in intensity more quickly with increasing q than the simulation for $\sigma = 0$. The reflectivity curves shown here, as well as fit curves shown later in this thesis, are generated using the Simulreflec software package that calculates the reflectivity from a defined multilayer structure using the Parratt formalism [77].

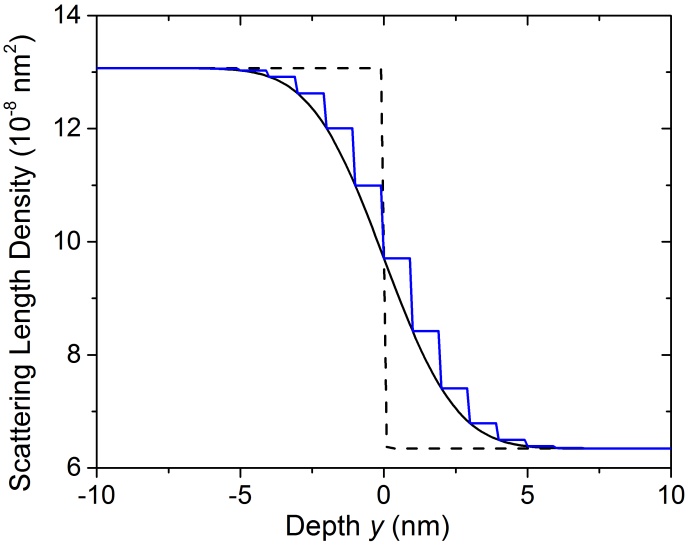

Figure 2.4: Scattering length density for a spin-up neutron at the interface between saturated Co ($y > 0$) and Fe ($y < 0$). Dashed line shows SLD with no roughness, solid black line shows the SLD with roughness $\sigma = 2$ nm, and solid blue line shows the SLD with roughness $\sigma = 2$ nm discretized into 1 nm layers.

2.2.2 D3 Reflectometer

PNR measurements presented in this thesis were gathered on the D3 reflectometer at Chalk River Laboratories with the assistance of Dr. H. Fritzsche. Figure 2.5 shows a schematic of the setup of this instrument. It uses a graphite focusing monochromater followed by a pyrolytic graphite (PG) filter to produce a beam of neutrons with wavelength 0.237 nm. This beam is then polarized using an Fe/Si supermirror to produce a spin-up neutron beam, and flipped to a spin-down beam, if required, using a Mezei type precession spin flipper [78] before impinging on the sample. A spin flipper and Heusler alloy spin analyzer after the sample allow measurement of the spin-flip signals. Finally, the neutrons are detected by a 32-wire He detector. In

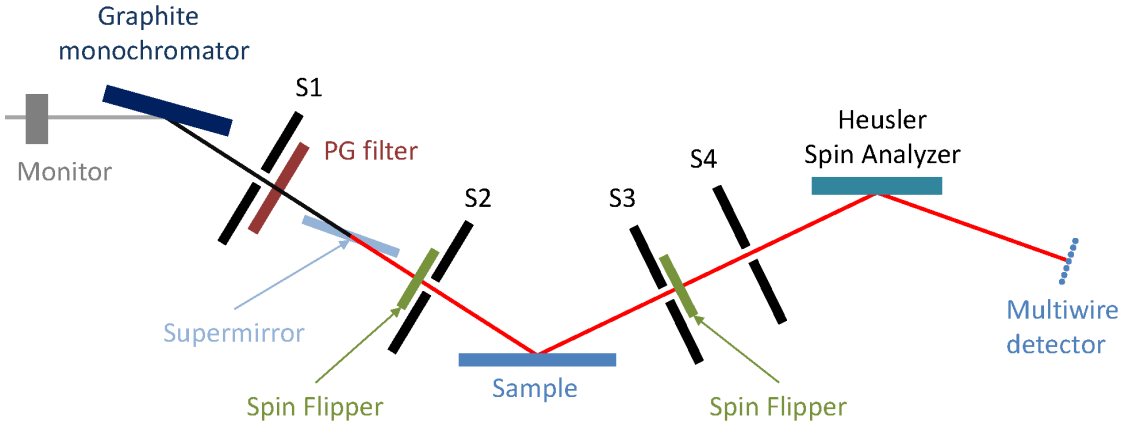

Figure 2.5: Schematic of the D3 reflectometer at Chalk River Laboratories.

this thesis I did not measure the spin-flip component of the reflectivity as it was shown to be very small in similar measurements by Karhu et al. as a result of the chiral domains in these films [20]. Hence, the Heusler alloy was only used to determine the spin-flip ratio, a measure of the polarization of the beam. The spin-flip ratio, $SPFR$, is determined by passing a nominally spin-up polarized beam directly through the setup with the sample out of the beam, and measuring the spin-up and spin-down components of this beam using the spin flipper and Heusler spin analyzer. This value is defined as the ratio between the spin-up and spin-down components of

this measurement, and is used to adjust the calculated reflectivity fits to the finite polarization of the measured curves. This correction is done by adding a portion of the opposite spin to the fits calculated for an ideal infinite spin-flip ratio using the following relations,

$$\begin{aligned} R^{--}_{corr} &= R^{--}(1 - \frac{1}{SPFR+1}) + \frac{R^{++}}{SPFR+1}, \\ R^{++}_{corr} &= R^{++}(1 - \frac{1}{SPFR+1}) + \frac{R^{--}}{SPFR+1}, \end{aligned} \tag{2.11}$$

where R^{++} and R^{--} are the measured spin-up and spin-down reflectivities.

The magnetic field at the sample was provided by a split coil cryomagnet, allowing measurement in fields up to several Tesla. However, to retain neutron beam polarization, a non-zero field parallel or anti-parallel to the neutrons spin must be present at all points in space. This requires running the cryomagnet in asymmetric mode, with the bottom coil producing a larger field than the top coil [79]. This results in a small variation in the applied field over the sample surface that had to be taken into consideration when planning the experiments. In particular, data points near transition fields were not measured to avoid the possibility of different portions of the sample being in different magnetic states.

Measurements were conducted by varying the sample and detector angle together to produce a $\theta - 2\theta$ spectrum, which is plotted in terms of the scattering vector, q, defined above. The sample was overilluminated at all incidence angles, with the length of the beam projected on the sample plane, l, being larger than the sample length, L, as shown in Fig. 2.6. Therefore, the footprint of the sample as a fraction of the projected beam length can be written as, $f = L/l = Lsin\alpha/S_w$. This represents the fraction of the total neutron beam that is incident on the sample at a given incidence angle. In PNR experiments we directly measure the neutron intensity that is reflected from the film for a given total incident beam intensity. To compare the sample reflectivities at different incidence angles we therefore must correct for the

sample footprint by dividing each measured reflected intensity by $sin\alpha$. Further, as the neutron flux from the reactor is variable, a low-efficiency monitor counter is placed before the monochromator and the count rates at each data point are normalized by the monitor count rate. Background subtraction was done by measuring a $\theta - 2\theta$ reflectivity curve with the sample angle offset by 0.5^o, and subtracting these values from all other measured $\theta - 2\theta$ curves.

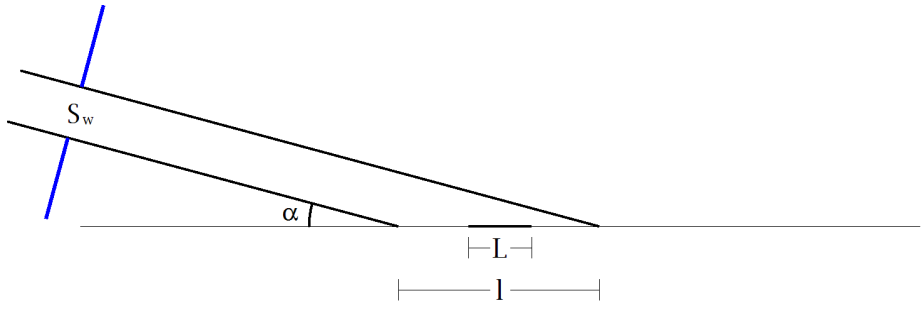

Figure 2.6: Diagram of the length of the beam on the sample plane, l, for a beam width defined by a slit of width S_w. In this diagram α is the incidence angle and L is the sample length

2.3 SQUID Magnetometry

Supconducting quantum interference device (SQUID) magnetometry is an extremely sensitive technique that can measure magnetic moments as low as 10^{-8} emu. This makes it a useful tool for studying the magnetic properties of small magnetic samples. As a result, it has become the standard method of measuring sample magnetization in recent years.

This magnetometry technique relies on Faraday's law of magnetic induction. A time varying magnetic flux, Φ_M, through a loop induces an electromotive force, ϵ, in the loop, given by $\epsilon = -\frac{d\Phi_M}{dt}$, which in turn generates a current in the loop.

Figure 2.7 shows a diagram of the magnetometer pick-up coil. The coil shown is a second-order gradiometer. This is sensitive to the second-order spatial derivative of the time varying flux, rather than the flux itself, which helps eliminate some sources

of background. The magnetic sample is mounted in a plastic straw inside of the conducting loops, where an external magnetic field can be applied. A magnetic field is also present around the sample as a result of its intrinsic magnetization. When the sample is moved vertically past the conducting loops, a time varying magnetic flux is created through these loops from the magnetization of the sample. This causes a current to flow through the fifth conducting loop, labelled P, which produces an emf in the SQUID sensor.

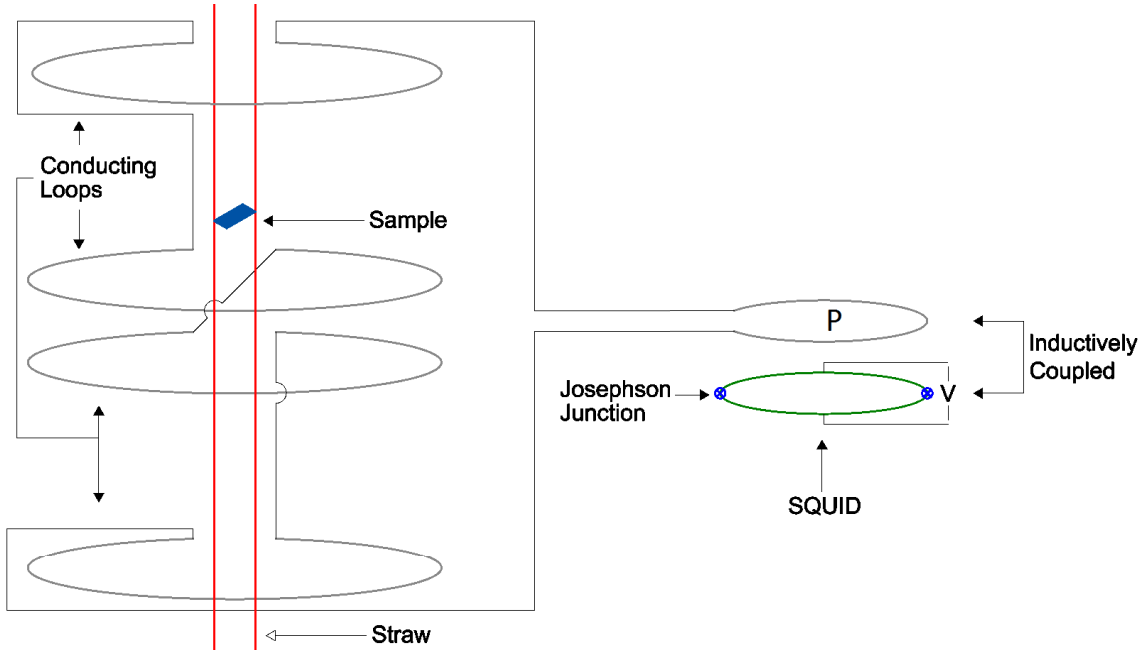

Figure 2.7: Diagram of the SQUID magnetometer with 2nd order gradiometer setup. Translating the sample through the conducting loops induces a current in these loops which is transmitted to the SQUID sensor and read by the voltage produced across this sensor.

The SQUID sensor consists of a superconducting wire loop broken by two Josephson junctions. When a magnetic flux is introduced inside a loop of superconducting wire, a current will be induced in this wire that attempt to cancel out the magnetic flux. However, the magnetic flux inside a superconducting loop is quantized in units of the flux quantum, $\frac{h}{2e} = 2.07 \times 10^{-15}$Wb, where h is Planck's constant, and e is the charge of an electron [80, 81]. Therefore, the induced current in the superconducting

loop will oscillate as the flux is increased in order to bring the total flux to the nearest integer multiple of the flux quantum. This current can be read as an output voltage because of the presence of the two Josephson junctions in the loop.

Josephson junctions are thin insulating boundaries that are placed between two superconducting wires. It was first predicted by Josephson in 1962 that a current would flow through an insulating boundary between superconducting wires with no voltage drop, provided the current was low enough [82], and this was first observed in 1963 by Anderson et al. [83]. The voltage across this junction will begin to increase above zero once a critical current is reached. SQUID sensors use a bias current applied across the superconducting loop, as shown in Fig. 2.8, to raise the current above the critical current required for a non-zero voltage. With this bias current applied, any small change in the flux through the superconducting loop will result in a large change in the voltage across the Josephson junctions. This allows for the accurate measurement of magnetic moments in SQUID magnetometry.

SQUID magnetometry measurements in this thesis were collected on a Quantum Design MPMS SQUID magnetometer. All measurements were conducted with the reciprocating sample option (RSO) mode of this device. The RSO mode oscillates the sample vertically about the center of the coils, and measures the SQUID voltage as a function of position, which gives a curve as shown in Fig. 2.9. The measured voltage curve is then fit to obtain the magnetic moment with the following equation,

$$V = z+l_oP+\mu\eta[2(r^2+[P-\gamma]^2)^{-1.5}-(r^2+[\beta+(P-\gamma)]^2)^{-1.5}-(r^2+[-\beta+(P-\gamma)]^2)^{-1.5}], \tag{2.12}$$

where z is the sample position that aligns the sample with the center of the coils, l_o is a linear offset, P is the position of the sample, r, γ, and β are geometric parameters of the coil setup, η is a sensitivity factor, and μ is the magnetic moment of the sample.

The SQUID magnetometer measures the average magnetic moment of the entire sample. The samples mounted in the straws consisted of cleaved pieces of the wafers

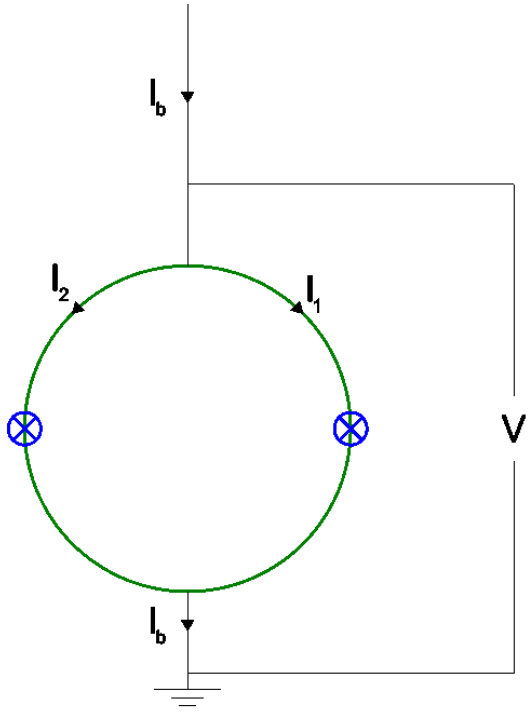

Figure 2.8: SQUID sensor schematic. I_b is the bias current applied to the SQUID sensor, and I_1 and I_2 are the currents that will pass through each Josephson junction. The net circulating current in the sensor will be $I_2 - I_1$.

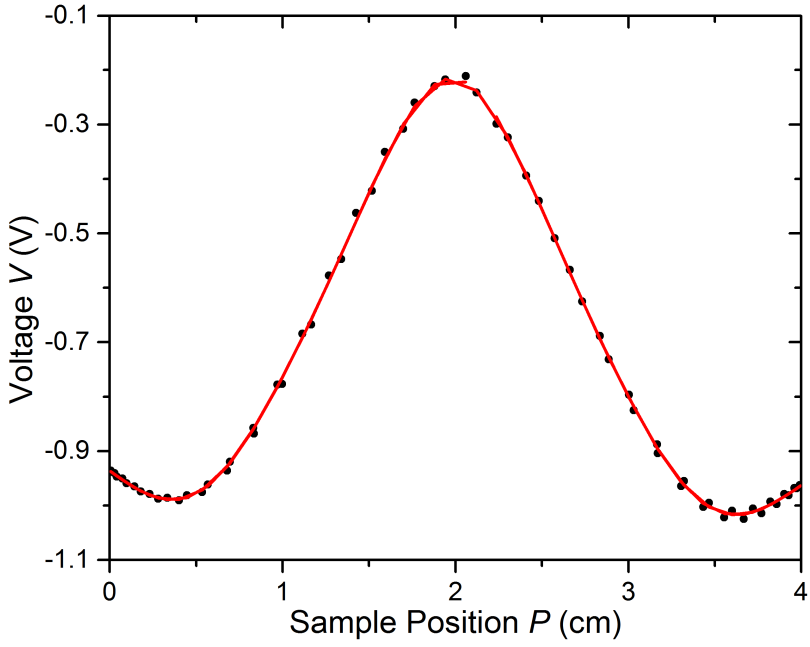

Figure 2.9: Sample RSO output voltage curve. The black circles show the measured voltage, while the red line shows the voltage fit, as described in the text.

with the deposited thin films, and therefore include the Si substrate. This substrate is roughly four orders of magnitude thicker than the thin film of MnSi, and therefore the small diamagnetic response of the Si results in a significant background to the measurement of the magnetization of the thin film. For the magnetization measurements with an applied field in-plane, the substrate background was subtracted by fitting the magnetic moment at high field, as shown in Fig. 2.10, and subtracting the slope, χ_{Si}, from the measured magnetic moment. The magnetization in kA/m was then calculated as $M = (\mu - \chi_{Si}\mu_0 H)/v$, where v is the sample volume. The substrate background correction for the measurements with an applied field out-of-plane will be discussed in chapter 4.

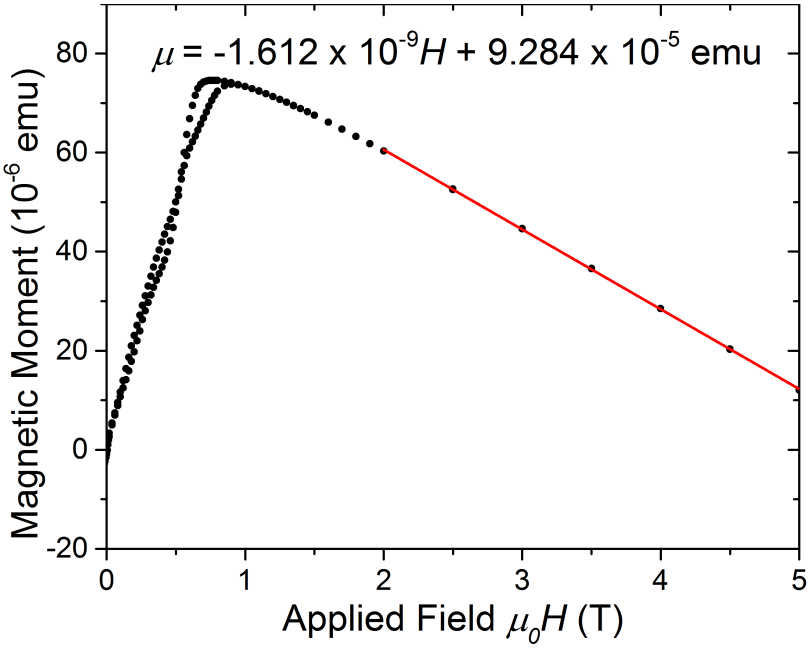

Figure 2.10: Fitting of the magnetic moment at high field for the subtraction of the substrate background. The black circles show the measured magnetic moment generated from fitting the SQUID voltage, and the red line shows the fit to this data at high field. The equation for the fit is shown on the graph.

To detect magnetic phase transitions, two types of magnetization curves were measured in this thesis: $M - H$ curves, and $M - T$ curves. As shown in Fig. 2.11, changes in M observed in $M - H$ scans are more sensitive to phase boundaries with

a weak temperature dependence that are close to horizontal on a field-temperature phase diagram. By contrast, $M-T$ curves are more sensitive to phase boundaries with a weak field dependence that are closer to vertical on a $H-T$ plot. Therefore, these two types of scans are complimentary and allow any transition on a field-temperature phase diagram to be detected.

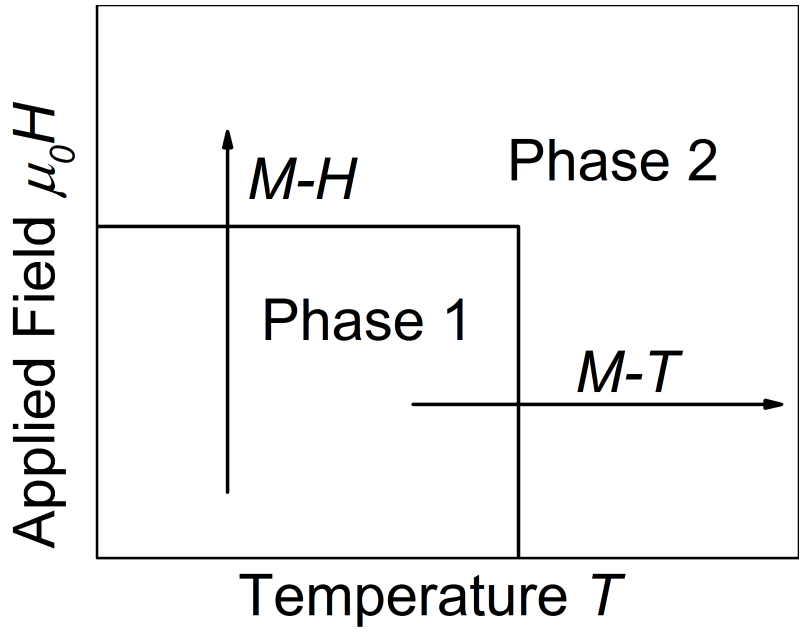

Figure 2.11: A schematic representation of a field-temperature phase diagram with one phase boundary that is vertical, and one that is horizontal. The arrows represent how the phase diagram is sampled by $M-H$ and $M-T$ scans.

The $M-H$ curves were measured by setting the temperature to the desired value, and then applying a field of 5 T or -5 T to saturate the sample. The field was then changed in discrete steps and the magnetization measured at each field value. For each field, multiple RSO voltage curves were measured, and the fit moments were averaged together. The $M-T$ curves were measured by heating the samples to 100 K, well above the Curie temperature, applying the desired magnetic field, cooling the sample to 5 K, and then measuring the magnetization upon warming the sample. Again, the temperature was changed in discrete steps, multiple RSO voltage curves were measured at each temperature, and the fit magnetic moments were averaged

together.

2.4 Electrical Transport Measurements

Electrical transport measurements are a valuable tool that can give insight into the electrical and magnetic properties of materials. To perform transport measurements, a portion of a 25.4 nm sample was patterned into the Hall-bar arrangement shown in Fig. 2.12 using SPR220-3.0 photoresist, and then etched using Ar-ion bombardment. Gold wire leads were then soldered onto the surface using indium solder applied at approximately 200 ^{o}C, below the temperature expected to cause significant structural changes in the film [65].

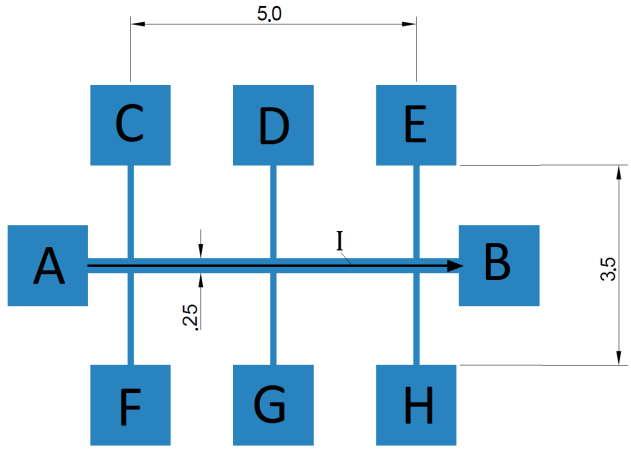

Figure 2.12: Hall bar geometry used for measuring longitudinal resistivity and Hall effect. In this figure all dimensions are in millimeters, and I is the current.

2.4.1 Longitudinal Resistivity

The longitudinal resistivity of the patterned sample was measured by passing a current between leads A and B and simultaneously measuring the voltage, V_L, between leads C and E. The resistivity, ρ_{xx}, is then given by,

$$\rho_{xx} = \frac{(V_L)(25.4 \text{ nm})(0.25 \text{ mm})}{I(5 \text{ mm})}. \tag{2.13}$$

These measurements were performed in a Quantum Design PPMS that allowed control of the temperature between 2 and 300 K and applied field up to 9 T. The Hall voltage, V_H, was simultaneously measured between leads E and H.

2.4.2 Hall Effect

Hall Effect Theory

The Hall effect is a transverse voltage that is produced across a current-carrying conductor in a magnetic field applied perpendicular to the current flow, as shown in Figure 2.13 for a non-magnetic material. In this figure, V_H is the Hall voltage, I is the current, H is the magnetic field, w is the width of the conductor, and d is the thickness of the conductor. When charges move in a magnetic field, they feel a force called the Lorentz force, $\vec{F_L} = q(\vec{v} \times \mu_0 \vec{H})$, where q is the charge, and $\vec{v}$ is the velocity of the charge. This force causes the charge carriers to accumulate on one side of the conductor, which gives rise to the observed Hall voltage that is proportional to the applied field. The Hall resistivity is defined as,

$$\rho_{yx} = \frac{V_H d}{I}, \tag{2.14}$$

and is the quantity typically reported from experiments.

In nonmagnetic materials, the Hall resistivity follows the above model, and can be expressed as, $\rho_{yx} = R_0 \mu_0 H$, where R_0 is the ordinary Hall coefficient. This coefficient can be related to the charge carrier density of the material, n_C. In equilibrium, the Lorentz force will be equal to the electric force generated by the displaced electrons, $|F_L| = -ev\mu_0 H = -eE = -eV_H/w$, where e is the electron charge. The electron velocity can be related to the current by, $I = -en_C vdw$, which gives,

$$\frac{-I\mu_0 H}{en_C dw} = V_H w = \frac{\rho_{yx} I}{dw}. \tag{2.15}$$

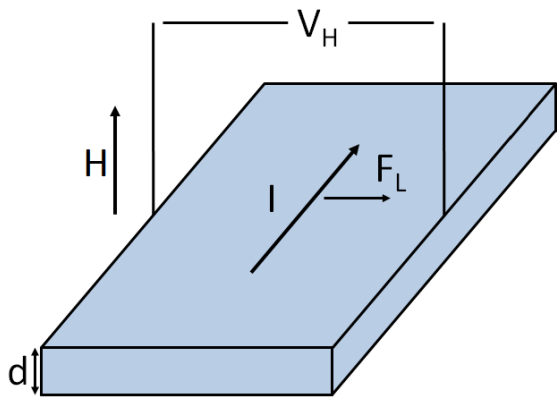

Figure 2.13: Schematic of the Hall effect for a magnetic field, H, applied to a conductor of width w and thickness d carrying current I. V_H is the Hall voltage and F_L is the force felt by the electrons.

Therefore, $\rho_{yx}\mu_0^{-1}H^{-1} = -(en_C)^{-1}$, and $R_0 = -(en_C)^{-1}$.

In magnetic materials, the Hall effect is more complicated. It has been known since the late 19th century that ferromagnetic conductors have a Hall effect that is significantly larger than that derived from the above explanation. This is termed the anomalous Hall effect and has been the topic of considerable study over the years [84]. The anomalous Hall effect is proportional to the magnetization, M, of the material, which gives the following expression for the Hall resistivity,

$$\rho_{yx} = R_0\mu_0 H + R_S M, \tag{2.16}$$

where R_S is the anomalous Hall coefficient. The anomalous Hall coefficient comes from three distinct mechanisms, called the intrinsic, skew, and side jump contributions. The intrinsic contribution was first explained by Karplus and Luttinger and comes about from a velocity contribution given by inter-band coherence in an applied electric field [85]. This contribution has also recently been linked to the topology of the bands, and the Hall conductivity, σ_{yx}, is independent of the transport lifetime, τ [84]. The intrinsic Hall resistivity is given by $\rho_{yx}^{int} = \rho_{xx}^2\sigma_{yx}^{int}$.

The second two contributions both come from impurity scattering. Skew scattering results from asymmetric scattering from impurities caused by spin-orbit coupling[84]. This contribution is proportional to the transport lifetime, $\sigma_H^{skew} \propto \tau$, which is also proportional to the longitudinal conductivity, σ_{xx}. Therefore, the Hall resistivity from this arrangement will be directly proportional to the longitudinal resistivity. Side-jump scattering is the impurity scattering that is independent of the transport lifetime, and comes from a transverse displacement experienced upon scattering from a spherical impurity [84]. This contribution will have the same ρ_{xx}^2 dependence as the intrinsic contribution, and therefore it is difficult to distinguish between the two in experiments.

There is also an additional component to the Hall effect that can be observed in chiral magnets, called the topological Hall effect. This effect comes about from the geometric phase, called the Berry Phase [86], that electrons pick up when moving through a spatially varying magnetic field. This phase factor creates an effective magnetic field felt by the electrons and hence contributes to the Hall effect. The effective magnetic field is proportional to the skyrmion density, Φ, which can be calculated as follows, [87]

$$\Phi = \frac{1}{4\pi}\hat{m} \cdot \left(\frac{\partial \hat{m}}{\partial x} \times \frac{\partial \hat{m}}{\partial y} \right). \tag{2.17}$$

In the continuum limit, the skyrmion density is proportional to the spin chirality, $SC = S_i \cdot (S_j \times S_k)$, where $S_{i,j,k}$ are adjacent spins [59]. This means that the effect will only be present for spin structures that have a net chirality, and spins which are non-coplanar. Therefore, the simple helical and conical phases in Fig. 1.2 cannot produce a topological Hall effect, while the skyrmion phase can.

Hall Effect Experiment

The Hall effect was measured on the 25.4 nm patterned sample shown in Fig. 2.12 using the Quantum Design PPMS system, and the raw Hall resistivity was determined according to Eq. 2.14. However, slight misalignment of the leads used to measure the Hall effect introduces a small component of ρ_{xx} into the measured ρ_{yx}, which must be removed for proper analysis. The Hall resistivity is necessarily antisymmetric in field, while ρ_{xx} is symmetric in field. Therefore, to remove this ρ_{xx} contribution from the Hall resistivity data, I use $\rho_{yx} = (\rho_{yx+} - \rho_{yx-})/2$ as a true measure of the Hall resistivity, where ρ_{yx+}, ρ_{yx-} are the positive and negative field portions of the raw data.

Chapter 3

Magnetic Properties with $\vec{H} \parallel [1\bar{1}0]$

Prior magnetic studies of MnSi thin films focused on the low temperature magnetic behavior, at or near 5 K [70, 73, 20]. In this chapter, I expand upon prior work by presenting a study of the magnetic behavior of MnSi thin films over a broad temperature range with an applied field in-plane along the $[1\bar{1}0]$ axis. The studied films were grown by molecular beam epitaxy as described in section 2.1, and have been previously magnetically characterized at low temperatures [20]. This characterization identified the helical and conical phases but found no low temperature skyrmion phase. The new PNR and SQUID measurements presented in this chapter show that these films do exhibit a skyrmion phase at elevated temperatures, which persists over a broad field range.

3.1 SQUID Magnetometry

Detailed SQUID magnetometry measurements were performed on five films of thicknesses 18.3, 23.6, 25.4, 26.7 and 29.8 nm. Each of the films was grown on a Si(111) substrate and capped by an amorphous layer of silicon with a thickness close to 20 nm. As the results are very similar for all of the films, the detailed analysis is only shown for one film at $d = 26.7$ nm with the results of the rest of the films summarized into a field-anisotropy phase diagram at the end of this section. This $d = 26.7$ nm film was previously found to have a 26.3 nm layer of pure MnSi, with a 0.4 nm layer of mixed MnSi/Si at the boundary with the amorphous cap [62].

I first present a series of $M - H$ curves at representative temperatures for the $d = 26.7$ nm MnSi thin film in Fig. 3.1. These plots show that there is significant

hysteresis present at low temperature that vanishes at higher temperatures. Further, there is clear evidence for multiple first-order phase transitions in the distinct slope changes on the plots, including one transition near $B = 0.3$ T that appears on the $T = 15$ and 35 K plots, but not the 5 K plot. To better characterize these transitions, the static susceptibility was calculated from this data by taking the derivative of magnetization as a function of applied field.

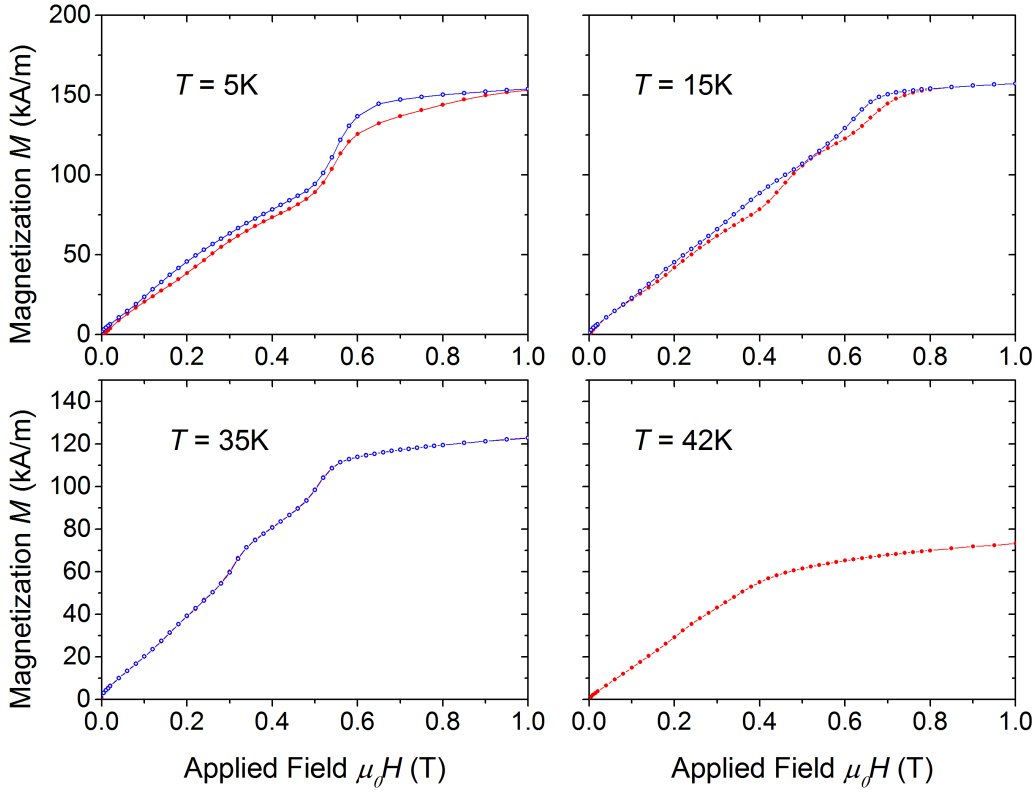

Figure 3.1: Magnetization curves as a function of field for representative temperatures of a $d = 26.7$ nm MnSi thin film.

Figure 3.2 shows a series of susceptibility curves calculated from the $M-H$ curves in Fig. 3.1, as well as from similar measurements at intermediate temperatures. In addition to the two peaks previously identified at $T = 5$ K by Karhu et al. [20], these plots show a third peak that arises at higher temperatures. These three peaks are labeled H_β, $H_{\alpha 1}$, and $H_{\alpha 2}$, and indicate three first-order transitions. Ideally, first-order transitions would appear as extremely sharp peaks in the susceptibility,

but inhomogeneities in the films caused by, among other factors, the chiral domains observed by Karhu et al. [70], causes these transitions to be broadened into the peaks shown in Fig. 3.2.

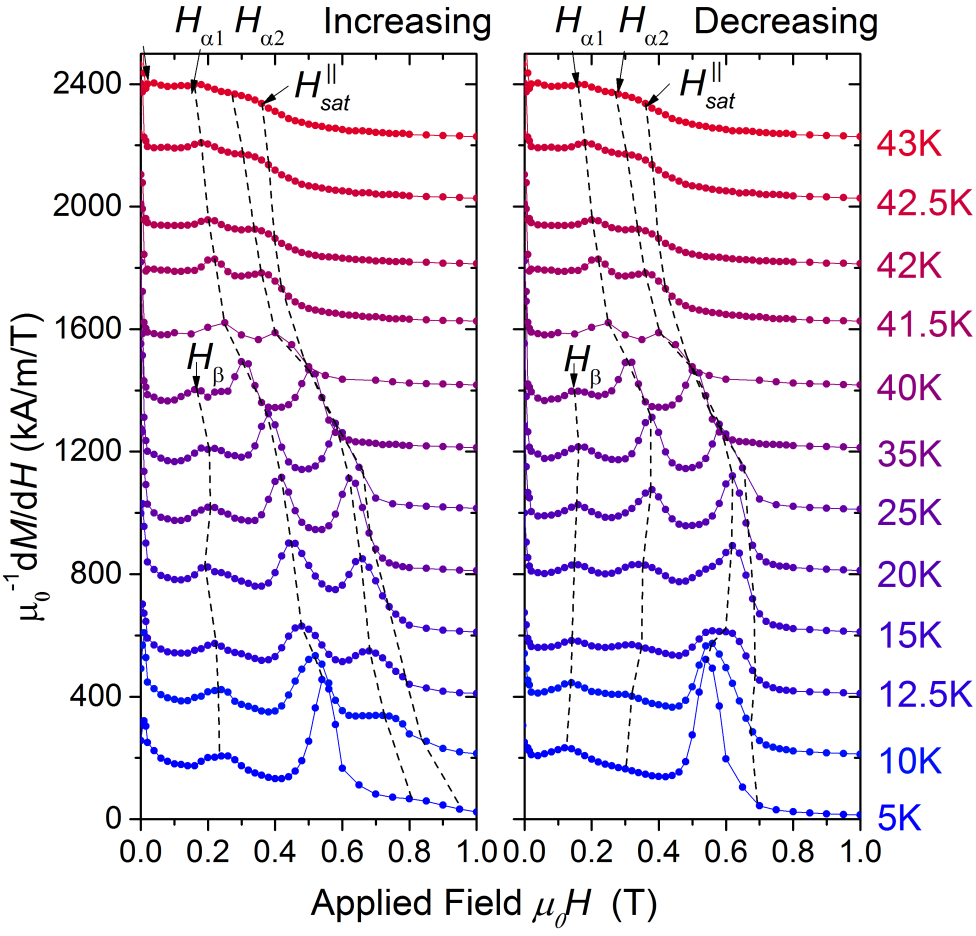

Figure 3.2: Magnetic susceptibility curves as a function of field for a 26.7 nm MnSi film. These curves were calculated from the derivative of hysteresis curves for increasing and decreasing field branches separately.

The field value of each transition was determined by fitting each peak to a gaussian. The saturation field, $H_{sat}^{\parallel}$, was determined from the magnetization curves by the intersecting line method, as demonstrated in Fig. 3.3 for a curve at $T = 15$ K. This method involves extrapolating a line from the slope just below saturation and a line from the slope just above saturation. The field value where these two lines intersect is then taken as the saturation field. In previous analysis of these films,

$H_{sat}^{\parallel}$ was determined by the position of a minimum in $\frac{d^2M}{dH^2}$. However, I was unable to consistently find a minimum corresponding to saturation at all temperatures, and hence the line intersection method was used for consistency. This method involves some estimation of the characteristic slope above and below saturation, and hence is the main source of uncertainty in the analysis that follows.

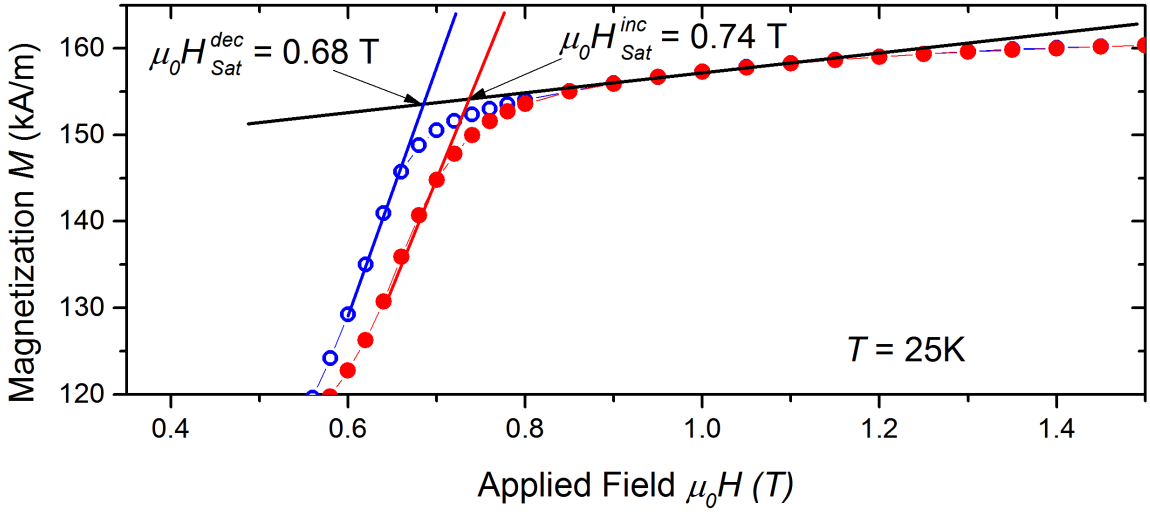

Figure 3.3: Demonstration of the method used to determine the saturation field. Red filled circles show increasing field magnetization, while the blue open circles show decreasing field magnetization. Red, black, and blue lines are manually drawn to track the slope of the susceptibility just above and below saturation.

It is instructive to compare the measured magnetization curves to curves calculated theoretically for known magnetic phases. U.K. Rößler, A.B. Butenko, and A.N. Bogdanov calculated the magnetization curves expected for these films from Eq. 1.7 by relaxing the system to the minimum energy state using simulated annealing. This calculation used periodic boundary conditions and assumed the saturation magnetization, M_S, was constant over the film. Surface anisotropies were only included as an additional contribution to the effective volume anisotropy, K_u. Further details on the calculation can be found in Ref. [61]. This calculation revealed helical and conical phases, and well as a regular skyrmion lattice with cores parallel to the film surface, as shown in Fig. 3.4.

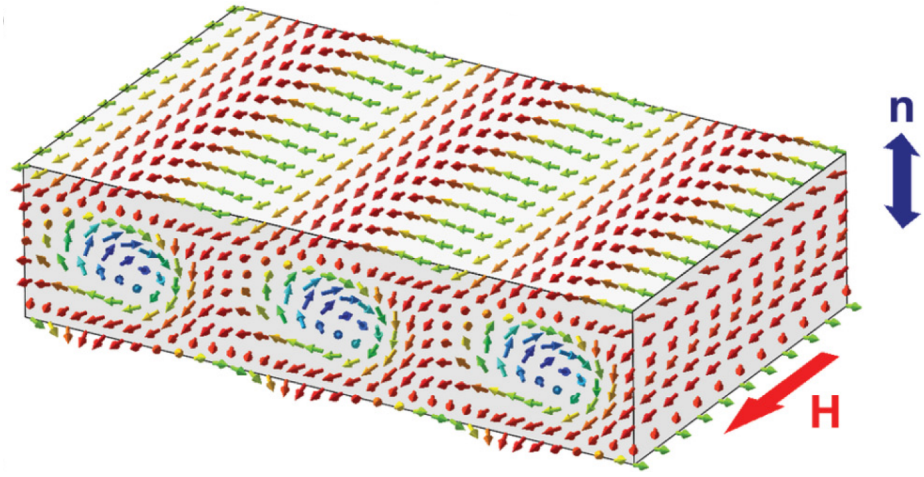

Figure 3.4: Skyrmion lattice determined by energy minimzation calculations with $H||[1\bar{1}0]$

In order to properly compare with these curves, the anisotropy (K_u/K_0) and effective bulk saturation field (H_D) were calculated from the in-plane and out-of-plane saturation fields following equations 1.11, 1.12 and 1.13. The out-of-plane saturation fields, $H_{sat}^{\perp}$, were determined from $M-H$ curves measured with an out-of-plane field at each temperature. Here, a clear minimum in the second derivative was fit to obtain the saturation field, as shown in Fig. 3.5.

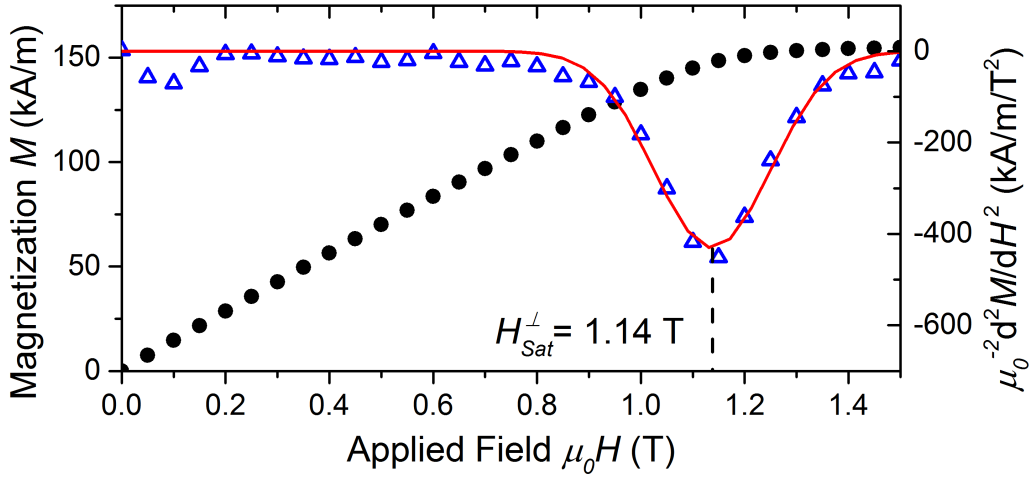

Figure 3.5: Magnetization curve (solid black circles) and $\mu_0^{-2}d^2M/dH^2$ (open blue triangles) along with a gaussian fit (red line) to the peak in $\mu_0^{-2}d^2M/dH^2$ for the $d = 26.7$ nm film with $H \parallel [111]$ at $T = 15$ K.

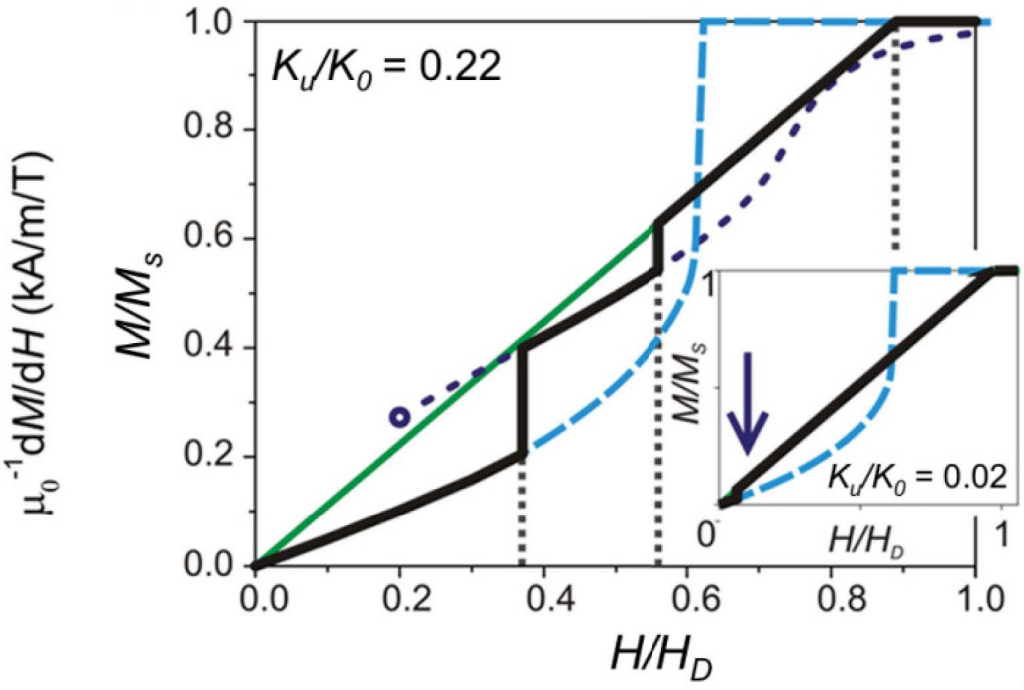

Figure 3.6: Calculated magnetization curve for MnSi film with $K_u/K_0 = 0.22$, corresponding to $T = 15$ K, $d = 26.7$ nm. The green solid line indicates the magnetization for a conical phase, the blue dashed line shows the magnetization for the helical phase, and the dotted navy line shows the magnetization for the skyrmion phase. The black solid line follows the minimum energy state. Inset: Magnetization curve for MnSi film with $K_u/K_0 = 0.02$ corresponding to $T = 42$ K, $d = 26.7$ nm.

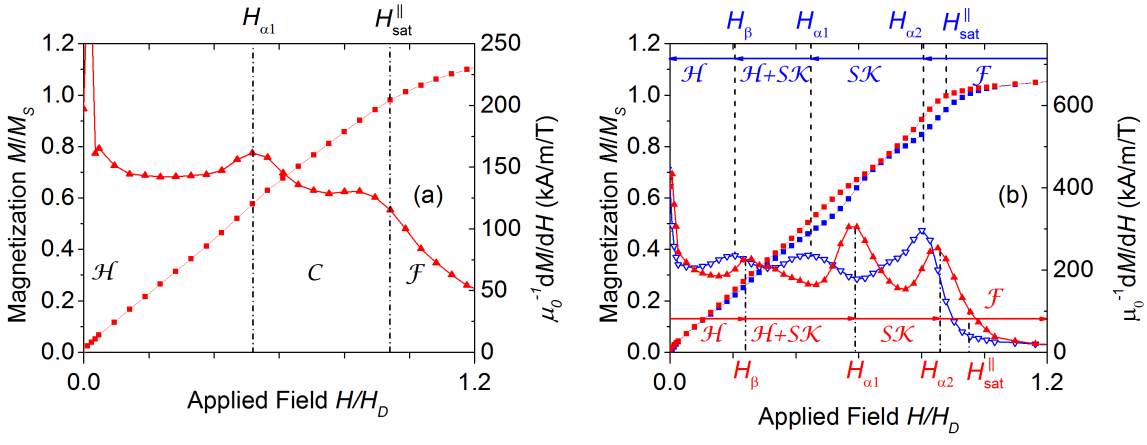

Figure 3.7: Measured magnetization (squares) and susceptibility (triangles) for (a) $T = 42$ K, and (b) $T = 15$ K. In (b) red closed symbols show values measured on increasing field and open blue symbols show values measured for decreasing field. $\mathcal{H}$ denotes helicoid phase, $\mathcal{SK}$ denotes skyrmion phase, $\mathcal{C}$ denotes conical phase, and $\mathcal{F}$ denotes ferromagnetic phase.

Figure 3.6 shows calculated magnetization profiles for $K_u/K_0 = 0.22$ and $K_u/K_0 = 0.02$ (inset), corresponding to $T = 15$ K and $T = 42$ K respectively. These two graphs show distinctly different behaviors, that correspond to two different regions of the anisotropy-field phase diagram. Figure 3.6 (inset), which is qualitatively comparable to the measured curve at 42K shown in Fig. 3.7 (a), has a single first-order transition from the helical to conical phase at low field that represents the reorientation of $\vec{Q}$ from the [111] direction to the field direction. This corresponds to $H_{\alpha 1}$ on the measured magnetization curve in Fig. 3.7 (a). Above this transition, the measured susceptibility shows a plateau, which is consistent with the calculated conical phase that has a linear increase in magnetization with field.

The calculated magnetization curve in the larger plot of Fig. 3.6 shows two first-order transitions, the transitions into and out of the skyrmion phase. This is consistent with the presence of two first-order transitions, $H_{\alpha 1}$ and $H_{\alpha 2}$, in the measured curve shown in Fig. 3.7 (b). On the increasing branch, these two measured transition fields are $H_{\alpha 1} = 0.46$ T$= 0.56 H_D$, and $H_{\alpha 2} = 0.67$ T$= 0.86 H_D$ at $T = 15$ K. Comparison of these values with the calculated curve indicates that the system is in a metastable helicoid phase up to $H_{\alpha 1}$, as this is very close to the field $H_h/H_D = 0.62$ above which helicoids are no longer stable. The first-order nature of the transitions at $H_{\alpha 1}$ and $H_{\alpha 2}$ indicates that a skyrmion phase exists between these field values as there is no other likely phase that is topologically distinct from the helical and ferromagnetic phases. Further, the shape of the magnetization curve measured in an increasing field is consistent with the shape of the calculated magnetization for the skyrmion phase, which gives additional evidence that this is the skyrmion phase. On the decreasing branch, the lower transition, $H_{\alpha 1} = 0.45 H_D$, is much closer to the predicted transition between the helical and skyrmion phases, $H = 0.37 H_D$, shown in Fig. 3.6. This indicates that the decreasing branch follows a phase evolution much closer to the minimum energy state. The energy barrier between this minimum energy state and the metastable states that are accessed on the increasing branch is

what gives rise to the hysteresis in the measured magnetization curves.

The interpretation of the measured susceptibility curves for the temperatures below 15 K is complicated by the kinetics that become increasingly important at these temperatures. There is a much more dramatic difference between the increasing and decreasing field curves at these temperatures, as shown by Fig. 3.2. In particular, for increasing fields, $H_{\alpha 1}$ dominates, and $H_{\alpha 2}$ becomes a flat shoulder instead of a peak. This indicates behavior similar to that discussed for high temperature, where the system transitions from a helical phase to a conical phase at $H_{\alpha 1}$, and then progresses smoothly into the ferromagnetic phase. On the decreasing branch, the transition $H_{\alpha 1}$ shrinks, vanishing almost completely at the lowest temperatures, while $H_{\alpha 2}$ remains as a large peak. This indicates that there is no conical phase with decreasing field. Instead, $H_{\alpha 2}$ indicates a transition directly into the ferromagnetic phase, likely from a mixed skyrmion/helicoid phase.

Figure 3.2 also shows that in all regions of the phase diagram, apart from the highest temperatures, there is a third transition, H_{β}. This transition manifests as a peak that is significantly smaller than the $H_{\alpha 1}$ and $H_{\alpha 2}$ peaks, meaning it is unlikely to represent a transition of the entire film between different magnetic states. In addition, comparison of Fig. 3.6 to Fig 3.7 (b) shows that this transition occurs very close to the minimum skyrmion stability field near $0.2H_D$, indicated by the open circle in Fig. 3.6. This suggests that H_{β} represents the partial nucleation of skyrmions in the films. This could occur on defect sites where the energetics would be modified and may promote skyrmion formation. For example, skyrmions could nucleate on the boundaries between chiral domains, as seen by Yu et al. in thinned FeGe crystals [52]. Assuming typical domain sizes of 500 nm [62], nucleation of single skyrmions on either side of the domain walls would give a skyrmion coverage of approximately 10%, which roughly accounts for the small size of H_{β} compared to $H_{\alpha 1}$.

The susceptibility curves in Fig. 3.2 give one other piece of evidence pointing to the presence of the skyrmion phase. As shown more clearly in Fig. 3.8, the

susceptibility drops significantly between $H_{\alpha 1}$ and $H_{\alpha 2}$ compared to the susceptibility at low fields for temperatures between 15 and 35 K. This susceptibility drop is a signature for the skyrmion phase that has been seen in magnetization measurements through the A-phase of bulk MnSi [75]. Therefore, the existence of this drop for intermediate temperatures in these films strongly points towards the skyrmion phase in this region.

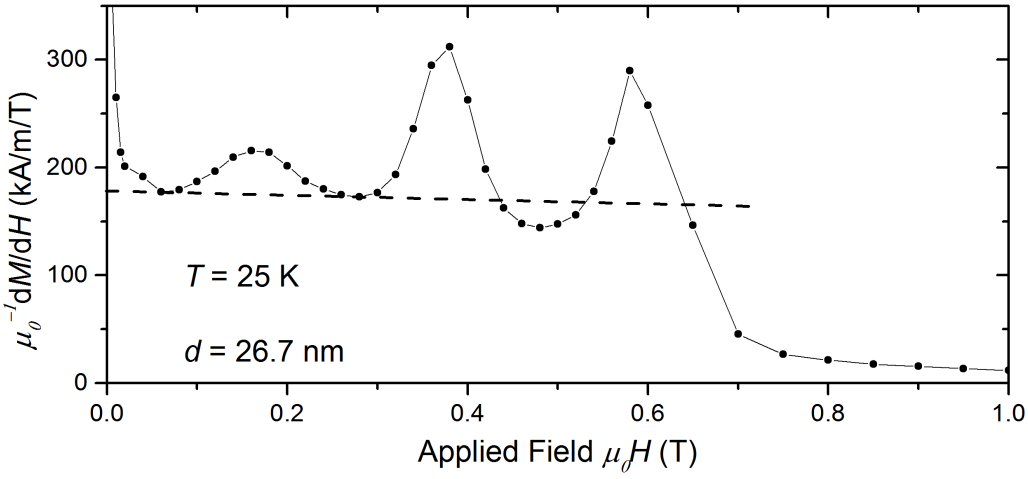

Figure 3.8: Magnetic susceptibility curve as a function of field for a $d = 26.7$ nm MnSi film at $T = 25$ K. The dashed line is a guide to the eye.

The susceptibility curves presented above are not sensitive to transitions that would lie along a vertical $H - T$ line. Therefore, I also took susceptibility measurements from field cooled $M - T$ scans in order to screen for these transitions, as described in chapter 2. From these curves, dM/dH was calculated from scans separated by $\mu_0 H = 10$ mT; the resulting curves are shown in Fig. 3.9. This data shows two first-order peaks in the susceptibility, $H_{\alpha 1}$ and $H_{\alpha 2}$, that lie between $T = 20$ K and 40 K, and are completely consistent with the susceptibility calculated from the $M - H$ curves. In addition, a clear susceptibility decrease is seen in these measurements between these transitions, which confirms the drop seen in the $M - H$ derived susceptibility curves and gives additional evidence for the skyrmion phase. Finally, no extra transitions are seen in this plot that are not present in Fig. 3.2.

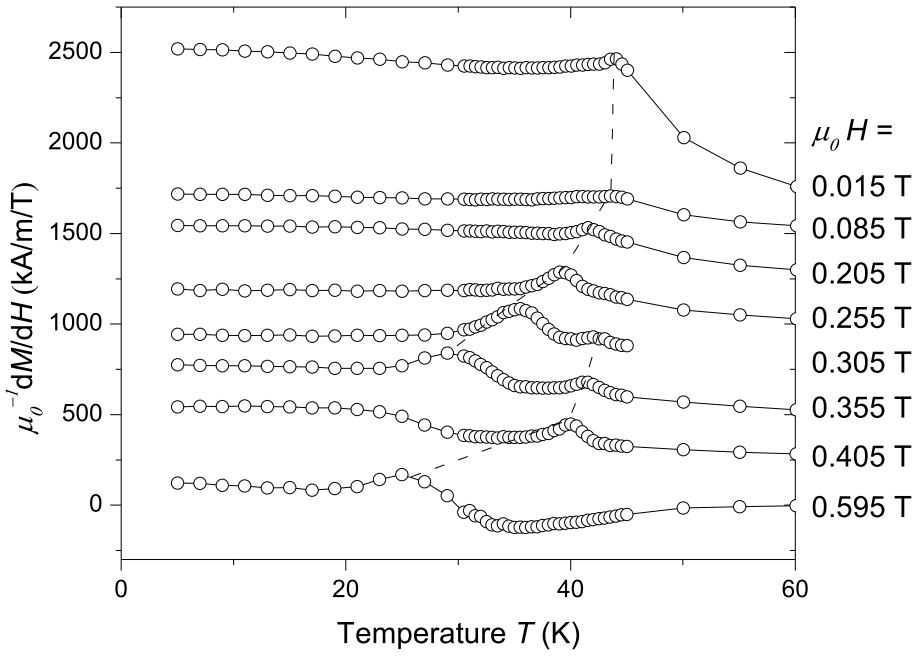

Figure 3.9: Magnetic susceptibility curves as a function of temperature for the $d = 26.7$ nm MnSi thin film. These curves were calculated from the field derivative between M-T scans separated by 0.01 T.

The transition fields from all of the susceptibility plots are summarized as a phase diagram in Fig. 3.10. This figure clearly shows the large hysteresis present at low temperatures, which emphasizes that these transitions are first-order. Further, it shows the broad skyrmion stability region that is indicated to exist in this film.

The transition fields for multiple samples are plotted together to form the anisotropy-field phase diagram shown in Fig. 3.11. On this phase diagram, the data points below $T = 15$ K were not plotted in order to avoid the more complicated behavior at these temperatures. Further, the critical fields determined from the increasing and decreasing $M - H$ branches are averaged together for each temperature in order to more easily compare with theoretical results. This makes only a small difference to the phase diagram as there is little hysteresis at $T = 15$ K and above. Figure 3.11 shows that the variation of the measured transition fields fits well to the predicted curves. H_β tracks the lower skyrmion stability line, H_{S1}, very well. This indicates that skyrmions begin to nucleate at this field in all films. The next transition, $H_{\alpha 1}$,

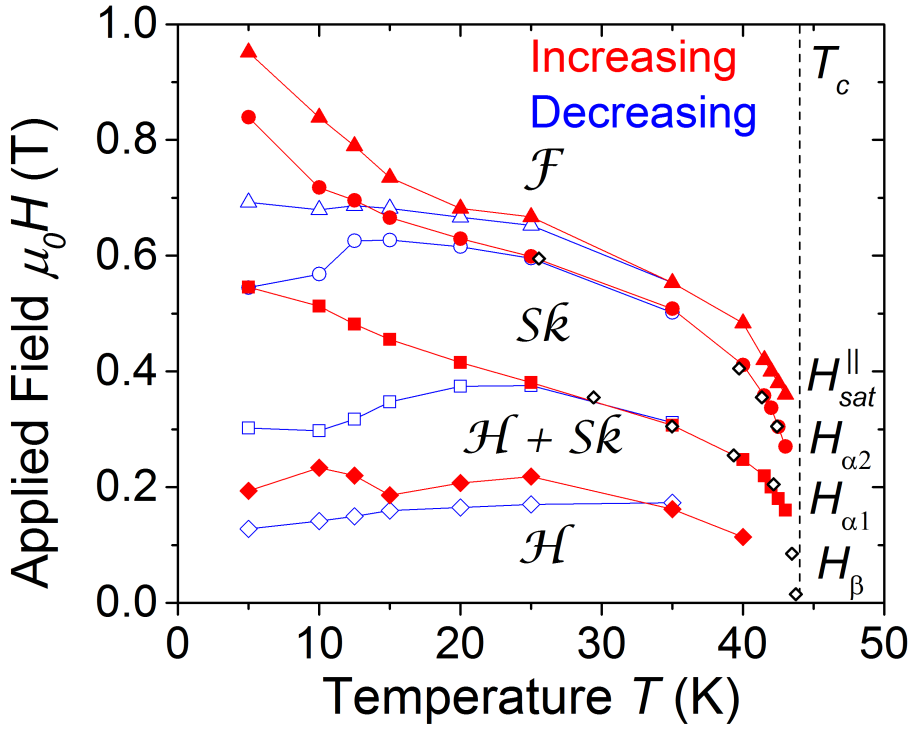

Figure 3.10: Magnetic phase diagram of the $d = 26.7$ nm MnSi thin film from magnetic susceptibility measurements. Red and blue symbols represent peaks in the susceptibility from $M - H$ curves, and the black diamonds represent peaks in the susceptibility from M-T curves.

follows a nearly horizontal line that is very close to $H_h = 0.62H_D$, the upper helicoid stability field. This gives additional evidence that $H_{\alpha 1}$ represents the field where the helicoid phase disappears completely, making way for either the conical phase at high temperatures, or the skyrmion phase at lower temperatures. The final first-order transition, $H_{\alpha 2}$, has a slope that is slightly different from that of $H_{sat}^{\parallel}$, and is consistent with the slope of H_{S3}, the upper bound of skyrmion stability. This indicates that the system does not immediately fall into the ferromagnetic phase when the skyrmion lattice dissolves, but passes through an intermediate state for a small field region. One possibility for this state is a disordered phase of isolated skyrmions, as was observed in (Fe,Co)Si [50].

It is important to note that the measured transition fields show that skyrmions are stable up to H_{S3}, whereas the theory predicts equilibrium stability of skyrmions

only in the region between H_{S1} and H_{S2}, with a cone phase existing between H_{S2} and H_{S3}. This indicates that there are additional interactions in these films, which act to either stabilize the skyrmion phase or destabilize the cone phase, and are not taken into account by the model of Eq. 1.7. These additional interactions may also explain the shift of H_{S3} to a slightly higher field than predicted, and of H_h to a slightly lower field. Future work towards understanding the nature of these interactions will be important to develop a full picture of the magnetic phases in this material.

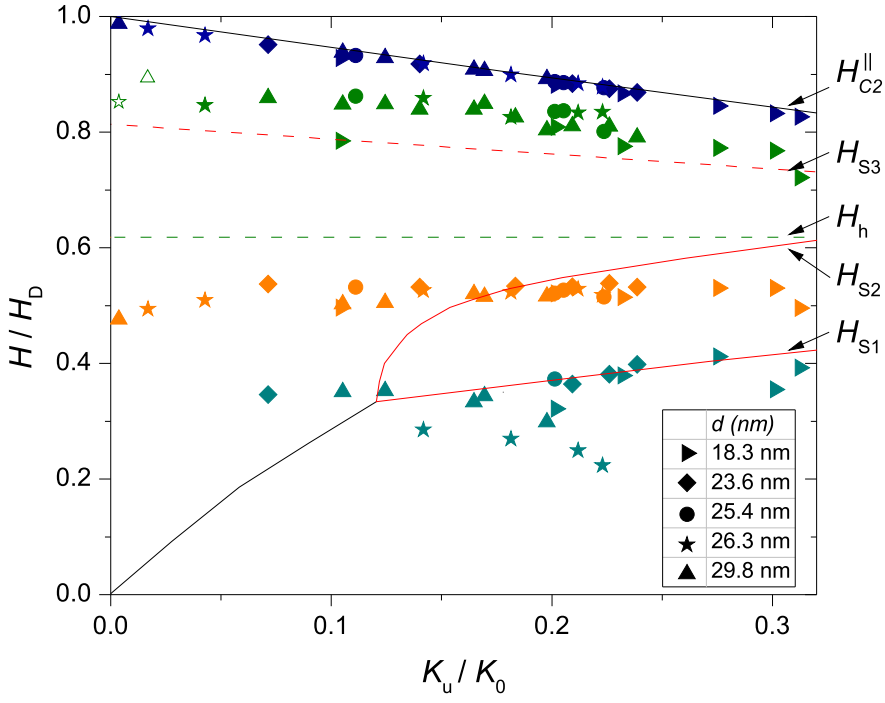

Figure 3.11: Phase diagram of MnSi thin films as a function of anisotropy. Teal symbols are transitions H_β from a variety of films, orange symbols show $H_{\alpha 1}$, green symbols show $H_{\alpha 2}$ and navy symbols show $H_{sat}^{\parallel}$. Solid and dotted lines show theoretical transition fields calculated by Bogdanov et al. H_{S1} and H_{S2} are the lower and upper bounds of skyrmion equilibrium stability, H_h is the upper bound of helicoid stability, and H_{S3} is the upper bound of skyrmion stability.

3.2 Polarized Neutron Reflectometry

As an independent verification of the magnetic states, I measured polarized neutron reflectivity curves at a number of field and temperature points for the 26.7 nm film with $H \parallel [1\bar{1}0]$. This film has previously been studied by PNR for four field values at $T = 5$ K [20]. I measured reflectivity curves for additional field values at $T = 5$ K to obtain a more complete picture of the magnetic structure. Furthermore, I measured curves at $T = 25$ K to explore a different region of the phase diagram. Figure 3.12 shows the field-temperature values of the PNR measurements, where green stars represent the curves shown in this thesis, and navy stars represent previous measurements by Karhu et al. [20]. All PNR measurements were obtained on the decreasing field branch.

I measured PNR curves at $T = 25$ K in applied fields of $B = 2$ T, 500 mT, 300 mT, and -32 mT, and at $T = 5$ K in applied fields of $B = 2$ T, 700 mT, 400 mT, 200 mT and -32 mT. Here, the negative field refers to the direction with respect to the physical instrument. However, in all cases the sign convention is adopted that a positive neutron spin is parallel to the field direction. For both temperatures the field was first set to 2 T for measurement of the 2 T reflectivity curve. The reflectivity curves at lower field, with the exception of $B = -32$ mT, were then measured by sequentially decreasing the field from 2 T through the required field values. The $B = 32$ mT reflectivity curves could not be measured by directly decreasing the field to 32 mT as instrumental hysteresis requires that low field values be approached from negative field in order to have an acceptable spin-flip ratio. Therefore, for the $B = 32$ mT curves the field was first set to -2 T, and then increased up to -32 mT where the reflectivity curve was measured. $B = -32$ mT was used rather than 32 mT in order to stay on the decreasing field branch of the hysteresis loop.

Simulreflec was used to calculate fits to the data from given magnetization depth profiles by using the structural model of this film found previously by Karhu in ref.

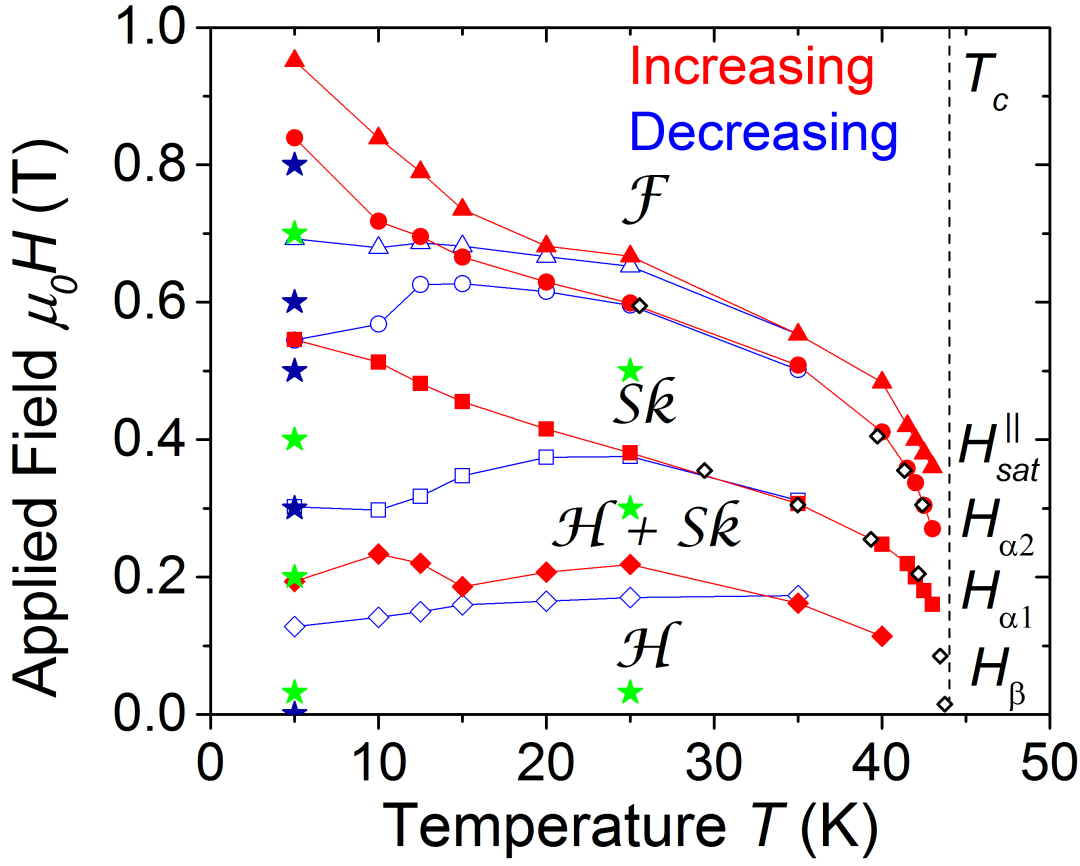

Figure 3.12: Magnetic phase diagram of the $d = 26.7$ nm MnSi thin film from magnetic susceptibility measurements. Red and blue symbols represent peaks in the susceptibility from $M - H$ curves, and the black diamonds represent peaks in the susceptibility from $M - T$ curves. Stars show field-temperature data points at which polarized neutron reflectivity curves were measured. Navy stars were measured previously by Karhu et al. in Ref. [20] and green stars are presented in this thesis.

[62]. This structural model was generated by simultaneously fitting x-ray reflectometry data and unpolarized neutron reflectometry data and is summarized in Table 3.1. To input the magnetization profiles into Simulreflec, the profiles were discretized into 100 layers each of thickness $d = 0.263$ nm. These layers replaced the $d = 26.3$ nm MnSi layer shown in Table 3.1. The fits generated by Simulreflec were then corrected for the measured spin-flip ratios, shown in Table 3.2, using Eq. 2.11.

Figures 3.13 - 3.16 present the field dependence of the PNR data at $T = 25$ K. The $B = 2$ T reflectivity data in Fig. 3.13 is well fit by a flat magnetization profile, with

Layers	Thickness d (nm)	Density ρ (10^{28} atoms / m^3)	Roughness σ (nm)
Si Substrate	0	5.00	0.47
MnSi	26.3	8.44	0.76
MnSi + Si	0.38	7.04	0.27
Si	20.31	5.00	0.68
SiO_2	1.56	1.76	0.55
Vacuum	0	0	0

Table 3.1: Structural model of the 26.7 nm MnSi thin film used to fit the neutron data.

Field (T)	Spin-flip Ratio
2	35
0.5	20
0.3	29
0.032	36

Field (T)	Spin-flip Ratio
2	30
0.7	18.7
0.4	35.4
0.2	19.5
0.032	29.9

Table 3.2: Spin-flip ratios for PNR measurements at 25 K (left) and 5 K (right).

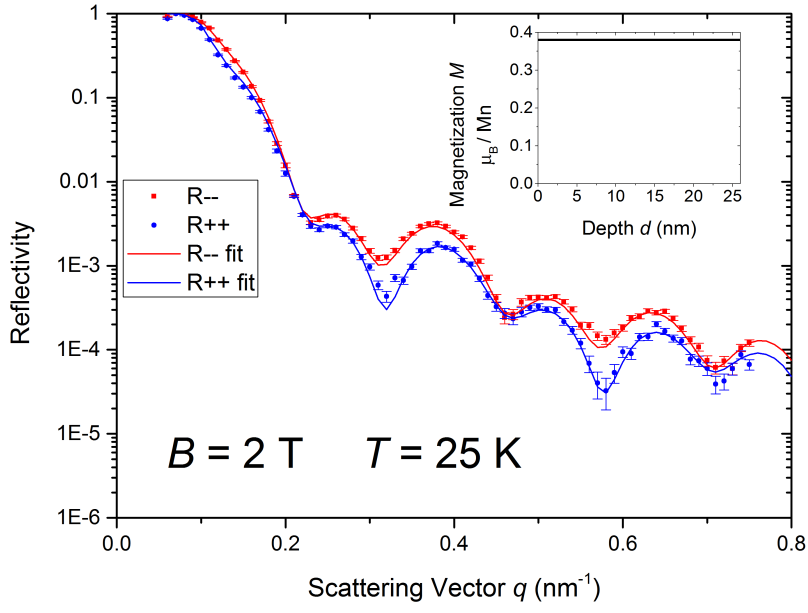

Figure 3.13: Polarized neutron reflectometry data for the $d = 26.7$ nm MnSi film measured at $B = 2$ T, $T = 25$ K. Blue(red) circles show the spin-up(down) measured reflectivity points with 1σ error bars. Solid blue(red) lines show the reflectivity fits calculated using Simulreflec. The inset shows the magnetization profile used to fit the data.

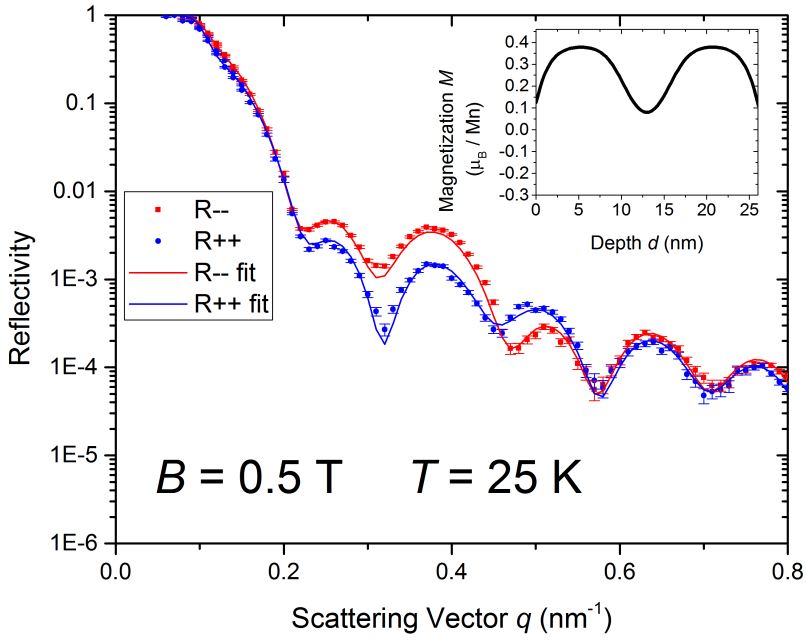

Figure 3.14: Polarized neutron reflectometry data for the $d = 26.7$ nm MnSi film measured at $B = 500$ mT, $T = 25$ K. Blue(red) circles show the spin-up(down) measured reflectivity points with 1σ error bars. Solid blue(red) lines show the reflectivity fits calculated using Simulreflec. The inset shows the magnetization profile used to fit the data.

$M = 0.38\mu_B$ / Mn. This shows that a ferromagnetic phase exists above the saturation field, as is expected. When the field is decreased to 500 mT, midway between $H_{\alpha 1}$ and $H_{\alpha 2}$, the data shown in Fig. 3.14 is very well fit by the magnetization profile for the skyrmion phase calculated theoretically by Rybakov [88]. The structure of the skyrmion phase was calculated by energy minimization assuming free boundary conditionsfor the interface, in contrast to the periodic boundary conditions used to generate Fig. 3.6 and 3.11. The magnetization profile, expressed in terms of the saturation magnetization (M_S), was calculated by integrating the magnetization over the film area at each depth in the film. To input this into Simulreflec, the saturation magnetization was taken to be $M_S = 0.38\mu_B$ / Mn, the value obtained from the reflectivity data at $B = 2$ T. It is important to note that the magnetization profile so obtained was directly used to fit the reflectivity data, with no fitting parameters other than the measured M_S. This gives strong evidence that the skyrmion phase

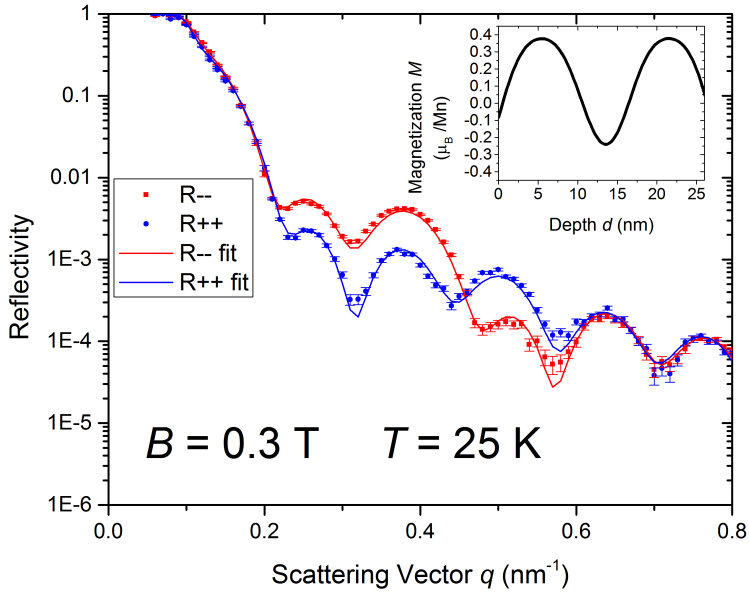

Figure 3.15: Polarized neutron reflectometry data for the $d = 26.7$ nm MnSi film measured at $B = 300$ mT, $T = 25$ K. Blue(red) circles show the spin-up(down) measured reflectivity points with 1σ error bars. Solid blue(red) lines show the reflectivity fits calculated using Simulreflec. The inset shows the magnetization profile used to fit the data.

exists at this field, as was expected from magnetometry data.

As the field is dropped below $H_{\alpha 1}$ to 300 mT, the reflectivity data, shown in Fig. 3.15, changes significantly, and is no longer well fit by the pure skyrmion phase. As discussed in section 3.1, the magnetometry data indicates that a mixed helicoid-skyrmion phase exists between H_β and $H_{\alpha 1}$, the region where this data is measured. Hence, the reflectivity data was fit with a profile generated from the superposition of a distorted helicoid and the skyrmion phase. This profile was calculated from the following equation,

$$M = \left[M_1 sin\left(\frac{2\pi y}{\lambda} + \phi_0\right) + M_2 cos^2\left(\left[\frac{2\pi y}{\lambda} + \phi_0\right]\right)\right](1 - S_f) + S_f M_S S(y), \quad (3.1)$$

where M_1 and M_2 are fitting parameters giving the proportions of first harmonic and a phenomenological non-linear term of the helicoid, y is the depth in the film, λ is the helical wavelength, ϕ_0 is a fitting parameter which gives the translation of

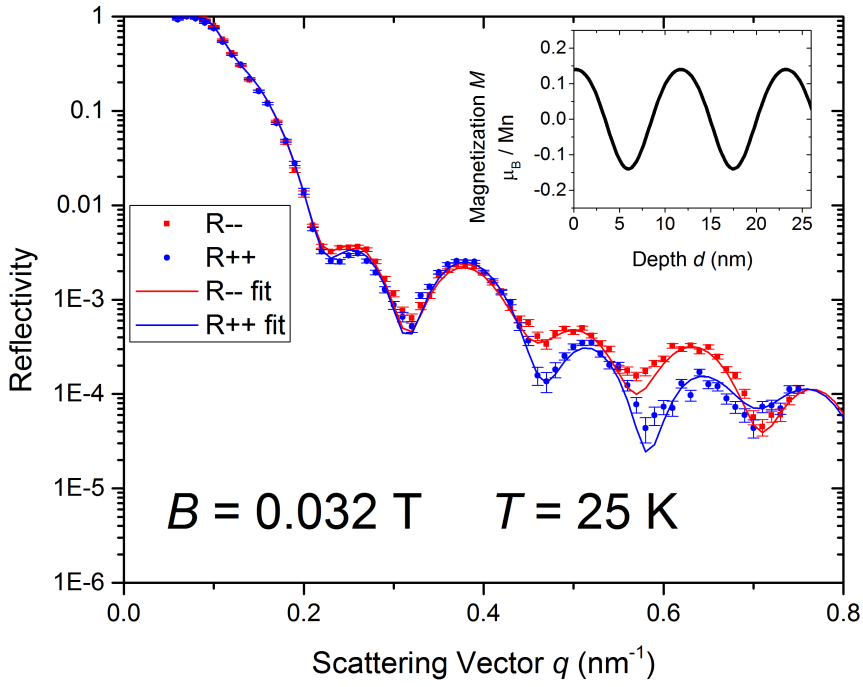

Figure 3.16: Polarized neutron reflectometry data for the $d = 26.7$ nm MnSi film measured at $B = 32$ mT, $T = 25$ K. Blue(red) circles show the spin-up(down) measured reflectivity points with 1σ error bars. Solid blue(red) lines show the reflectivity fits calculated using Simulreflec. The inset shows the magnetization profile used to fit the data.

the helicoid along the [111] direction, S_f is the fraction of skyrmion phase, and $S(y)$ is the skyrmion magnetization depth profile. The fit profile was generated using the parameters $M_1 = 0.38\mu_B/Mn$, $M_2 = 0.11\mu_B/Mn$, $\phi_0 = 0.66$, $A = 0.4$ and $\lambda = 16$ nm. This gives a 40% skyrmion phase in the film, and a significant non-linearity in the helicoid phase. Presence of non-linearity in the helicoid is expected, as it has been explained theoretically in helicoids with an applied field $\vec{H} \perp \vec{Q}$ by Plumer and Walker [89], and observed by small angle neutron scattering in bulk FeGe [90] and MnSi [91] as well as in prior PNR studies of MnSi thin films [20]. The 40% skyrmion phase is significantly larger than the expected skyrmion fraction of 10% from nucleation at chiral domain boundaries. This proportion of a skyrmion phase, assuming nucleation only around the chiral grain boundaries, would require a skyrmion lattice around each boundary that is eight skyrmions deep. Lorentz images collected by Yu et al.

only show skyrmions up to three deep at the grain boundaries in FeGe, and it is not known whether the energy balance in MnSi thin films would promote more skyrmion formation at these sites. If this is not the case, it is possible that skyrmions are nucleating at other defect sites to give this 40% skyrmion fraction.

The final reflectivity curve, at $B = -32$ mT, is measured below the field, H_β, where magnetometry indicates skyrmions begin to nucleate, and hence no skyrmion phase is expected. This curve was fit using a profile generated from Eq. 3.2 with parameters $M_1 = 0.14\mu_B/Mn$, $M_2 = 0.024\mu_B/Mn$, $\phi_0 = 1.7$, and $\lambda = 11.5$ nm. This profile has no skyrmion phase, as expected, and there is a small non-linearity in the helicoid phase. Adding this non-linearity only makes a small difference to the reflectivity curve, and the data cannot distinguish between these two cases from the reflectivity alone, as shown in Fig. 3.17. However, the non-linearity brings the average film magnetization to 9.2 kA/m from 4.6 kA/m without the non-linearity, which agrees much better to the value of 9.2 kA/m obtained from SQUID magnetometry data. Table 3.3 shows the comparisons of average magnetization from the PNR fits and SQUID data for the four PNR curves. In each case, the magnetizations agree within 5%, which is an important validity test for the PNR fits. This table also shows a summary of the fitting parameters used to generate the magnetization depth profiles.

B (T)	PNR M (kA/m)	SQUID M (kA/m)	M_1 (μ_B/Mn)	M_2 (μ_B/Mn)	ϕ_0	S_f	λ (nm)
2	148	157	N/A	N/A	N/A	N/A	N/A
0.5	109	104	N/A	N/A	N/A	1	N/A
0.3	63.0	61.3	0.38	0.11	0.66	0.4	16
0.032	9.2	9.2	0.14	0.024	1.7	0	11.5

Table 3.3: Average magnetization for PNR measurements at $T = 25$ K compared to magnetization measured by SQUID, and fitting parameters used to generate the magnetization depth profiles.

Taken together, these PNR curves at 25 K support the magnetic phase diagram generated from the SQUID magnetometry data, with a helicoid phase at low field,

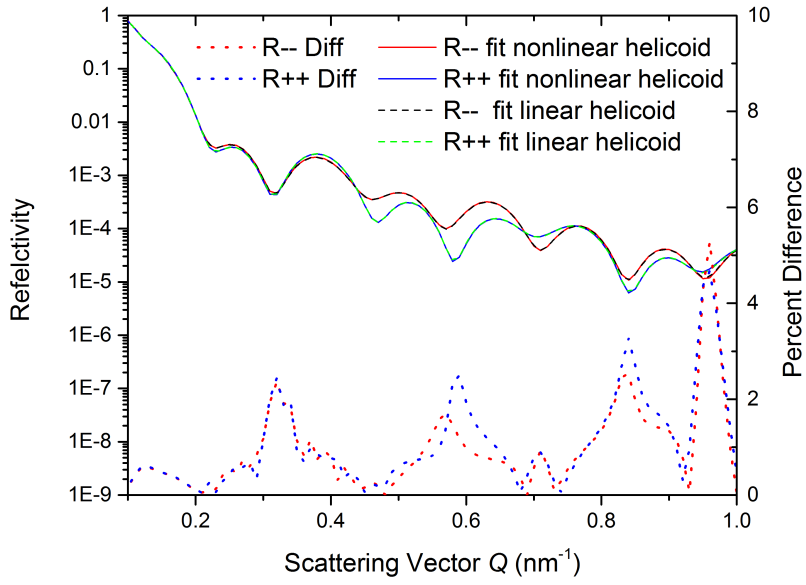

Figure 3.17: Comparison of PNR fits for $B = 32$ mT at $T = 25$ K with and without a non-linearity added. Red and blue solid lines show the spin-down and spin-up reflectivities calculated with a non-linearity, while the dashed black and dashed green lines show reflectivities calculated without the non-linearity. Dotted red(spin-down) and blue(spin-up) lines show the percent difference between the curves with and without the non-linearity.

partial nucleation of skyrmions at H_β, formation of a skyrmion lattice at $H_{\alpha 1}$, and dissolution of the skyrmion lattice at $H_{\alpha 2}$.

Figures 3.18-3.22 present the field dependence of the PNR data at $T = 5$ K. As expected, the $B = 2$ T reflectivity curve shown in Fig. 3.18 is again well fit with a uniform magnetization profile, with $M = 0.42\mu_B/Mn$. This magnetization is higher than for the $T = 25$ K point at 2 T, which is expected from the magnetometry curves.

$B = 700$ mT brings the film below $H_{sat}^{\parallel}$, and the reflectivity curve, shown in Fig. 3.19, can not be fit with a uniform magnetization profile, indicating that at this field the system is in neither a ferromagnetic nor conical phase with $\vec{Q} \parallel \vec{B}$. Instead, I was able to obtain a reasonable fit to the data with a magnetization profile that is flat in the center of the film and tails off slightly at both interfaces. One possible explanation for this magnetization depth profile is a long wavelength distorted helicoid

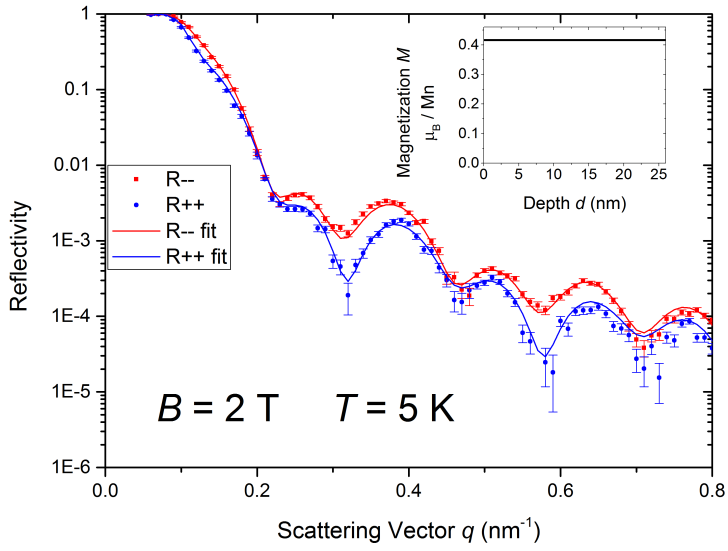

Figure 3.18: Polarized neutron reflectometry data for the $d = 26.7$ nm MnSi film measured at $B = 2$ T, $T = 5$ K. Blue(red) circles show the spin-up(down) measured reflectivity points with 1σ error bars. Solid blue(red) lines show the reflectivity fits calculated using Simulreflec. The inset shows the magnetization profile used to fit the data.

with $\vec{Q} \parallel [111]$.

The $B = 400$, 200, and 32 mT reflectivity curves shown in Fig. 3.20 - 3.22 are each fit with distorted helicoid magnetization profiles generated by the equation,

$$M = \left[M_1 sin\left(\frac{2\pi y}{\lambda} + \phi_0\right) + M_2 cos^2\left(\frac{2\pi y}{\lambda} + \phi_0\right)\right] + G, \tag{3.2}$$

where G is a fitting parameter which gives an offset to the helicoids magnetization. This offset gives a magnetization that is larger in the direction of the field then away from it, and indicates that the films are not in a pure helicoid phase. In particular, a small offset is consistent with the presence of a mixed skyrmion-helicoid phase. The offset was used for fitting at $T = 5$ K rather than using a fraction of a skyrmion depth profile, as was done for fitting at $T = 25$ K, because detailed calculations of the skyrmion structure at this temperature are not available. The fitting parameters used for the three field values are shown below in Table 3.4.

These fits indicate that the magnetic states at $B = 400$ mT and 200 mT are nearly

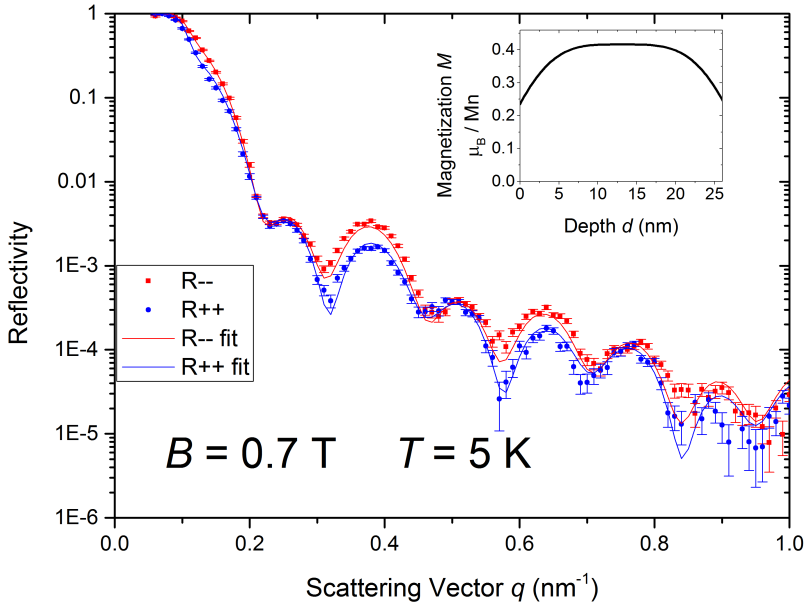

Figure 3.19: Polarized neutron reflectometry data for the $d = 26.7$ nm MnSi film measured at $B = 700$ mT, $T = 5$ K. Blue(red) circles show the spin-up(down) measured reflectivity points with 1σ error bars. Solid blue(red) lines show the reflectivity fits calculated using Simulreflec. The inset shows the magnetization profile used to fit the data.

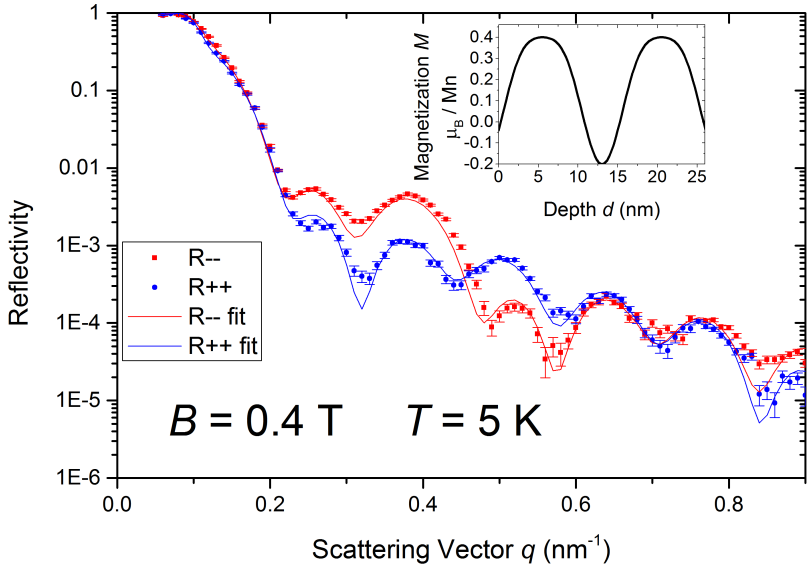

Figure 3.20: Polarized neutron reflectometry data for the $d = 26.7$ nm MnSi film measured at $B = 400$ mT, $T = 5$ K. Blue(red) circles show the spin-up(down) measured reflectivity points with 1σ error bars. Solid blue(red) lines show the reflectivity fits calculated using Simulreflec. The inset shows the magnetization profile used to fit the data.

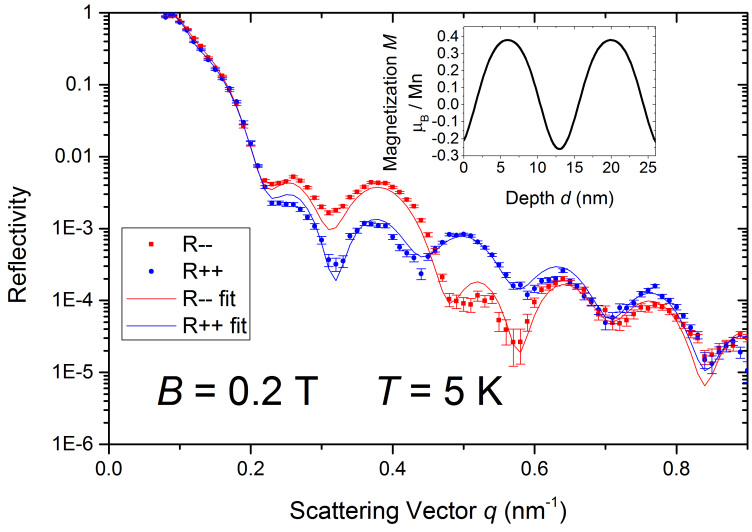

Figure 3.21: Polarized neutron reflectometry data for the $d = 26.7$ nm MnSi film measured at $B = 200$ mT, $T = 5$ K. Blue(red) circles show the spin-up(down) measured reflectivity points with 1σ error bars. Solid blue(red) lines show the reflectivity fits calculated using Simulreflec. The inset shows the magnetization profile used to fit the data.

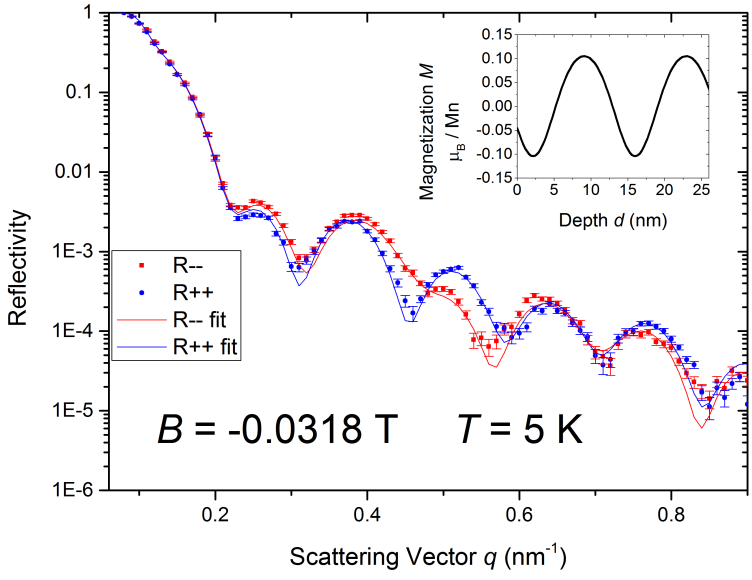

Figure 3.22: Polarized neutron reflectometry data for the $d = 26.7$ nm MnSi film measured at $B = 32$ mT, $T = 5$ K. Blue(red) circles show the spin-up(down) measured reflectivity points with 1σ error bars. Solid blue(red) lines show the reflectivity fits calculated using Simulreflec. The inset shows the magnetization profile used to fit the data.

Field B (T)	M_1 (μ_B/ Mn)	M_2 (μ_B/ Mn)	ϕ_0	G (μ_B/ Mn)	λ (nm)
0.4	0.3	0.12	0.75	0.1	15
0.2	0.32	0.08	1.1	0.06	14
0.032	0.21	0.02	2.54	0	13.85

Table 3.4: Fitting parameters used to generate the magnetization depth profiles to fit PNR curves at $T = 5$ K, $B = 400$, 200, and 32 mT.

identical, with only small changes in the parameters. The presence of a non-zero offset at both of these fields supports the interpretation of H_β on the decreasing branch at $T = 5$ K as the field where there is partial nucleation of skyrmions. In addition, the slightly larger offset at $B = 400$ mT may indicate that there is additional skyrmion nucleation at $H_{\alpha 1}$ at this temperature, although it is difficult to distinguish this small change in offset from the reflectivity curves. Further, the non-linearity in the helicoid is slightly larger at $B = 400$ mT than at $B = 200$ mT, which indicates an increasing distortion of the helicoid from H_β to $H_{\alpha 2}$.

The reflectivity curve at $B = 32$ mT, below H_β, is fit by a magnetization profile that has no offset, which is consistent with the interpretation of H_β as the field where skyrmions begin to nucleate. However, the magnetization profile at this field is generated with a translation parameter, ϕ_0, that is significantly larger than at other fields. The position of the helicoid in this magnetization profile is similar to that used by Karhu et al. to fit the reflectivity at $B = 1$ mT. This indicates that the translation of the helicoid does not occur gradually from $B = 0$ mT up to $B = 200$ mT, but rather might occur in an abrupt jump at H_β. If there are skyrmions nucleated at H_β, the interaction between the partial skyrmion phase and helicoid phase may energetically favor this abrupt translation. In addition, surface anisotropies could be pinning the helicoid in a specific position at low fields, which could give rise to the observed shift. Further theoretical investigations of this energy balance are required to determine the nature of these effects.

The average magnetization values for the $T = 5$ K PNR profiles are compared to

Field (T)	PNR Magnetization (kA/m)	SQUID Magnetization (kA/m)
2	164	159
0.7	147	147
0.4	79.5	78.4
0.2	47.7	45.7
0.032	8.4	8.0

Table 3.5: Average magnetization for PNR measurements at $T = 5$ K compared to magnetization measured by SQUID.

the values from SQUID magnetometry in Table 3.5. As was seen for the $T = 25$ K profiles, these values agree within 5%, which shows that the the fits are consistent with the magnetometry measurements. Magnetization profiles determined for the $T = 5$ K PNR curves shown in this thesis are consistent with those presented earlier by Karhu et al. [20]. In particular, the curves measured at 300 mT and 500 mT by Karhu et al. are similar to the 200 mT and 400 mT curves presented here. These 4 data points give clear evidence that the magnetic state does not undergo significant changes in the region between H_β and $H_{\alpha 2}$, as was expected from the magnetization data. Further, comparison of the profile determined at 32 mT here with the 1 mT profile by Karhu et al. shows that the only difference is a small non-linearity in the helicoid at 32 mT compared to none at 1 mT. This indicates that the magnetization increase seen below H_β can be attributed entirely to a continuous increase in the distortion of the helicoid.

The PNR data presented here is completely consistent with the picture of the magnetic evolution derived from the magnetometry measurements. These two independent measures of the magnetic states of this film give compelling evidence that the skyrmion phase exists in this material with an in-plane applied field. Further, the dependence of the skyrmion stability on the film anisotropy demonstrates a mechanism by which the stability region may be manipulated, as the anisotropy can be adjusted by changing the film thickness. This study therefore represents an important step towards the use of the skyrmion phase in technological applications.

Chapter 4

Magnetic Properties with $\vec{H} \parallel [111]$

The results of the previous chapter were obtained with an applied field pointing in-plane, parallel to the $[1\bar{1}0]$ MnSi crystal axis. However, as a result of the uniaxial anisotropy with hard axis along the [111] direction, the magnetic properties are substantially different when the field is applied out-of-plane, parallel to the [111] axis. With an applied field in-plane, the hard axis of the anisotropy supresses the conical phase. This, combined with the reduction of the Dzaloshinskii-Moriya contribution to the free energy from a two dimensional modulation rather than one, leads to the stability of skyrmions in this geometry [61]. However, with an applied field along the hard axis, the magnetization of the cone phase rotates perpendicular to the hard axis, and therefore this phase is not supressed. In addition, the hard axis would destabilize a skyrmions core, which would point along the hard axis. These two effects mean that skyrmions are not predicted to be stable with an applied field along the [111] axis.

Further, as the $\vec{Q}$ vector lies along the [111] axis at zero field, a field applied along this direction does not reorient the $\vec{Q}$ vector, and hence the system can evolve continuously from a pure helicoid state into the conical state, without reorientation effects. The analysis of magnetometry and transport measurements I show below demonstrates that there is no skyrmion phase with this field arrangement.

4.1 SQUID Magnetometry and Magnetoresistance

To interrogate the phase diagram for an out-of-plane field, I measured magnetization curves as a function of field and temperature by SQUID magnetometry for a 25.4 nm

MnSi thin film with the applied field $\vec{H} \parallel [111]$. Figure 4.1 shows a full hysteresis loop measured at $T = 25$ K with this field arrangement. This figure demonstrates that there is no hysteresis in these magnetization curves. Hence, all magnetization curves after this are taken on only a single branch, where consecutive measurements alternate between increasing and decreasing branches. A series of these magnetization curves is shown in Fig. 4.2.

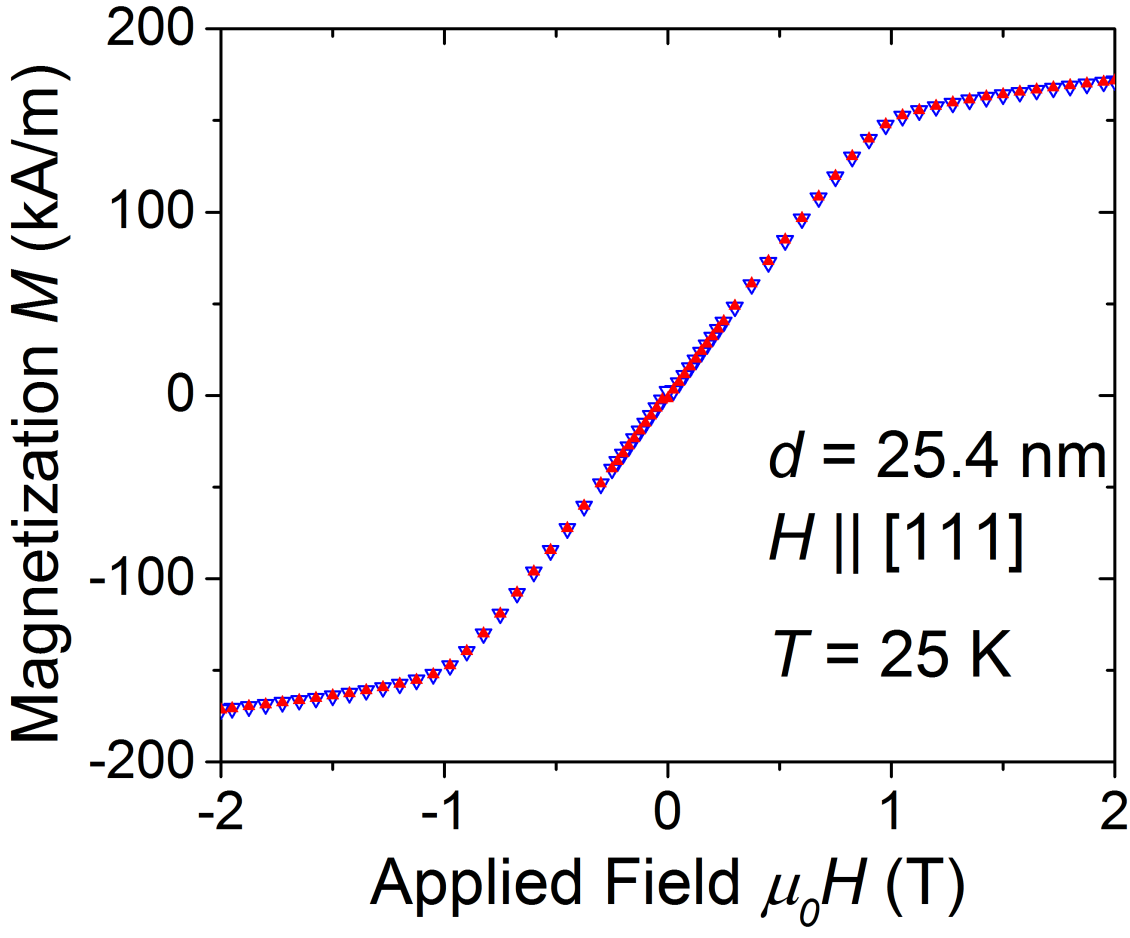

Figure 4.1: Hysteresis loop at $T = 25$ K with $H \parallel [111]$ for a $d = 25.4$ nm MnSi thin film. Blue open triangles show decreasing field points and red closed triangles show increasing field points.

Typically, the background from the substrate in thin film SQUID magnetometry is removed by assuming that the high-field susceptibility is derived entirely from the diamagnetic response of the substrate. However, MnSi is a weak itinerant magnet

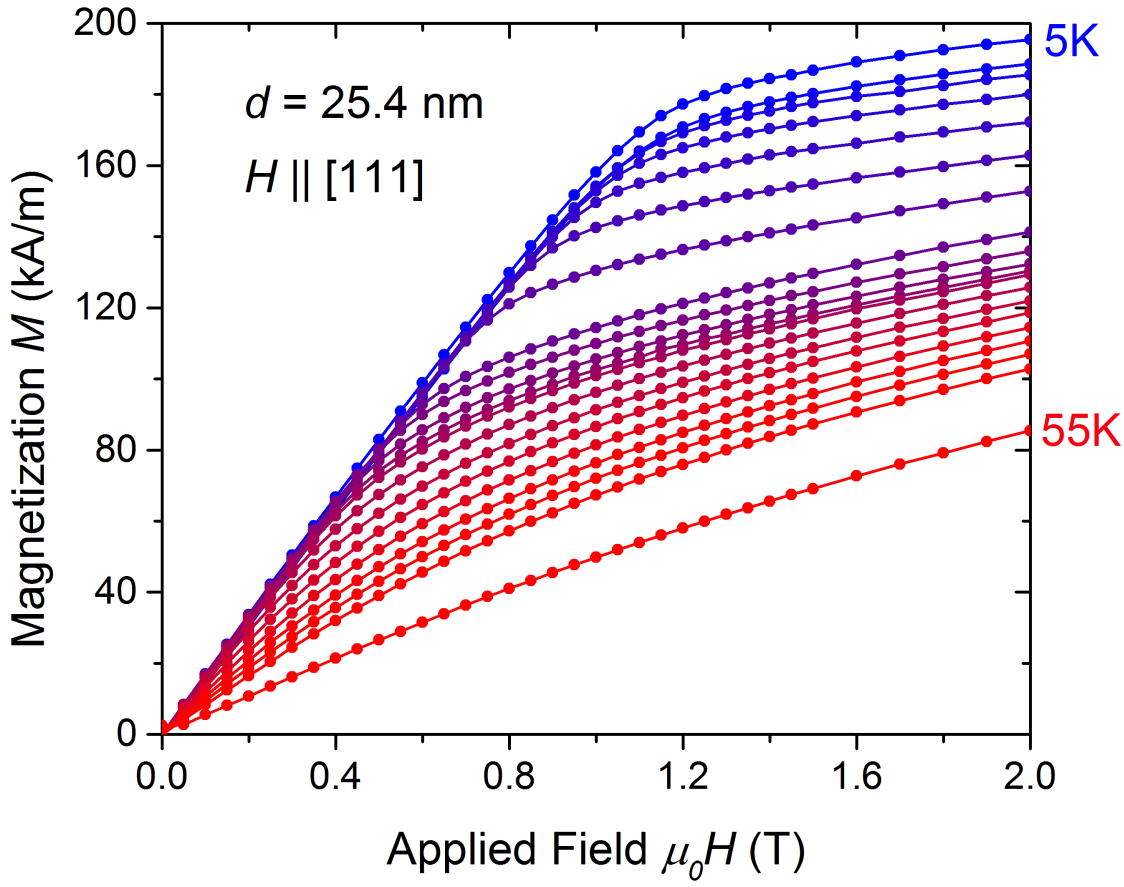

Figure 4.2: Magnetization versus applied field curves for the $d = 25.4$ nm MnSi film. Temperatures shown are 5 - 40 K in 5 K steps, 41 - 50 K in 1 K steps, 42.5 K and 55 K. The applied field points out of the plane of the film, along $H \parallel [111]$.

and has a non-zero susceptibility even up to very high fields, which therefore must be accounted for to subtract the substrate background properly [94]. In particular, it is important to correctly determine this susceptibility for fitting the Hall effect data that is presented in a later section.

Arrott plot analysis is normally used to determine the Curie temperature of a sample. Here it was instead used to determine the high-field susceptibility that corresponds to the Curie temperature, $T_C = 42 \pm 0.5$ K, independently determined from the resistivity data as shown in Fig. 4.3. This analysis involves plotting a series of M^2 vs. H/M isotherms near T_C. These curves are linear at high H/M, and the isotherm whose linear fit has an intercept of zero is the Curie temperature isotherm

[92]. This comes from considering the Landau expansion of the magnetic contribution to the free energy,

$$w_M = \frac{c_1 M^2}{2} + \frac{c_2 M^4}{4} + ... - \mu_0 M H, \tag{4.1}$$

where c_1 and c_2 are constants. If $c_1 > 0$, the free energy is minimized for $M = 0$ and the material is paramagnetic, while if $c_1 < 0$, the free energy is minimized for $M > 0$ and the material is ferromagnetic. The crossover between these two behaviors therefore occurs for $c_1 = 0$. This free energy is minimized with respect to the magnetization, M, by the relation $\mu_0 H = aM + bM^3$, which can then be linearized to $\mu_0 H/M = c_1 + c_2 M^2$. This yields the linear curves mentioned above, as $c_1 = 0$ at the curie temperature, where the material crosses from paramagnetic to ferromagnetic behavior.

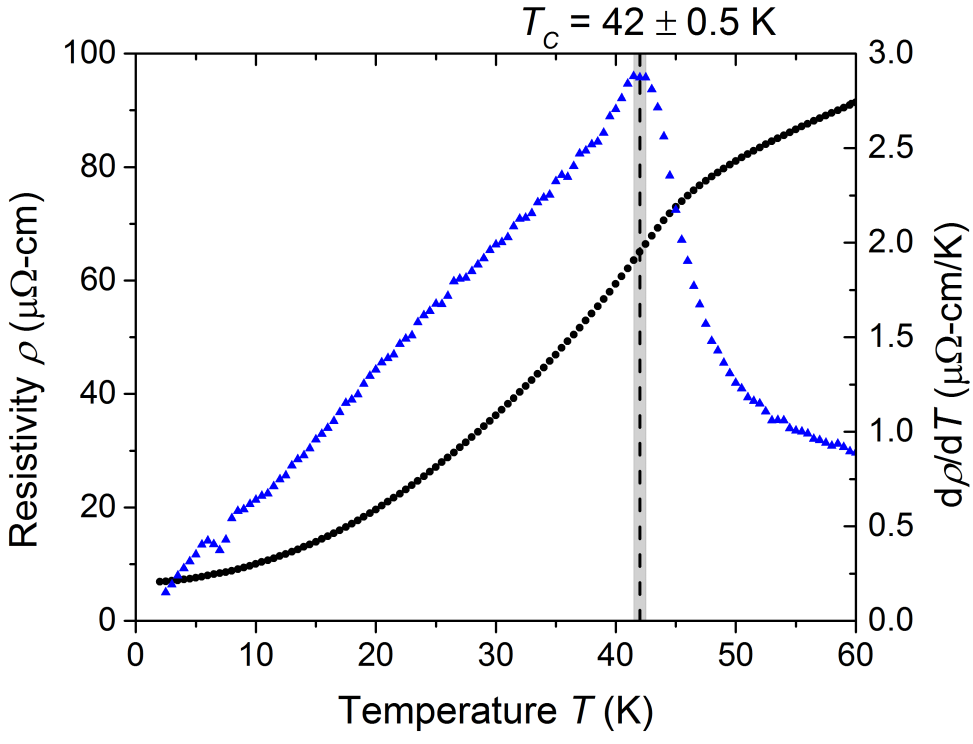

Figure 4.3: Linear resistivity (black circles) and its temperature derivative (blue triangles) measured with zero applied field on the 25.4 nm sample. The dotted line indicates the T_C, determined from the position of the peak in the derivative. The gray box around the dotted line shows the estimated uncertainty of T_C

Arrott plots of bulk MnSi are nonlinear even up to very high fields, and require a more complicated fitting to extract T_C [93]. However, I found that the Arrott plots for MnSi thin films are linear at high field and hence do not require this complex fitting.

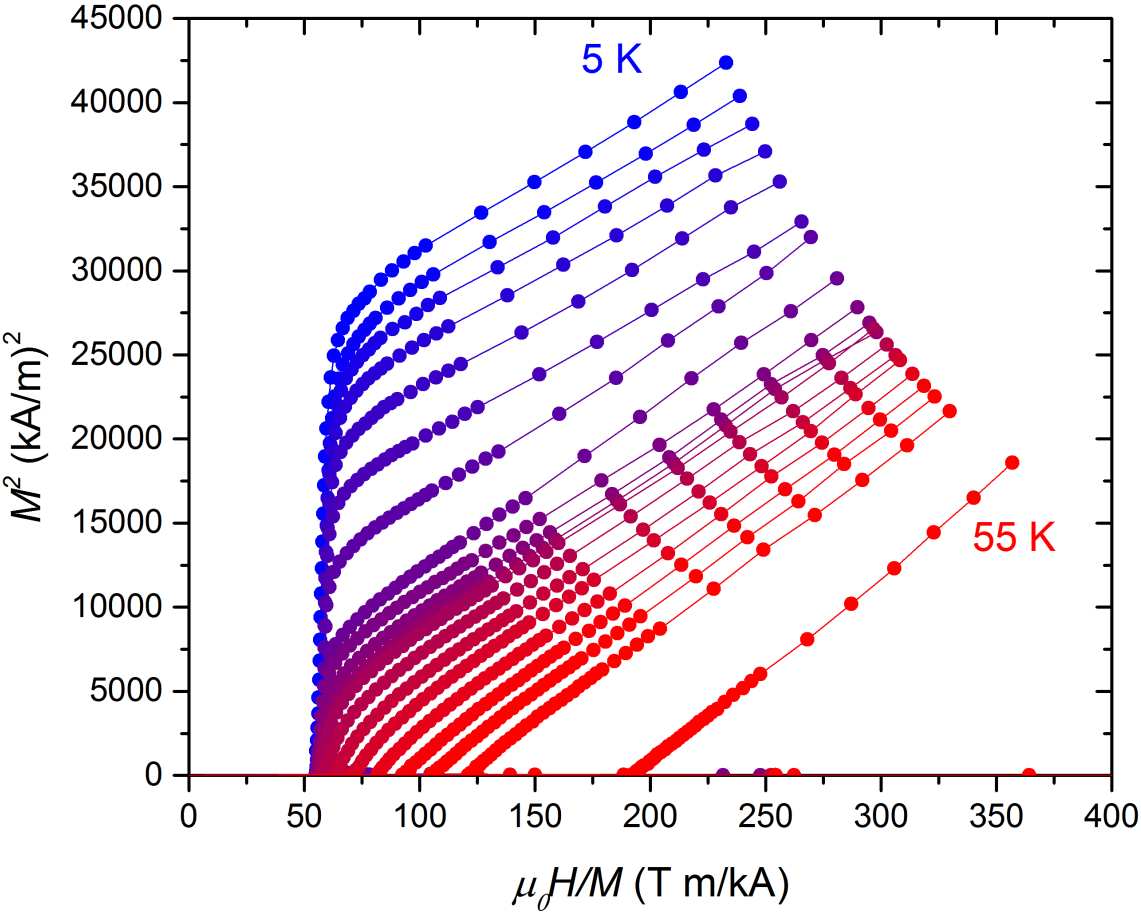

Figure 4.4: Arrott plot with applied field $H \parallel [111]$ for the 25.4 nm MnSi film. Temperatures shown are 5 - 40 K in 5 K steps, 41 - 50 K in 1 K steps, 42.5 K and 55 K.

For this analysis, the magnetization of the film is expressed as $M = (\mu - H\chi_{Si})/v$, where μ is the total moment measured by the SQUID magnetometer, χ_{Si} is an adjustable substrate background correction factor, and v is the volume of the film. An Arrott plot was then constructed using this magnetization, and the factor χ_{Si} was adjusted until the Arrott plot gave $T_C = 42 \pm 0.5$ K. The resulting Arrott plot is

shown in Fig. 4.4. The high-field susceptibility was taken as the slope of the $M - H$ graphs above 2 T, as these graphs are linear beyond this field. The value obtained at $T = 40$ K is 17.5 ± 1 kA/m/T, where the uncertainty is derived from scatter in the magnetization data and the uncertainty in T_C. This high-field susceptibilty is significantly larger than the value of 1.69 kA/m/T measured for bulk samples [94]. I also repeated this Arrott plot analysis for the $d = 26.7$ nm film discussed in the previous chapter, and found a value of 15.7 ± 0.5 kA/m. These two values are close to one another, but are roughly two standard deviations apart. Although these samples have a similar thickness, their strains are significantly different, with an out-of-plane strain of -0.45 ± 0.01 % for the 26.7 nm film and -0.38 ± 0.01 % for the 25.4 nm film [62]. This indicates that the high-field susceptibility varies from sample to sample, and may depend on the thickness or strain of the films. To properly determine this dependency, future work could study the high-field susceptibility of a range of samples of different thicknesses and strains by Arrott plot analysis.

To confirm this novel approach to SQUID substrate background subtraction, I used PNR to measure the magnetization of the $d = 26.7$ nm film at $T = 40$ K for in-plane fields of 1, 2, and 3 T. The advantage of PNR is that the magnetization of the film can be measured independently, without any contribution from the substrate. This measurement is done with an in-plane field, in contrast to the Arrott plot analysis of magnetization data with the field applied out-of-plane. However, the behavior of the ferromagnetic state is expected to be similar with an applied field in-plane or out-of-plane, and therefore this analysis should confirm the large slope found from the Arrott plots.

Measurement of the high-field magnetization with PNR was done by measuring the spin-up and spin-down reflectivities for Q between 0.08 and 0.17 nm^{-1} at each field. The spin asymmetry, $ASYM = \frac{R_{++} - R_{--}}{R_{++} + R_{--}}$, for these three curves was then calculated at each field and fit using Simulreflec to determine the magnetization of the MnSi layer. The spin asymmetry drops unexpectedly after the $Q = 0.14$ nm^{-1} data

point for the $B = 1$ T scan, likely indicating an alignment error or other transient technical fault. In order to avoid this error, the fits were done in the region Q = 0.08 to 0.14 nm^{-1}. These fits are shown in Fig. 4.5, with the fit magnetization values shown in Fig. 4.6. The slope between the $B = 2$ T and 3 T points gives a high-field susceptibility of 15 ± 2 kA/m, in reasonable agreement with the values from Arrot plot analysis, which demonstrates that MnSi thin films do have a significant high-field susceptibility.

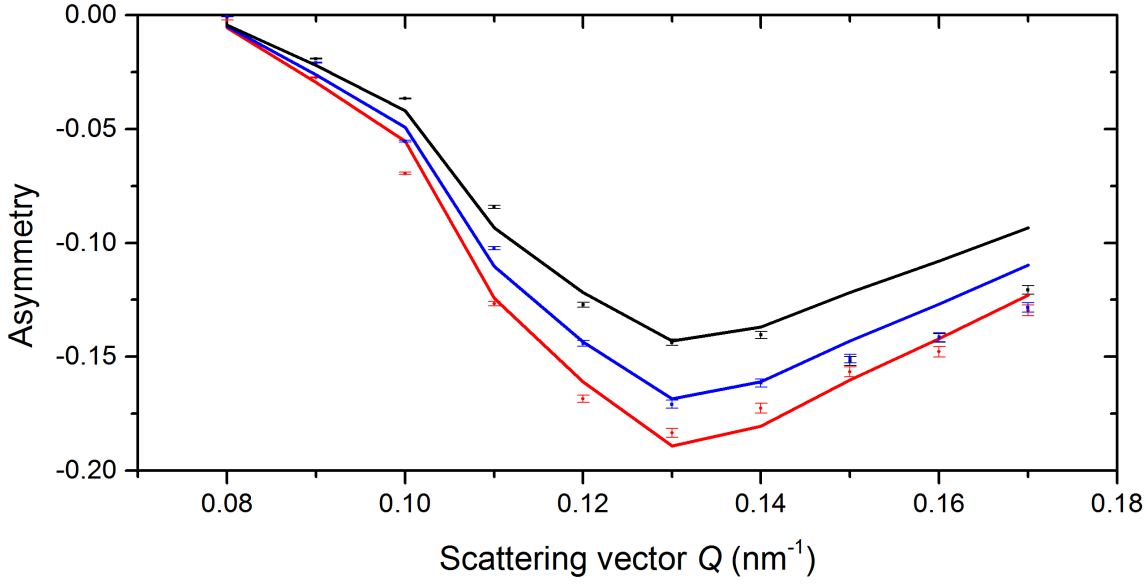

Figure 4.5: Plots of the spin asymmetry for PNR data collected at $T = 40$ K on the $d = 26.7$ nm MnSi film at $B = 1$ T (black), 2 T (blue), and 3 T (red) . Solid circles show the measured data points with 1σ error bars, and solid lines show the fits to the data generated by Simulreflec.

Figure 4.7 shows a comparison of the PNR fit magnetization values to the magnetization values measured by SQUID magnetometry on the $d = 26.7$ nm film. In this figure, the values for $H \parallel [111]$ were corrected using the substrate background correction factor determined by Arrott plot analysis. However, a suitable data set to construct an Arrott plot for $H \parallel [1\bar{1}0]$ was not available. Therefore, the substrate background was removed for this curve by adjusting the background correction factor until the slope between $B = 2$ T and 3 T matched that measured by PNR, and by

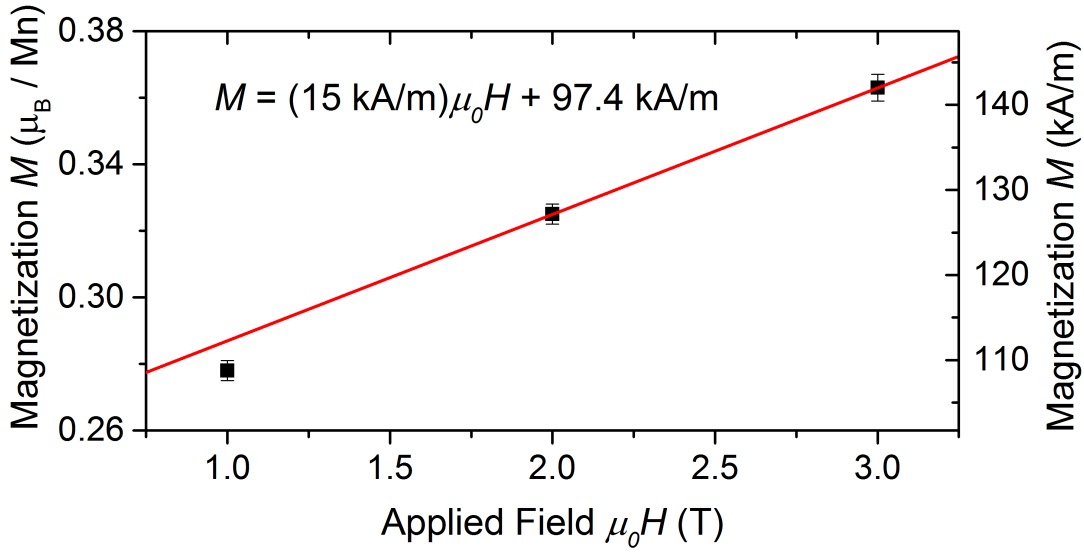

Figure 4.6: Magnetization values used to produce the spin asymmetry fits in Fig. 4.5. The red line is a linear fit to the data with the equation shown on the graph. Error bars were generated by fitting the asymmetry curves with individual 1 σ error range added to each point, and taking the difference between this fit magnetization and the data point fit magnetization.

SQUID with $H \parallel [111]$ curve. The PNR magnetizations are also plotted in this figure offset vertically by 8 kA/m to more easily compare the field dependencies. This makes it clear that the three fit magnetizations accurately match the field dependence of the magnetization measured by SQUID magnetometry with $H||[1\bar{1}0]$. In particular, this figure shows the non-linearity of the magnetization between $B = 1$ T and 2 T, which is why the high-field susceptibility must be taken between $B = 2$ T and 3 T.

This figure also shows that while the field dependencies match, the PNR fit magnetization values are offset with respect to those measured by SQUID magnetometry. One possible explanation for this offset is a temperature calibration error in the PNR measurements. As the temperature increases close to T_C, the saturation magnetization falls off rapidly, and hence a small temperature calibration error can explain the significant downward shift of the magnetization. Figure 4.8 shows the saturation magnetization as a function of field for the $d = 26.7$ nm film with $H \parallel [111]$. The values of M_S were taken as the intercepts of the high-field susceptibility fit lines for

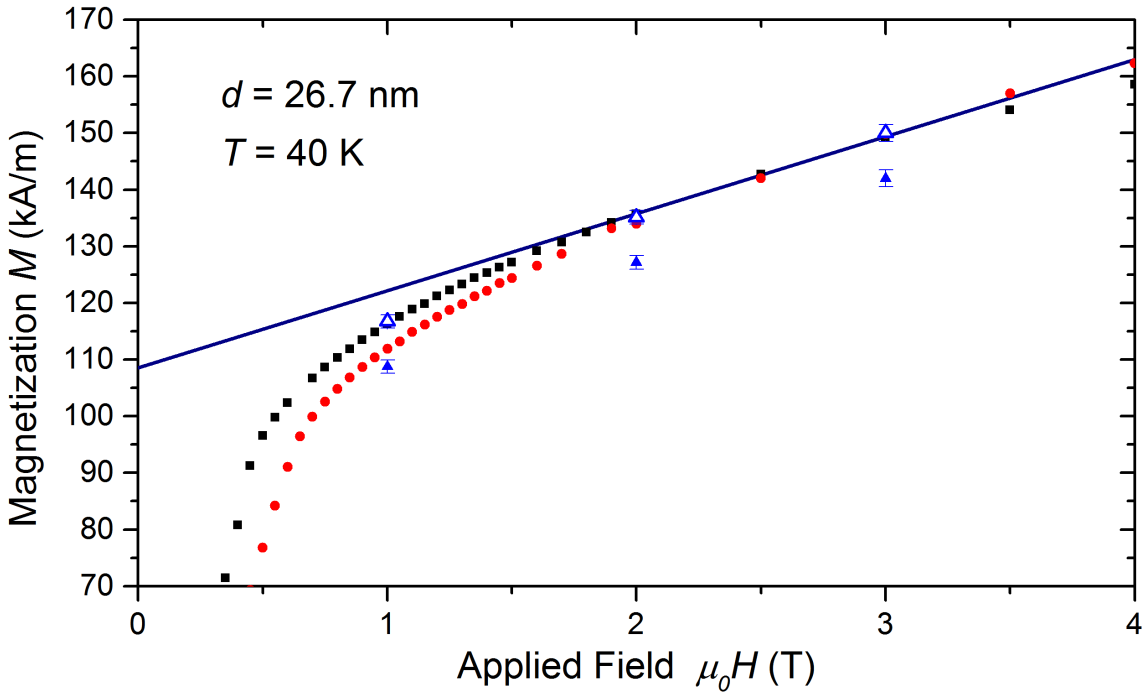

Figure 4.7: Comparison of the magnetization values of the $d = 26.7$ nm film measured by PNR and SQUID magnetometry. The blue closed triangles are the PNR fit magnetization values with $H \parallel [1\bar{1}0]$, the blue open triangles are the same PNR fit magnetization values offset by 8 kA/m, the red circles are the magnetization values measured by SQUID magnetometry with $H \parallel [111]$, and the black squares are the magnetization values measured by SQUID magnetometry with $H \parallel [1\bar{1}0]$. The navy line shows the high-field susceptibility.

$M-H$ curves measured at each temperature that had been corrected using the Arrott plot analysis. These M_S values were then fit with a quadratic function to give the red line shown in Fig. 4.8. The saturation magnetization, $M_S = 97.4$ kA/m, for the PNR measurements is then compared to the quadratic M_S fit line on this figure. This comparison indicates that the offset of the PNR magnetization values can be explained by a "true" temperature for the PNR measurements of 41.3 K as would be measured by the SQUID. A temperature calibration deviation of this magnitude between different cryogenic system is reasonable, and it is likely that this is the cause observed offset. As the curie temperature measured on the SQUID magnetometer has been cross-checked to values obtained from resistivity values on a different instrument, it is more likely that the PNR setup is the source of the calibration error.

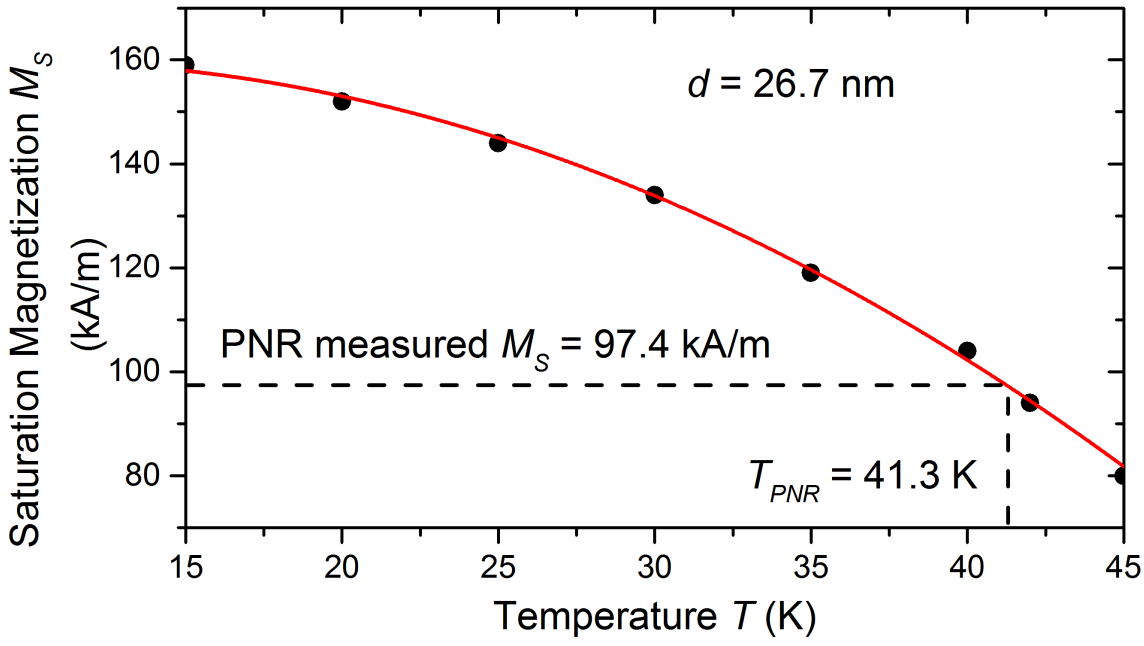

Figure 4.8: Saturation magnetization values for the $d = 26.7$ nm thin film. The black circles show the values from SQUID-measured $M - H$ curves, and the red line shows a quadratic fit to these points. The dotted lines indicate the saturation magnetization from the PNR magnetization fits and the temperature that this corresponds to.

Notwithstanding the temperature discrepancy, the high-field susceptibility measured by PNR is consistent with the measurements of both samples by Arrott plot analysis. The agreement between these two methods provides strong evidence that the high-field susceptibility in these films is a real effect effect that can be accurately accounted for with the novel use of Arrott plots. Hence, I have assumed that the Arrott plot analysis yields an accurate background correction factor. This background correction factor was used to produce the magnetization curves shown in Fig. 4.2.

From Fig. 4.2, I calculated the static susceptibility as a function of field to look for peaks that indicate first-order transitions that may not be obvious in the $M - H$ data. The results of these calculations are shown in Fig. 4.9. This figure shows no first-order transitions, consistent with a continuous transition from a helical phase at zero field, through a conical phase, and to a ferromagnetic phase above the saturation field.

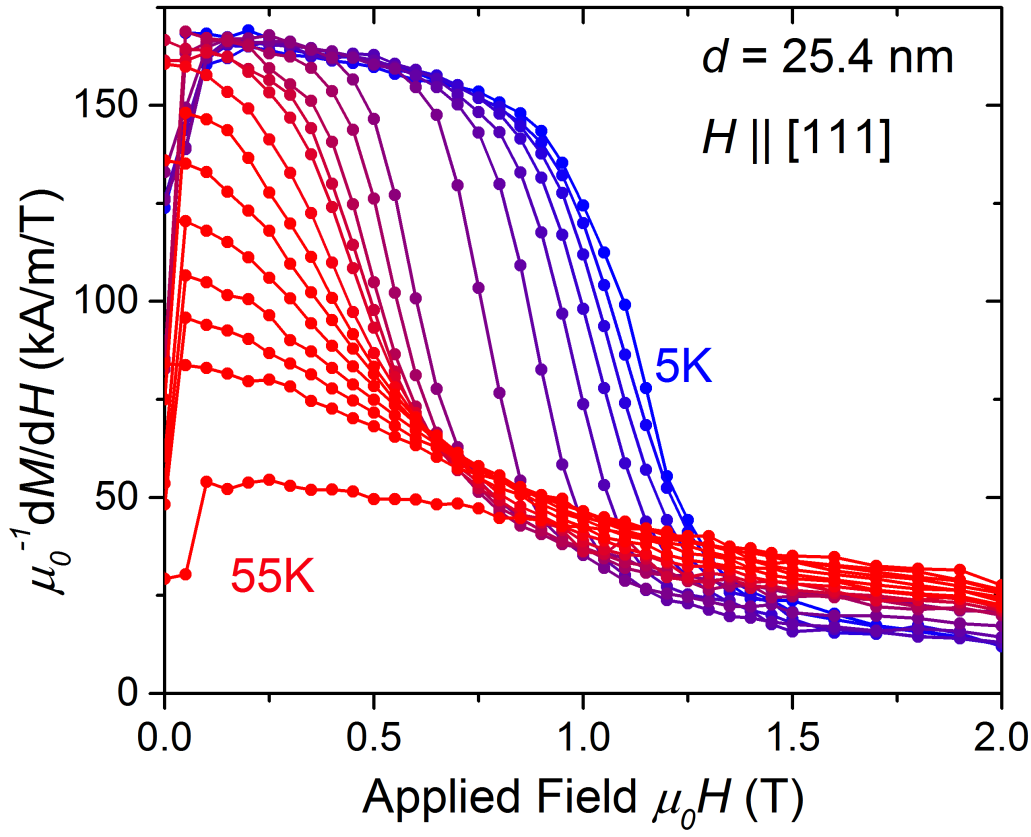

Figure 4.9: Static susceptibility versus field of the $d = 25.4$ nm MnSi film obtained by taking the derivative of Fig. 4.2. Temperatures shown are 5 - 40 K in 5 K steps, 41 - 50 K in 1 K steps, 42.5 K and 55 K. The applied field points out of the plane of the film, along $H \parallel [111]$.

However, there is one feature on these plots that requires discussion. At many of the temperatures there is a markedly decreased susceptibility for the points at very low field, followed by a sharp increase up to a flat plateau. This effect is similar to the susceptibility changes as the helix reorients in bulk MnSi [95]. Further, SQUID samples are manually mounted in a plastic straw and adjusted by eye to the correct orientation. This makes it difficult to align the sample perfectly with $H \parallel [111]$; misalignments of up to a few degrees are expected. Hence, it is likely that this deviation represents the small reorientation of the helical Q vector from the [111] direction to the field direction when the sample was slightly misaligned.

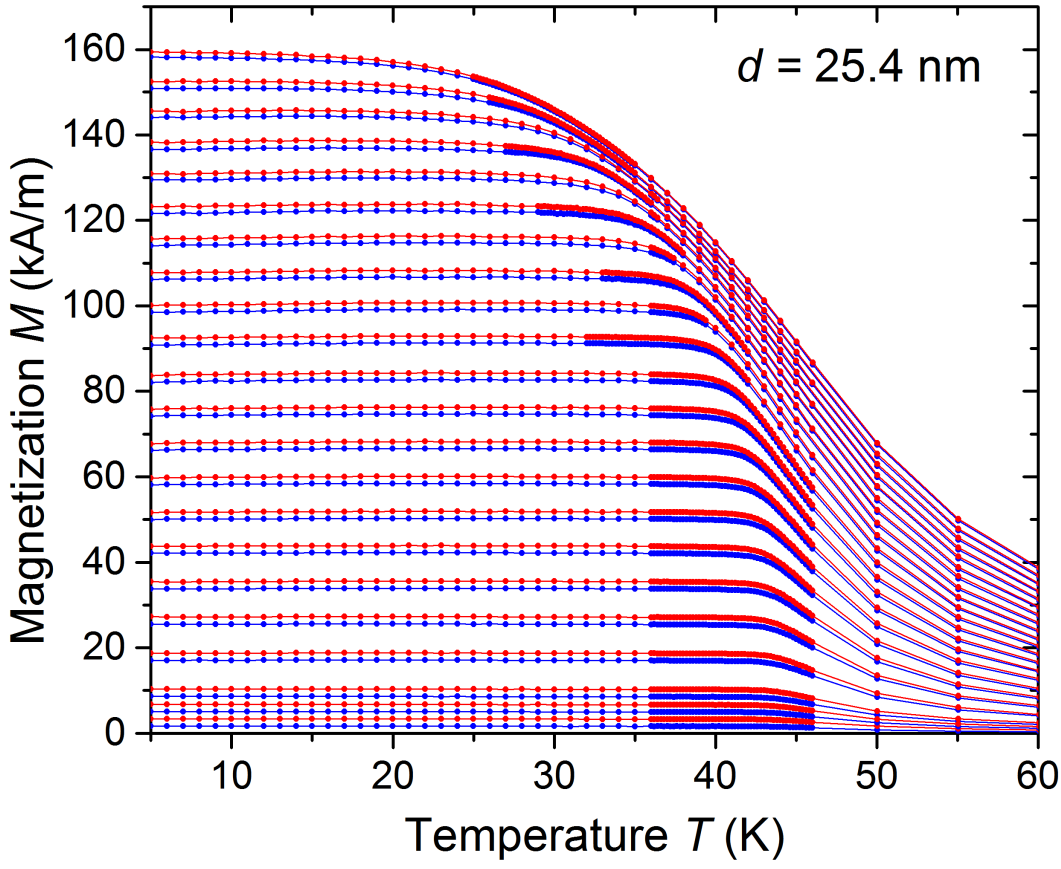

Figure 4.10: Field-cooled magnetization measurements for the $d = 25.4$ nm MnSi film. Data sets shown in blue are for field values in steps of $B = 0.05$ T from 0.1 to 1.0 T and steps of 0.02 T from 0.01 T to 0.05 T, and the data sets in red are each measured at a field 10 mT higher than the blue. Applied field points out of the plane of the film along $H \parallel [111]$

It is also instructive to consider plots of the susceptibility as a function of temperature, as these may give evidence of transitions that are vertical on a $H-T$ phase diagram, and hence would not appear on the M-H plots shown above. In addition, the in-plane skyrmion phase does show a distinct peak in susceptibility-temperature plots at its phase boundaries, as shown in Fig. 3.9. Therefore, as a second means of screening for skyrmions, I performed a similar set of measurements for $H \parallel [111]$. I measured the magnetization as a function of temperature for a wide range of fields by cooling the samples in an applied field from $T = 100$ K to 5K and then measuring the magnetization on warming. These curves are shown in Fig. 4.10.

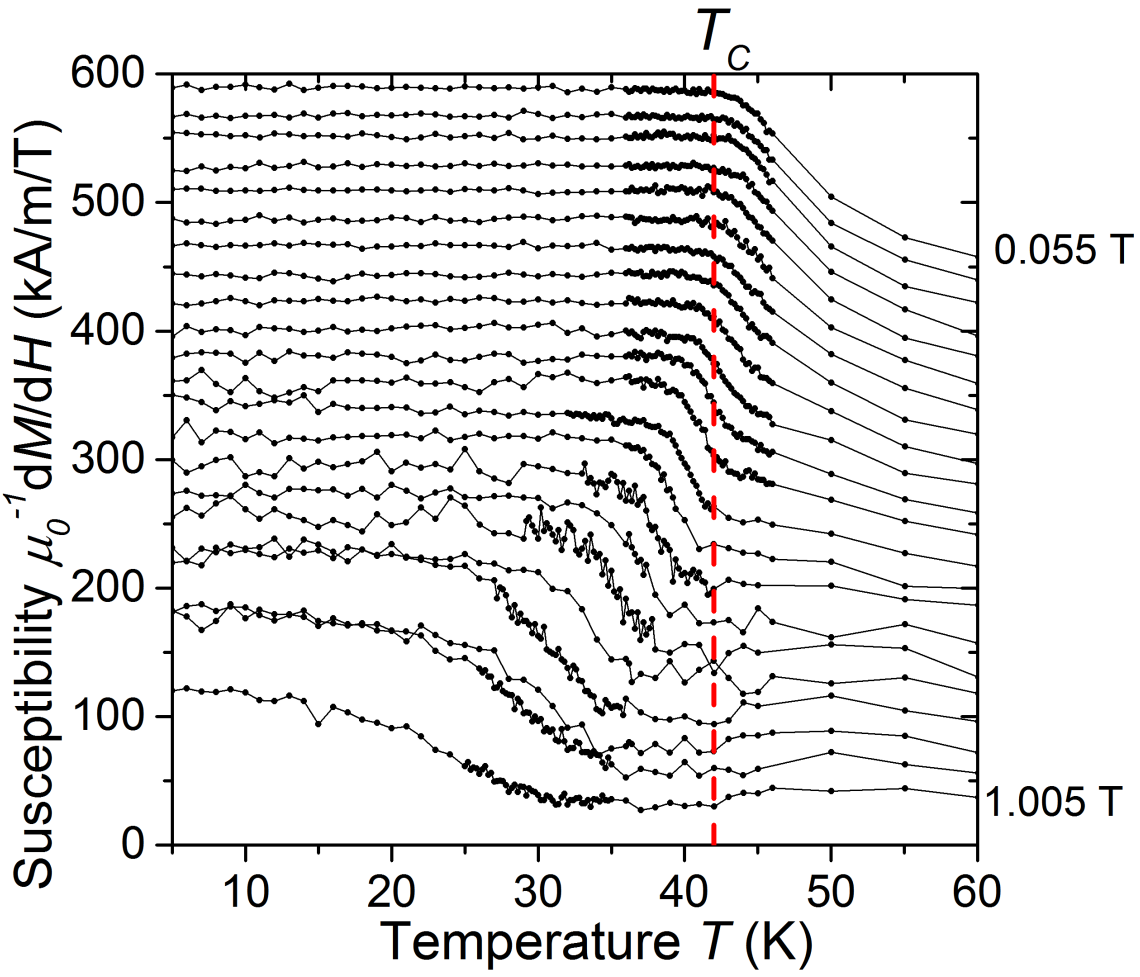

Figure 4.11: Susceptibility curves determined from field cooled magnetization measurements on the $d = 25.4$ nm MnSi film. Each curve was calculated from field cooled scans at fields separated by 10 mT. Field values shown are in steps of 0.02 T from 0.015 T to 0.055 T and in steps of $B = 0.05$ T from 0.105 to 1.005 T from top to bottom. These curves are offset by 20 kA/m/T for clarity. Applied field points out of the plane of the film along $H \parallel [111]$.

From these curves, the static susceptibility is calculated by taking the derivative between curves separated by $B = 10$ mT, as was done in section 3.1. The resulting curves are shown in Fig. 4.11. Figure 4.12 shows an expanded view of the curves from $B = 0.2$ to 0.55 T near T_C, which corresponds the the bulk A-phase region where transitions might be expected to show up. Neither of these figures show evidence of peaks in the susceptibility that would indicate first-order transitions, and hence it can be concluded that there is no skyrmion phase for $H \parallel [111]$.

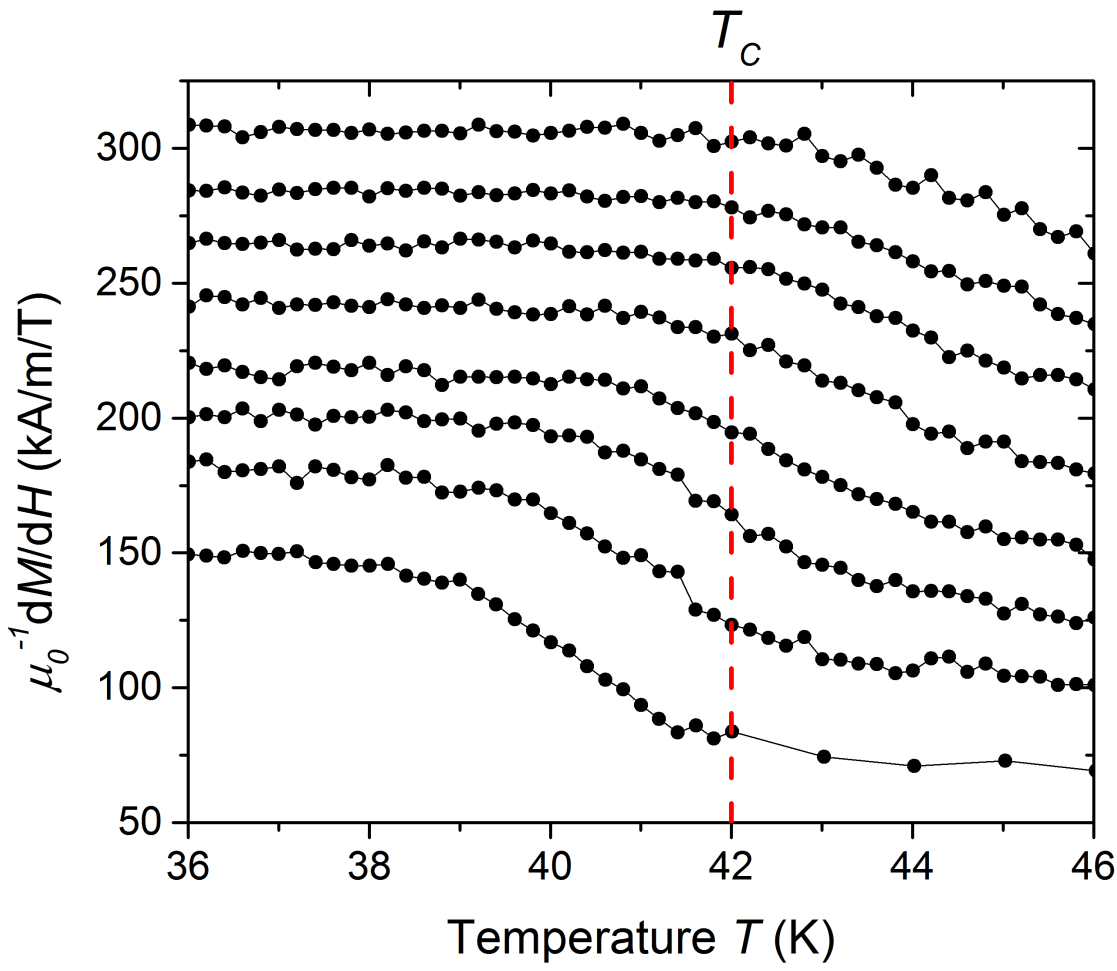

Figure 4.12: Susceptibility curves determined from field cooled magnetization measurements on the $d = 25.4$ nm MnSi film. Each curve was calculated from field cooled scans at fields separated by 10 mT. Field values shown are 0.205, 0.255, 0.305, 0.355, 0.405, 0.455, 0.505 and, 0.555 T from top to bottom, and are offset by 20 kA/m/T for clarity. Applied field points out of the plane of the film along $H \parallel [111]$.

The curves for 0.905 T and 0.705 T in Fig. 4.11 appear to be offset significantly at low temperature relative to what is expected from the other curves. Normally, this would indicate peaks in the susceptibility as a function of field centered on these two curves that persist over a broad temperature range. However, since no such peaks were seen in Fig. 4.2, this deviation is much more likely a result of some extrinsic effect, rather than showing a transition in the films. These two curves were measured at a later time, with the sample mounted in a different straw than for the

measurements of the other curves. Hence, one possible explanation is that there was some contaminant introduced into the straw that produced this deviation.

An additional method that can be used to interrogate the phase diagram of this film is magnetoresistance. Kadowaki et al. have shown that the transition into and out of the skyrmion A-phase in bulk samples is accompanied by peaks in the magnetoresistance [25], and hence peaks of this nature would be expected if this film hosts a skyrmion phase. The magnetoresistance was measured as described in section 2.4 at a variety of temperatures between 10 and 46 K, and the resistivity calculated from equation 2.13, where V_L is the longitudinal voltage, and I is the current.

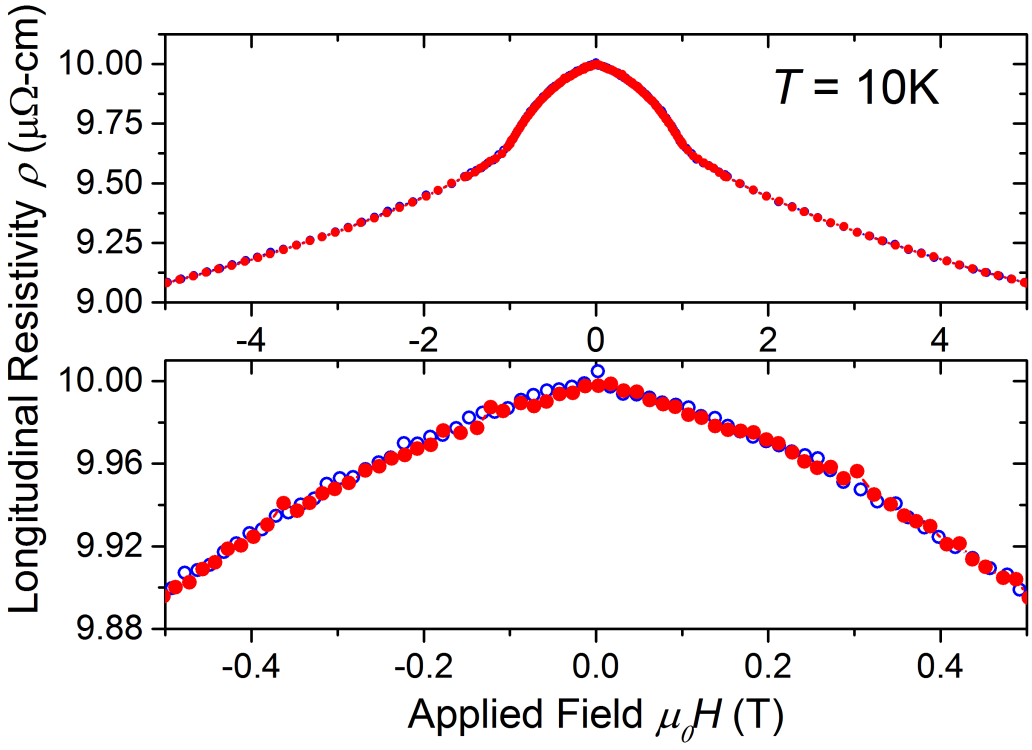

Figure 4.13: Magnetoresistance of the $d = 25.4$ nm MnSi film with applied field pointing out-of-plane along the [111] direction at $T = 10$ K. Open blue circles represent the data points measured on decreasing field, and close red circles represent the data points measured on increasing field.

First, Fig. 4.13 is presented to show that there is no hysteresis in the magnetoresistance data, even at small field. This gives additional weight to the argument

that the slight deviation at low field seen in the SQUID data is a result of sample misalignment, as the mount for magnetoresistance measurements makes it much easier to align the sample very close to the desired $\vec{H} \parallel [111]$. Therefore, the lack of any deviation here is indicative of what would be seen with perfect alignment in the SQUID data. Next, the magnetoresistance ratio $\Delta\rho_{xx}/\rho_{xx0} = (\rho_{xx} - \rho_{xx0})/\rho_{xx0}$, where ρ_{xx} is the longitudinal resistivity and ρ_{xx0} is the zero field longitudinal resistivity, was calculated at each field in order to emphasize changes in the resistivity, with the resultant curves shown in Fig. 4.14. These show no evidence of peaks that would indicate a skyrmion phase, consistent with the interpretation of the magnetometry data.

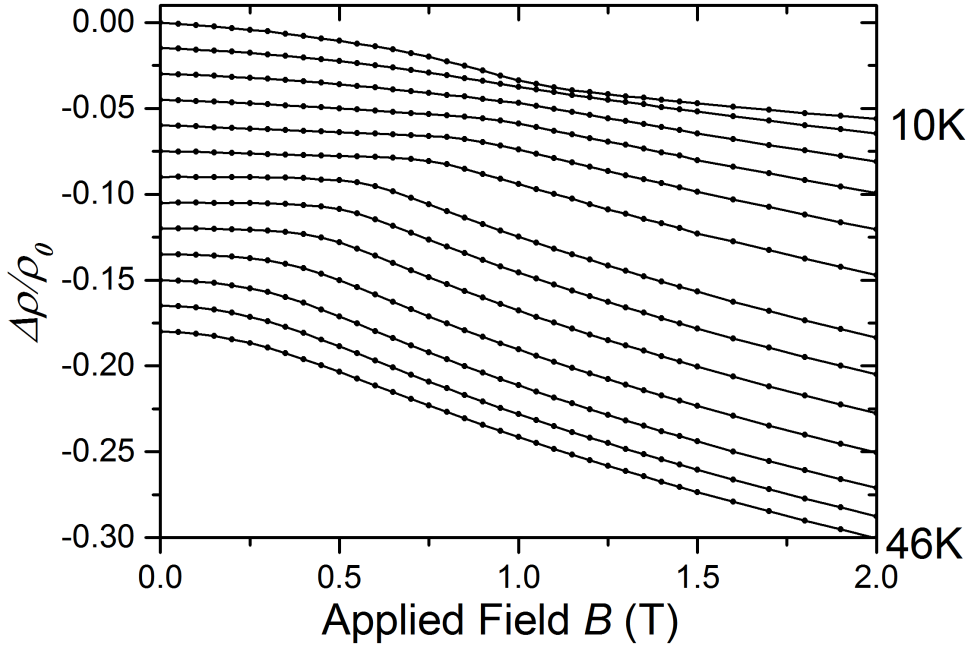

Figure 4.14: Magnetoresistance of the $d = 25.4$ nm MnSi film with applied field pointing out-of-plane along $H \parallel [111]$. Temperatures shown are 10 - 40 K in 5 K steps and 41 - 46 K in 1 K steps. Curves are offset by -0.015 for clarity, for T >10 K. increasing.

The magnetoresistance and magnetometry data together support the simple phase diagram shown in Fig. 4.15, where the system transitions smoothly through a conical state into the ferromagnetic state. Significantly, the detailed investigation over

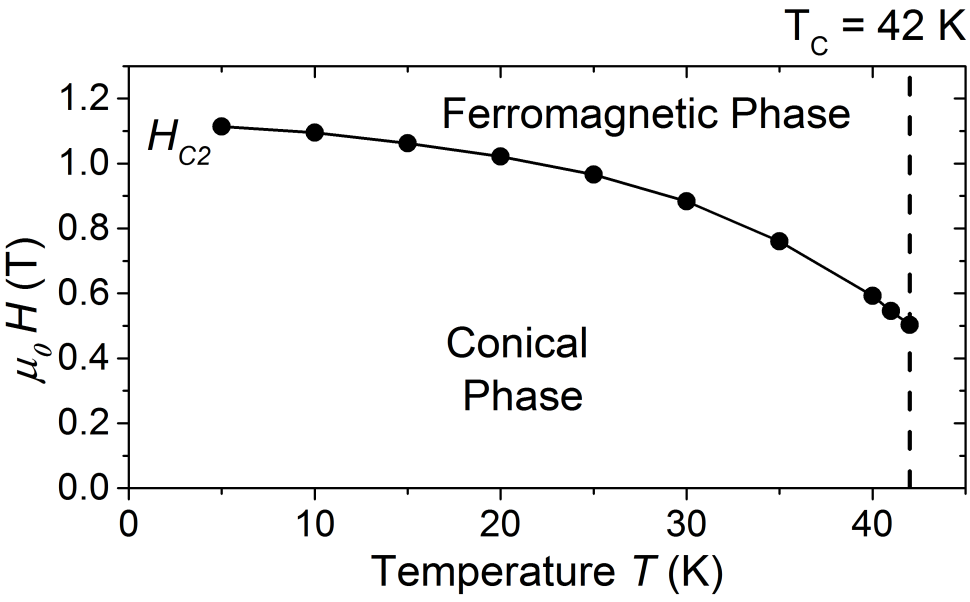

Figure 4.15: Phase diagram for the $d = 25.4$ nm MnSi film with an applied field $\vec{H} \parallel [111]$. Closed black circles are saturation fields determined from a minima in d^2M/dH^2 calculated from M-H curves.

the entire phase diagram shows no evidence of a skyrmion pocket at any field or temperature values, which is a significant contrast to the broad skyrmion stability region with an in-plane field. This highlights the importance of the magnetocrystalline anisotropy in stabilizing the skyrmion phase.

4.2 Hall Effect

A topological contribution to the Hall effect has been taken by others as a sufficient condition to prove the existence of a skyrmion phase. Therefore, I measured the Hall resistivity of the $d = 25.4$ nm patterned sample, as described in section 2.4, for a variety of temperatures below T_C. The data was then fit to Eq. 4.2, including the regular Hall effect, R_0H, and the anomalous Hall effect, $S_HM\rho_{xx}^2$,

$$\rho_{yx} = R_0\mu_0H + S_HM\rho_{xx}^2. \tag{4.2}$$

In this equation, R_0 is the Hall coefficient, S_H is a fitting parameter for the anomalous Hall effect, and ρ_{xx} is the longitudinal resistivity. For the fits, I measured ρ_{xx} at the same time as ρ_{yx}, and used the magnetization measured by SQUID magnetometry shown in Fig. 4.2. The resultant fits, along with the data, are shown in Fig. 4.16, and the parameters used to generate the fits are shown in Fig. 4.17. This figure shows that the values of R_0 and S_H vary significantly as a function of temperature, and S_H even changes sign. This is in sharp contrast to Hall effect measurements in bulk MnSi [56] that show temperature independent values of $R_0 = 7.32 \pm 0.06$ nΩ-cm/T and $S_H = -7.06 \pm 0.48 \times 10^{-4}\mathrm{V}^{-1}$. In addition, the values of R_0 in this film, 11-17 nΩ-cm, are significantly larger, with a mean value twice as large as the value measured for bulk MnSi, which indicates a reduced charge carrier density compared to bulk. Density functional calculations show that the band structure of MnSi changes when the structure is strained [62]; this may explain the change in carrier density.

These fits also show a significant deviation over a large field range, similar to that traditionally attributed to a topological contribution [57, 58, 59, 60]. The conventional view would be that this indicates a skyrmion phase covering almost the entire phase diagram. However, the magnetization and magnetoresistance data excludes this possibility as no first-order transitions are observed.

Topological contributions to the Hall effect, as discussed in chapter 2, come from the Berry phase that electrons pick up traversing a loop containing non-coplanar spins. Hence, any spin structure that contains non-coplanar spins that vary in the Hall effect measurement plane will show a topological Hall effect. One possibility for such a structure is shown in Fig. 4.18. This is a conventional cone phase which is also modulated in the in-plane direction, $\hat{x}$, with a propagation vector along the out-of-plane direction, $\hat{z}$. Assuming the in-plane and out-of-plane propagation vectors have

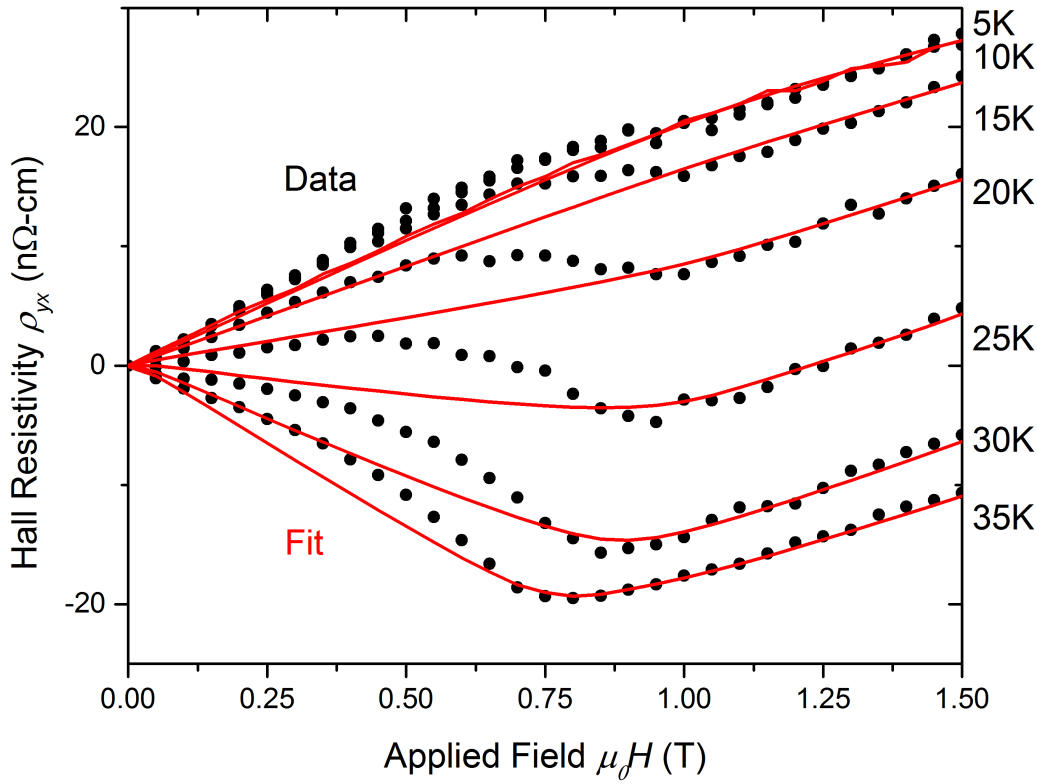

Figure 4.16: Measured Hall resistivity of the $d = 25.4$ nm sample (black circles), and fits to this data using Eq. 4.2 (red lines).

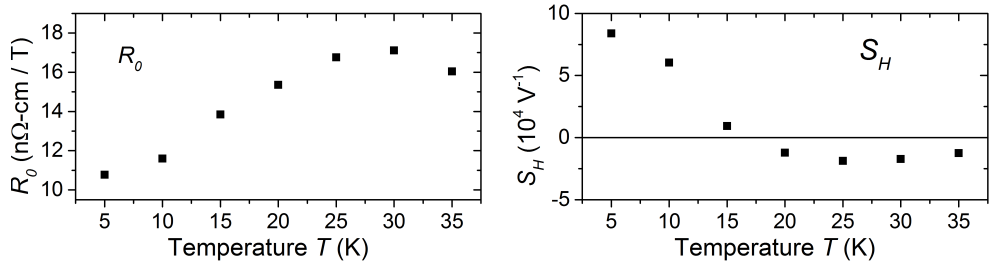

Figure 4.17: Values of the parameters R_0 and S_H used to produce the fits shown in Fig. 4.16.

the same magnitude, Q, the spin texture is described by,

$$\vec{S} = S_0 \left(cos[(x+z)Q]cos(\varphi), sin[(x+z)Q]cos(\varphi), sin(\varphi) \right). \tag{4.3}$$

Considering three neighboring spins in the z=0 plane, $\vec{S}_i(a,0,0)$, $\vec{S}_j(b,0,0)$, and

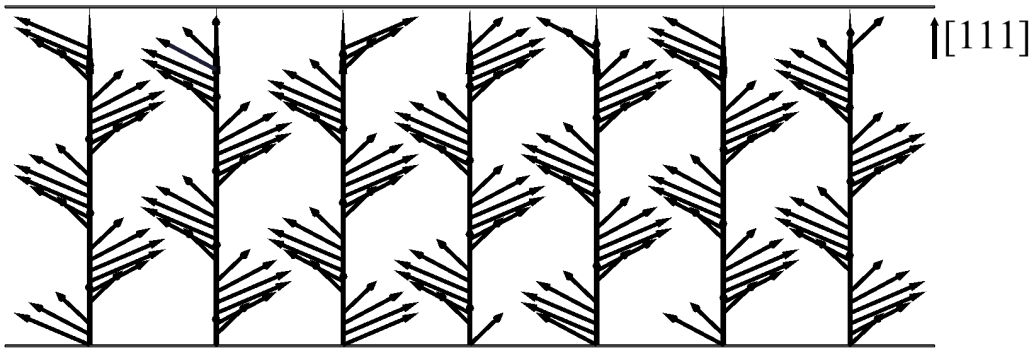

Figure 4.18: Schematic of the modulated cone phase with magnetization given by Eq. 4.3. In this figure the $\vec{Q}$ points out of the page.

$\vec{S_k}(c,0,0)$, the spin chirality, which is proportional to the Hall conductivity, is given by Eq. 4.4.

$$\begin{aligned}\vec{S_i}\cdot\vec{S_j}\times\vec{S_k} =& sin\varphi\ cos^2\varphi\Big[(sin[(a)Q]-sin[(b)q])cos[(c)Q] \\ &-(cos[(a)Q]-sin[(b)Q])sin[(c)Q] \\ &+(cos[(c)Q]sin[(b)Q]-sin[(a)q]cos[(c)Q])\Big]\end{aligned} \tag{4.4}$$

Regardless of the exact spin positions, the spin chirality is proportional to $sin\varphi cos^2\varphi$, where φ is the cone angle. Therefore, $\sigma_{yx}^{top} \propto sin\varphi cos^2\varphi$. The Hall resistivity is equal to the Hall conductivity times ρ_{xx}^2 [58], hence the total Hall resistivity can be written,

$$\rho_{yx} = R_0\mu_0 H + S_H\rho_{xx}^2 M + C\rho_{xx}^2 sin\varphi cos^2\varphi, \tag{4.5}$$

where C is a fitting parameter. The cone angle, φ, can be calculated from the magnetization data as the SQUID with $H \parallel [111]$ measures strictly the out-of-plane component of the magnetization, M_z, and, for a cone phase, $M_z/M_S = sin\varphi$. Using this cone angle, I calculated the topological Hall effect from this proposed spin configuration and adjusted C to best fit the measured topological signature, defined as $\rho_{yx}^{top} = \rho_{yx} - R_0\mu_0 H - S_H\rho_{xx}^2 M$, at each temperature. These fits are shown in Fig.

4.19.

The fits accurately replicate the field dependence of the measured topological hall effect, which shows that the Hall data is consistent with the proposed spin model. This distinctly shows that there are spin arrangements other than the skyrmion phase which produce a significant topological Hall signature and may be present in helimagnetic thin films. It is possible that a simple cone phase may also produce a topological Hall effect, as there is a significant deviation from the fits over a broad field region present in measurements on bulk MnSi [56]. Therefore, the topological signature alone is not sufficient to demonstrate the presence of a skyrmion phase. Further, topological signatures recently advanced by others in FeGe [60] and MnGe [59] as the sole evidence for skyrmions have field dependencies similar to that presented here, and it is thus a distinct possibility that these signatures were misinterpreted in these studies. Reinterpreting signatures of this nature as evidence for an in-plane modulated cone phase rather than skyrmions would require reevaluation of a number of claims of skyrmion stability in various helimagnets, and potentially have a significant impact on the direction of future work towards producing a material in which skyrmions are broadly stable.

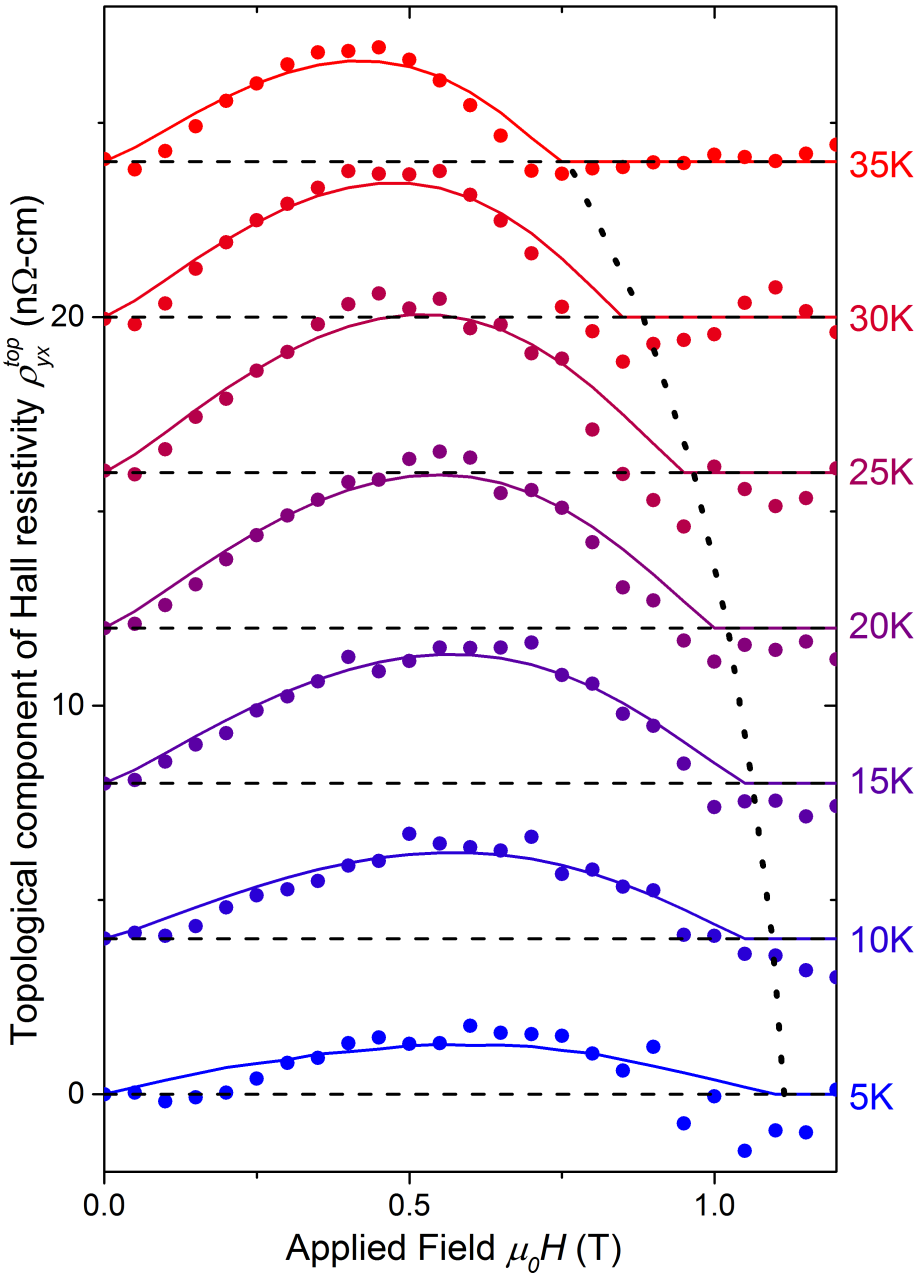

Figure 4.19: Topological component of the Hall resistivity, $\rho_{yx}^{top} = \rho_{yx} - R_0\mu_0 H - S_H\rho_{xx}^2 M$, of the $d = 25.4$ nm sample (circles) along with fits to this data (solid lines) assuming a modulated cone phase as described in the text. The fits are calculated by, $\rho_{yx\_fit}^{top} = C\rho_{xx}^2 sin\varphi cos^2\varphi$, where C is a fitting parameter. Curves are offset by 4 nΩ-cm for clarity, and the dashed lines show the zero for each temperature. The dotted line shows the saturation field at each temperature.

Chapter 5

Conclusion

MnSi thin films grown epitaxially on Si(111) substrates were magnetically characterized by SQUID magnetometry and polarized neutron reflectometry. These measurements indicate that for a magnetic field applied in-plane with $\vec{H} \parallel [1\bar{1}0]$, there exists a broad skyrmion stability region at elevated temperature and fields. The size of this skyrmion region was shown to vary as a function of film anisotropy, which demonstrates a potential method to engineer a structure with a given skyrmion stability region. In addition, skyrmion nucleation was found to occur in two main steps, with up to 40% of the film nucleating into the skyrmion phase at a lower transition field H_β and the rest of the film transitioning into the skyrmion field at a high field, $H_{\alpha 1}$. The skyrmion stability region was found to be qualitatively consistent with theoretical calculations. However, exact quantitative agreement was not found. Future theoretical work should be done to investigate the cause of these discrepancies. In particular, surface and cubic anisotropies that were neglected in the theoretical calculation should be considered. In addition, PNR studies that measure the spin-flip component of the reflectivity should be conducted in order to complete the picture of the magnetic states of the film.

For a field applied out-of-plane with $\vec{H} \parallel [111]$, a detailed investigation of the magnetic states of the films using SQUID magnetometry and transport measurements found no evidence for a skyrmion phase. This is consistent with earlier theoretical predictions that the the uniaxial anisotropy in these films would not stabilize the skyrmion phase in this geometry. In addition, Hall effect measurements were conducted that showed the presence of a topological Hall effect over a broad region of

the film. This shows that the presence of the topological Hall effect is not a sufficient test for the presence of skyrmions. In these films, the topological Hall effect was interpreted as arising from a multidimensionally modulated cone phase with $\vec{Q} \parallel [111]$. Good agreement was found between the expected topological Hall effect from this arrangement and the measured values. This study of the Hall effect raises significant questions about previous claims of skyrmion stability by other groups [57, 60], and could significantly impact the direction of work towards a technologically viable skyrmion-containing magnetic system. Future work should attempt to find additional evidence for this modulated cone phase. In particular, detailed Lorentz microscopy measurements may find evidence for this phase. The contrast for Lorentz microscopy measurements in this phase would be largest when the films are of half-integer wavelength thickness. Therefore, films of thickness $d = 21$ or 35 nm should be studied with this technique.

Magnetometry and PNR results also indicated that MnSi thin films have a high-field susceptibility that is close to 10 times larger than the high field susceptibility observed in bulk MnSi. The high field slopes measured by PNR on a $d = 26.7$ nm sample and by magnetometry on a $d = 25.4$ nm were slightly different. This could indicate that varying the film thickness and strain changes the high field slope. Additional investigations using PNR on films of a variety of thicknesses and strains should be done to determine this dependence, and hopefully help illuminate the cause of the increased high-field susceptibility.

The results of this thesis represent a significant step forward towards a technologically relevant material in which skyrmions are broadly stable. A material of this type could be used in novel magnetic storage devices and significantly impact our future computing capabilities.

Bibliography

[1] M. Julliere. "Tunneling between ferromagnetic films". *Physics Letters A*, **54**, 225 (1975)

[2] G. Binasch, P. Grunberg, F. Aurenbach, and W. Zinn. "Enhanced magnetoresistance in layered magnetic structures with antiferromagnetic interlayer exchange". *Physical Review B*, **39**, 4828 (1989)

[3] M.N. Baibich, J.M. Broto, A. Fert, F. Nguyen Van Dau, and F. Petroff. "Giant magnetoresistance of (001)Fe/(001)Cr magnetic superlattices". *Physical Review Letters*, **61**, 2472 (1988)

[4] S. Yuasa, T. Nagahama, A. Fukushima, Y. Suzuki, and K. Ando. "Giant room-temperature magnetoresistance in single-crystal Fe/MgO/Fe magnetic tunnel junctions". *Nature Materials*, **3**, 868 (2004)

[5] S. Ikeda, J. Hayakawa, Y. Ashizawa, Y.M. Lee, K. Miura, H. Hasegawa, M. Tsunoda, F. Matsukura, and H. Ohno. "Tunnel magnetoresistance of 604% at 300K by suppression of Ta diffusion in CoFeB/MgO/CoFeB pseudo-spin-valves annealed at high temperature". *Applied Physics Letters*, **93**, 082508 (2008)

[6] D.C. Ralph and M.D. Stiles. "Spin transfer torques". *Journal of Magnetism and Magnetic Materials*, **320**, 1190 (2008)

[7] L. Berger. "Low-field magnetoresistance and domain drag in ferromagnets". *Journal of Applied Physics*, **49**, 2156 (1978)

[8] P. P. Freitas and L. Berger. "Observation of s-d exchange force between domain walls and electric current in very thin Permalloy films". *Journal of Applied Physics*, **57**, 1266 (1985)

[9] M. Hayashi, L. Thomas, C. Rettner, R. Moriya, Y.B. Bazaliy and S.S.P. Parkin. "Current driven domain wall velocities exceeding the spin angular momentum transfer rate in permalloy nanowires". *Physical Review Letters*, **98**, 037204 (2007)

[10] J.C. Slonczewski. "Current-driven excitation of magnetic multilayers". *Journal of Magnetism and Magnetic Materials*, **159**, L1 (1996)

[11] L. Berger. "Emission of spin waves by a magnetic multilayer travsersed by a current". *Physical Review B*, **54**, 9353 (1996)

[12] S.S.P. Parkin, M. Hayashi and L. Thomas. "Magnetic domain-wall racetrack memory". *Science*, **320**, 190 (2008)

[13] F. Jonietz, S. Mühlbauer, C. Pfleiderer, A. Neubauer, W. Münzer, A. Bauer, T. Adams, R. Georgii, P. Böni, R.A. Duine, K. Everschor, M. Garst, and A. Rosch. "Spin transfer torques in MnSi at ultralow current densities". *Science*, **330**, 1648 (2010)

[14] X.Z. Yu, N. Kanazawa, W.Z. Zhang, T. Nagai, T. Hara, K. Kimoto, Y. Matsui, Y. Onose and Y. Tokura. "Skyrmion flow near room temperature in an ultralow current density". *Nature Communications*, **3**, 988 (2012)

[15] T. Jeong and W. Pickett. "Implications of the B20 crystal structure for the magnetoelectronic structure of MnSi". *Physical Review B*, **70**, 075114 (2004)

[16] T. Moriya. "Anisotropic superexchange interaction and weak ferromagnetism". *Physical Review*, **120**, 91 (1960)

[17] I. Dzyaloshinsky. "A thermodynamic theory of "weak" ferromagnetism of antiferromagnetics". *Journal of Physics and Chemistry of Solids*, **4**, 241 (1958).

[18] P. Bak and M.H. Jensen. "Theory of helical magnetic structures and phase transitions in MnSi and FeGe". *Journal of Physics C: Solid State Physics*, **13**, L881 (1980)

[19] M.L. Plumer and M.B. Walker. "Wavevector and spin reorientation in MnSi". *Journal of Physics C: Solid State Physics*, **14**, 4689 (1981)

[20] E.A. Karhu, U.K. Rößler, A.N. Bogdanov, S. Kahwaji, B.J. Kirby, H. Fritzsche, M.D. Robertson, C.F. Majkrzak, and T.L. Monchesky. "Chiral modulations and reorientation effects in MnSi thin films". *Physical Review B*, **85**, 094429 (2012)

[21] Y. Ishikawa, K. Tajima, D. Bloch, and M. Roth. "Helical spin structure in manganese silicide MnSi". *Solid State Communications* **19**, 525 (1976)

[22] K. Motoya, H. Yasuoka, Y. Nakamura, and J.H. Wernick. "Helical spin structure in MnSi-NMR studies". *Solid State Communications* **19**, 529 (1976)

[23] K. Motoya, H. Yasuoka, Y. Nakamura, V. Jaccarino, and J.H. Wernick. "^{55}Mn and ^{29}Si NMR in the Helically Ordered State of MnSi". *Journal of the Physical Society of Japan*, **44**, 833 (1978)

[24] S. Kusaka, K. Yamamoto, T. Komatsubara, and Y. Ishikawa. "Ultrasonic study of magnetic phase diagram of MnSi". *Solid State Communications*, **20**, 925 (1976)

[25] K. Kadowaki, K. Okuda, and M. Date. "Magnetization and magnetoresistance of MnSi". *Journal of the Physical Society of Japan*, **51**, 2433 (1982)

[26] Y. Ishikawa and M. Arai. "Magnetic phase diagram of MnSi near critical temperature studied by neutron small angle scattering". *Journal of the Physical Society of Japan*, **53**, 2726 (1984)

[27] B. Lebech, P. Harris, J.S. Pedersen, K. Mortensen, C.I. Gregory, N.R. Bemhoeft, M. Jermy, and S.A. Brown. "Magnetic phase diagram of MnSi". *Journal of Magnetism and Magnetic Materials*, **144**, 119 (1995)

[28] P. Harris, B. Lebech, H.S. Shim, K. Mortensen and J.S. Pedersen. "Small-angle neutron-scattering studies of the magnetic phase diagram of MnSi". *Physica B: Condensed Matter*, **213**, 375 (1995)

[29] D. Lamago, R. Georgii, C. Pfleiderer, and P. Böni. "Magnetic-field induced instability surrounding the A-phase of MnSi: bulk and SANS measurements". *Physica B: Condensed Matter*, **385**, 385 (2006)

[30] S. Mühlbauer, B. Binz, F. Jonietz, C. Pfleiderer, A. Rosch, A. Neubauer, R. Georgii, and P. Böni. "Skyrmion lattice in a chiral magnet". *Science*, **323**, 915 (2009)

[31] C. Pappas, E. Llièvre-Berna, P. Falus, P.M. Bantley, E. Moskvin, S. Grigoriev, P. Foquet, and B. Farago. "Chiral paramagnetic skyrmion-like phase in MnSi". *Physical Reviw Letters*, **102**, 197202 (2009)

[32] T.H.R. Skyrme. "A non-linear field theory". *Proceedings of the Royal Society of London A*, **260**, 127 (1961)

[33] U.A. Khawaja and H.T.C. Stoof. "Skyrmion physics in Bose-Einstein ferromagnets". arXiv:cond-mat, 0107302v1 (2001)

[34] B.P. Anderson, P.C. Haljan, C.A. Regal, D.L. Feder, L.A. Collins, C.W. Clark, and E.A. Cornell. "Watching dark solitons decay into vortex rings in a Bose-Einstein condensate". *Physical Review Letters*, **86**, 2926 (2001)

[35] A.A. Belavin and A.M. Polyakov. "Metastable states of two-dimensional isotropic ferromagnets". *JETP*, **22**, 503 (1975)

[36] S.L. Sondhi, A. Karlhede, E.H. Rezayi and S.A. Kivelson. "Skyrmions and the crossover from integer to fractional quantum Hall effect at small Zeeman energies". *Physical Review B*, **47**, 16419 (1993)

[37] A.N. Bogdanov, U.K. Rößler, and A.A. Shestakov. "Skyrmions in nematic liquid crystals". *Physical Review E*, **67**, 016602 (2003)

[38] Q. Ouyang and H.L. Swinney. "Transition from a uniform state to hexagonal and striped Turing patterns". *Nature*, **352**, 610 (1991)

[39] D.C. Wright and N.D. Mermin. "Crystalline liquids: the blue phases". *Reviews of Modern Physics*, **61**, 385 (1989)

[40] A.N. Bogdanov and D.A. Yablonskii. "Thermodynamically stable "vortices" in magnetically ordered crystals. The mixed state of magnets". *JETP*, **95**, 245 (1989)

[41] A.N. Bogdanov and A. Hubert. "Thermodynamically stable magnetic vortex states in magnetic crystals". *Journal of Magnetism and Magnetic Materials*, **138**, 255 (1994)

[42] U.K. Rößler, A.N. Bogdanov, and C. Pfleiderer. "Spontaneous skyrmion ground states in magnetic metals". *Nature* **442**, 797 (2006)

[43] A.N. Bogdanov, U.K. Rößler, and C. Pfleiderer. "Modulated and localized structures in cubic helimagnets". *Physica B: Condensed Matter*, **359**, 1162 (2005)

[44] S. Heinze, K. von Bergmann, M. Menzel, J. Brede, A. Kubetzka, R. Wiesendanger, G. Bihlmayer, and S. Blügel. "Spontaneous atomic-scale magnetic skyrmion lattice in two dimensions". *Nature Physics*, **7**, 713 (2011)

[45] N.S. Kiselev, A.N. Bogdanov, R. Schäfer, and U.K. Rößler. "Chiral skyrmions in thin magnetic films: new objects for magnetic storage technologies?". *Journal of Physics D: Applied Physics*, **44**, 392001 (2011)

[46] A. Fert, V. Cros and J. Sampaio. "Skyrmions on the track". *Nature Nanotechnology (Commentary)*, **8**, 152 (2013)

[47] U.K. Rößler, A.A. Leonov, A.N. Bogdanov. "Chiral Skyrmionic matter in non-centrosymmetric magnets". *Journal of Physics: Conference Series*, **303**, 012105 (2011)

[48] H. Wilhelm, M. Baenitz, M. Schmidt, C. Naylor, R. Lortz, U.K. Rößler, A.A. Lenov and A.N. Bogdanov. "Confinement of chiral magnetic modulations in the precursor region of FeGe". *Journal of Physics: Condensed Matter*, **24**, 294204 (2012)

[49] S.V. Grigoriev, S.V. Maleyev, E.V. Moskvin, V.A. Dyadkin, P. Foquet and H. Echerlebe. "Crossover behaviour of critical helix fluctuations in MnSi". *Physical Review B*, **81**, 144413 (2010)

[50] X.Z. Yu, Y. Onose, N. Kanazawa, J.H. Park, J.H. Han, Y. Matsui, N. Nagaosa, and Y. Tokura. "Real-space observation of a two-dimensional skyrmion crystal". *Nature*, **465**, 901 (2010)

[51] M.E. Hale, H.W. Fuller and H. Rubinstein. "Magnetic domain observation by electron microscopy". *Journal of Applied Physics*, **30**, 789 (1959)

[52] X.Z. Yu, N. Kanazawa, Y. Onose, K. Kimoto, W.Z. Zhang, S. Ishiwata, Y. Matsui, and Y. Tokura. "Near room-temperature formation of a skyrmion crystal in thin-films of the helimagnet FeGe". *Nature Materials* **10**, 106 (2011)

[53] A. Tonomura, X. Yu, K. Yanagisawa, T. Matsuda, Y. Onose, N. Kanazawa, H.S. Park, and Y. Tokura. "Real-space observation of skyrmion lattice in helimagnet MnSi thin samples". *Nano letters*, **12**, 1673 (2012)

[54] C. Pfleiderer, T. Adams, A. Bauer, W. Biberacher, B. Binz, F. Birkelbach, P. Böni, C. Franz, R. Georgii, M. Janoschek, F. Jonietz, T. Keller, R. Ritz, S. Mühlbauer, W. Münzer, A. Neubauer, B. Pedersen, and A. Rosch. "Skyrmion lattices in metallic and semiconducting B20 transition metal compounds". *Journal of physics: Condensed Matter*, **22**, 164207 (2010)

[55] A.N. Bogdanov and U.K. Rößler. "Chiral symmetry breaking in magnetic thin films and multilayers". *Physical Review Letters*, **87**, 037203 (2001)

[56] M. Lee, Y. Onose, Y. Tokura, and N.P. Ong. "Hidden constant in the anomalous Hall effect of high-purity magnet MnSi". *Physical Review B*, **75**, 172403 (2007)

[57] A. Neubauer, C. Pfleiderer, B. Binz, A. Rosch, R. Ritz, P.G. Niklowitz, and P. Böni. "Topological Hall effect in the A phase of MnSi". *Physical Review Letters*, **102**, 186602 (2009)

[58] M. Lee, W. Kang, Y. Onose, Y. Tokura, and N.P. Ong. "Unusual Hall effect anomaly in MnSi under pressure". *Physical Review Letters*, **102**, 186601 (2009)

[59] N. Kanazawa, Y. Onose, T. Arima, D. Okuyama, K. Ohoyama, S. Wakimoto, K. Kakurai, S. Ishiwata, and Y. Tokura. "Large topological Hall effect in a short-period helimagnet MnGe". *Physical Review Letters*, **106**, 156603 (2011)

[60] S.X. Huang and C.L. Chien. "Extended skyrmion phase in epitaxial FeGe(111) thin films". *Physical Review Letters*, **108**, 267201 (2012)

[61] A.B. Butenko, A.A. Leonov, U.K. Rößler, and A.N. Bogdanov. "Stabilization of skyrmion textures by uniaxial distortions in noncentrosymmetric cubic helimagnets". *Physical Review B*, **82**, 052403 (2010)

[62] E.A. Karhu. "Structural and magnetic properties of epitaxial MnSi(111) thin films". *PhD Thesis Dalhousie University*, (2012)

[63] S. Higashi, P. Kocán, and H. Tochihara. "Reactive epitaxial growth of MnSi ultrathin films on Si(111) by Mn deposition". *Physical Review B*, **79**, 205312 (2009)

[64] M.M.R. Evans, J.C. Glueckstein, and J. Nogami. "Epitaxial growth of manganese on silicon: Volmer-Weber growth on the Si(111) surface". *Physical Review B*, **53**, 4000 (1996)

[65] S.M. Shivaprasad, C. Anandan, S.G. Azatyan, Y.L. Gavriljuk, and V.G. Lifshits. "The formation of Mn / Si (111) interface at room and high temperatures". *Surface Science* **382**, 258 (1997)

[66] T. Nagao, S. Ohuchi, Y. Matsuoka, and S. Hasegawa. "Morphology of ultrathin manganese silicide on Si(111)". *Surface Science*, **419**, 134 (1999)

[67] Q. Zhang, M. Tanaka, M. Takeguchi, and K. Furuya. "Analytical UHV transmission electron microscopy studies of electronic structure changes between as-deposited Mn and Mn silicide on Si(111) surface". *Surface Science*, **507**, 453 (2002)

[68] A. Kumar, M. Tallarida, M. Hansmann, U. Starke, and K. Horn. "Thin manganese films on Si(111)-(7 × 7): electronic structure and strain in silicide formation". *Journal of Physics D: Applied Physics*, **37**, 1083 (2004)

[69] E. Magnano, F. Bondino, C. Cepek, F. Parmigiani, and M. C. Mozzati. "Ferromagnetic and ordered MnSi(111) epitaxial layers". *Applied Physics Letters*, **96**, 152503 (2010)

[70] E.A. Karhu, S. Kahwaji, C. Parsons, M.D. Robertson, C. Maunders and T.L. Monchesky. "Structure and magnetic properties of MnSi epitaxial thin films". *Physical Review B*, **82**, 184417 (2010)

[71] J.E. Jorgensen and S.E. Rasmussen. "Refinement of the structure of MnSi by powder diffracton". *Powder Diffraction*, **6**, 194 (1991)

[72] K. Schwinge, C. Muller, A. Mogilatenko, J.J. Paggel, and P. Fumagalli. "Structure and magneto-optic Kerr measurements of epitaxial MnSi films on Si(111)". *Journal of Applied Physics*, **97**, 103913 (2005)

[73] E.A. Karhu, S. Kahwaji, M.D. Robertson, H. Fritzsche, B.J. Kirby, C.F. Majkrzak, and T.L. Monchesky. "Helical magnetic order in MnSi thin films". *Physical Review B (Rapid Communications)*, **84**, 060404(R) (2011)

[74] K. Binder. "Theory of first-order phase transitions". *Reports on Progress in Physics*, **50**, 783 (1987)

[75] A. Bauer and C. Pfleiderer. "Magnetic phase diagram of MnSi inferred from magnetization and ac susceptibility". *Physical Review B*, **85**, 214418 (2012)

[76] L.G. Parrat. "Surface studies of solids by total reflection of X-rays". *Physical Review*, **95**, 359 (1954)

[77] SimulReflec. http://www-llb.cea.fr/prism/programs/simulreflec/simulreflec.html

[78] F. Mezei. "Neutron spin echo: a new concept in polarized thermal neutron techniques". *Z. Physik*, **255**, 146 (1972)

[79] H. Fritzsche. "Polarized neutron reflectometry in high magnetic fields". *Review of Scientific Instruments*, **76**, 115104 (2005)

[80] R. Doll and M. Näbauer. "Experimental proof of magnetic flux quantization in a superconducting ring". *Physical Review Letters*, **7**, 51 (1961)

[81] B.S. Deaver and W.M. Fairbank. "Experimental evidence for quantized flux in superconducting cylinders". *Physical Review Letters*, **7**, 43 (1961)

[82] B.D. Josephson. "Possible new effects in superconductive tunnelling". *Physics Letters*, **1**, 251 (1962)

[83] P.W. Anderson and J.M. Rowell. "Probable observation of the Josephson junction superconducting tunelling effect". *Physical Review Letters*, **10**, 230 (1963)

[84] N. Nagaosa, J. Sinova, S. Onoda, A.H. MacDonald and N.P. Ong. "Anomalous Hall effect". *Reviews of Modern Physics*, **82**, 1539 (2010)

[85] R. Karplus and J.M. Luttinger. "Hall effect in ferromagnetics". *Physical Review*, **95**, 1154 (1954)

[86] M.V. Berry. "Quantal phase factors accompanying adiabatic changes". *Proceedings of the Royal Society of London A*, **392**, 45 (1984)

[87] B. Binz and A. Vishwanath. "Chirality induced anomalous-Hall effect in helical spin crystals". *Physica B: Condensed Matter*, **403**, 1336 (2008)

[88] F.N. Rybakov. Private Communication (2013)

[89] M.L. Plumer and M.B. Walker. "Magnetoelastic effects in the spin-density wave phase of MnSi". *Journal of Physics C: Solid State Physics*, **15**, 7181 (1982)

[90] B. Lebech, J. Berhard and T. Freltoft. "Magnetic structures of cubic FeGe studied by small angle neutron scattering". *Journal of Physics: Condensed Matter*, **1**, 6105 (1989)

[91] A.I. Okorokov, S.V. Grigoriev, Y.O. Chetverikov, S.V. Maleyev, R. Georgii, P. Böni, D. Lamago, H. Eckerlebe and K. Pranzas. "The effect of the magnetic field on the spiral spin structure in MnSi studied by polarized SANS". *Physica B*, **356**, 259 (2005)

[92] A. Arrot. "Criterion for ferromagnetism from observations of magnetic isotherms". *Physical Review*, **108**, 1394 (1957)

[93] M.K. Chattopadhyay, P. Arora and S.B. Roy. "Magnetic properties of the field-induced ferromagnetic state in MnSi". *Journal of Physics: Condensed Matter*, **21**, 296003 (2009)

[94] D. Bloch, J. Voiron, V. Jaccarino and J.H. Wernick. "The high field-high pressure magnetic properties of MnSi". *Physics Letters A*, **51**, 259 (1975)

[95] C. Thessieu, C. Pfleiderer and J. Floquet. "Thermodynamical study under hydrostatic pressure of MnSi". *Physica B*, **239**, 67 (1997)